POLITECNICO DI MILANO

School of Engineering
Civil and Environmental Engineering

Master of Science in
Environmental Engineering

Hydro–Glaciological Modelling for the Dudh Kosi River basin, Nepal

Supervisor:
Prof. Daniele Bocchiola

Co–Supervisor:
Ing. Gabriele Confortola

Author:
Michela Buizza
Matr. 798666

Academic Year 2013/2014

"Felix qui potuit rerum cognoscere causas."

Virgil, Georgics. Book 2, verse 490.

Abstract

Understanding the hydrological dynamics of high altitude glacierised regions in the Himalayas is becoming more and more important as flash floods and the related hazards along with the glacier−stored water resources depletion are increasingly affecting the livings and economies of millions of people. This thesis develops a tool for modelling the hydro−glaciological processes in the Dudh Kosi River basin, Eastern Nepal, with particular focus on the Khumbu glacier, located within the catchment on the flanks of Mount Everest. A semi−distributed hydrological model is implemented over the study area (3700 km^2) at a daily time step, fed by ground observations merged with satellite long term averages of meteorological variables; evapotranspiration, surface runoff, snow and ice ablation, groundwater flow are simulated. The model is able to predict discharge time series along the river, yielding good NSE at the basin outlet; model performance is improved with respect to the previously adopted altitude belts hydrological model. Flood peaks magnitude during summer monsoon still constitutes the major challenge, suggesting that further studies are necessary to appropriately depict precipitation patterns and soil water contents. Thereafter, a finer scale hydro−glaciological model is set up for the subcatchment closed 4 km downstream the tongue of Khumbu glacier. The model specifically addresses the major glaciological processes, such as snow and clean ice melt, reproduced by means of a hybrid model, ice melt under debris cover, simulated with an energy budget approach, glacier dynamics and water storage within ice and snow. The predictions of discharge at Periche show good agreement with the observations, as well as ice velocities and ice ablation rates. The analysis shows that the Dudh Kosi River flow is dominated by ice melt at high altitudes (70% of annual discharge) with rainfall contributions increasing downstream (from 15% at Periche to 64% at Rabuwa Bazar). While decreasing, ice melt plays an important role in the downstream region, providing 30% of the annual discharge. The two scale modelling approach is able to simulate discharge along the Dudh Kosi River and to spatially describe ice ablation and glacier flow, thereby offering a tool for studying the fate of Khumbu glacier under different climatic scenarios and for assessing natural hazards and water availability in the remote Himalayan catchment.

Abstract

La comprensione delle dinamiche idrologiche nei bacini Himalaiani d'alta quota diventa sempre più importante con il verificarsi più frequente di piene devastanti e lo scioglimento dei ghiacciai, dato l'elevato numero di persone colpite da questi eventi. Questa tesi vuole dunque sviluppare un modello idro−glaciologico per il fiume Dudh Kosi, nel Nepal Orientale, analizzando in particolare il ghiacciaio del Khumbu, situato alle pendici del Monte Everest. Viene utilizzato un modello idrologico semi−distribuito a celle con passo giornaliero, che utilizza in ingresso variabili meteorologiche rilevate da stazioni a terra integrate con dati satellitari mediati sul lungo periodo. Sono simulatati processi quali l'evapotraspirazione, il deflusso superficiale e sotterraneo, lo scioglimento di neve e ghiaccio. Il modello restituisce in uscita l'idrogramma simulato in diverse sezioni del fiume; alla sezione di chiusura si ottiene una buona efficienza e un miglioramento rispetto alle simulazioni del precedente modello a fasce altitudinali. Ciò nonostante, la previsione del valore dei picchi di piena monsonici rimane scarsamente accurata, indicando che la via per possibili miglioramenti consiste nell'approfondire la rappresentazione spaziale delle piogge. In secondo luogo, un modello idro−glaciologico a maggior risoluzione spaziale viene implementato per il ghiacciaio del Khumbu, simulando dettagliatamente lo scioglimento di neve, ghiaccio scoperto, ghiaccio coperto da detrito, nonché la dinamica e l'idrologia glaciali. Le portate alla sezione di chiusura, posta 4 km a valle del ghiacciaio, riproducono bene i dati osservati; lo stesso vale per le velocità del ghiaccio ed i tassi di fusione. Dal modello si ricava che nelle zone più a monte la portata del fiume Dudh Kosi è composta prevalentemente (70%) da fusione glaciale, mentre il contributo derivante dalle precipitazioni cresce dal 16% a monte al 64% alla chiusura di valle; l'ablazione glaciale risulta comunque rilevante a valle, dove contribuisce per il 30% al deflusso annuale. Tale approccio modellistico a doppia scala consente di simulare la portata del fiume Dudh Kosi in diverse sezioni, così come i processi di dinamica e ablazione glaciale spazialmente distribuiti; il modello, dunque, si candida come strumento per lo studio del rischio naturale e dell'evoluzione glaciale per diversi scenari climatici in un bacino Himalayano scarsamente strumentato.

Acknowledgements

This study is made possible by the people and organization that collected and elaborated the data I largely relied upon. Meteorological data are provided by the Italian EvK2−CNR Committee, Dibas Shrestha from the Nepal Academy of Science and Technology (NAST) and the Nepalese Department of Hydrology and Meteorology (DHM), which also supplied the discharge time series at Rabuwa Bazar. Discharge data at Periche are provided by Franco Salerno, researcher at the Italian National Council for Research, Water Research Department (CNR−IRSA). Rainfall satellite data are retrieved from the datasets that have elaborated and published by Bodo Bookhagen, researcher at the University of California, Santa Barbara (UCSB). Field data have been collected by surveys on Khumbu and Changri Nup glaciers by Politecnico di Milano and Università degli Studi di Milano. Finally, maps are downloaded from the International Centre for Integrated Mountain Development (ICIMOD).

I would like to express my gratitude to my supervisor Daniele Bocchiola for the useful comments, remarks and challenges through the learning process of this master thesis, and to my co−supervisor Gabriele Confortola for his constant and firm support in this work. Also, I am grateful to Andrea Soncini for his patient help in understanding and modelling the dynamics of a glacierised catchment, and to Umberto Minora for introducing me to remote sensing. Learning from all of you has been a true pleasure.

Heartfelt thanks goes to my family, who have always supported me throughout the studies, especially during the period abroad. To Sam, companion along the way, for encouraging me and for sharing new perspectives. Finally, I would like to thank my friends, by now spread around the world and yet providing colour to these days of hard work.

Contents

Abstract iii

Abstract iv

Acknowledgements vi

Contents vii

List of Figures xi

List of Tables xv

1 Introduction 1
- 1.1 Background of the Study and Problem Statement . . . 2
- 1.2 Review of previous studies . . . 3
- 1.3 Executive Summary . . . 5

2 Study area 7
- 2.1 Physical features . . . 7
- 2.2 Climate . . . 12
- 2.3 Flow regime . . . 13
- 2.4 Glacier characteristics . . . 14
- 2.5 Challenges . . . 16
  - 2.5.1 Glacial Lake Outburst Floods . . . 16

3 Model description 19
- 3.1 Hydrological model . . . 20
  - 3.1.1 Snow and ice melt . . . 21
    - 3.1.1.1 Temperature index model . . . 22
    - 3.1.1.2 Hybrid model . . . 23
  - 3.1.2 Evapotranspiration . . . 23
  - 3.1.3 Recharge of groundwater reservoir . . . 24
  - 3.1.4 Flow routing . . . 24
- 3.2 Finer-scale modelling over the glacierized catchment . . . 24
  - 3.2.1 Snow and clean ice melt . . . 25
  - 3.2.2 Ice melt under debris cover . . . 26
  - 3.2.3 Glacier dynamics . . . 28
  - 3.2.4 Glacial Hydrology . . . 30

4 Data and Methods **31**
4.1 Temperature . . . 32
4.1.1 Ground stations data . . . 32
4.1.1.1 Data issues and Gap filling . . . 33
4.1.2 Remote sensing data . . . 33
4.1.3 Data merging . . . 38
4.1.3.1 Lapse rate estimation . . . 38
4.1.3.2 Spatial distribution . . . 39
4.1.4 Temperature correction at high altitude . . . 40
4.1.5 Temperature distribution in the double scale modelling approach . 41
4.2 Rainfall . . . 42
4.2.1 Ground stations data . . . 42
4.2.1.1 Data issues and Gap filling . . . 43
4.2.2 Remote sensing data . . . 45
4.2.3 Data merging . . . 47
4.2.3.1 Lapse rate estimation . . . 47
4.2.3.2 Spatial distribution . . . 50
4.2.4 Precipitation distribution in the double scale modelling approach . 50
4.3 Snow . . . 51
4.3.1 Ground station data . . . 51
4.3.2 Remote sensing data . . . 53
4.3.3 Precipitation amounts correction . . . 53
4.4 Ice melt rates . . . 55
4.5 Spatial distribution of debris thickness and ice melting . . . 57
4.5.1 Landsat Imagery . . . 57
4.5.1.1 Debris cover map . . . 58
4.5.1.2 Surface temperature calculation . . . 59
4.5.2 Debris thickness estimation . . . 60
4.5.3 Ice melting and debris thickness relation . . . 63
4.6 Ice thickness and basal shear estimation . . . 64

5 Results **67**
5.1 Calibration technique . . . 67
5.2 Wider-catchment calibration and validation . . . 69
5.2.1 Snow and ice melt parameters - calibration and validation . . . 70
5.2.2 Hydrological parameters . . . 73
5.2.2.1 Model calibration . . . 73
5.2.2.2 Model validation . . . 75
5.2.2.3 Hydrograph analysis . . . 77
5.2.2.4 Goodness of fit evaluation . . . 78
5.2.2.5 Input dataset choice . . . 79
5.3 Smaller-catchment calibration . . . 80
5.3.1 Snow melt parameters calibration . . . 80
5.3.2 Ice melt parameters calibration . . . 82
5.3.3 Hydrological parameters . . . 83
5.3.3.1 Model calibration . . . 84
5.3.3.2 Model validation . . . 85

5.3.3.3 Hydrograph analysis 86
5.3.3.4 Uncertainties and Limitations 88
5.3.3.5 Goodness of fit evaluation 89
5.3.4 Glacier dynamics parameters calibration 90

6 Discussion **93**
6.1 Spatial snow cover extent 93
6.2 Rainfall Spatial Distribution 98
6.3 Comparison with previous work 100
6.4 Contributions to the river flow 102
6.5 Comparison of the simulated discharge at Periche 105
6.6 Ice melt model for the Khumbu glacier: discussion 106
6.6.1 Simulation of debris thickness and ice melt under debris cover . . . 106
6.6.2 Spatio−temporal distribution of ice melt 109
6.7 Glacier dynamics model 112

7 Conclusions **115**
7.1 Achievements 116
7.1.1 Mesoscale hydrological model 116
7.1.2 Finer scale hydro−glaciological model 118
7.2 Follow up 120

Bibliography **123**

List of Figures

2.1 Physiographic regions of Nepal and location of the study area. Source: ICIMOD. 8
2.2 Hypsometry curve of the Dudh Kosi catchment closed at Rabuwa Bazar (top) along with the hyspometry of glacierised area (bottom). From Paramithiotti (2013). 9
2.3 Digital Elevation Model at 30 m resolution for the two studied catchments. Hydro− and meteorological stations are also included, along with the glacierised area. 10
2.4 Land Cover from AVHRR satellite imagery (left) and CN (right) maps, obtained by intersection of the land cover map with the soil classifications. 11
2.5 Monthly mean and standard deviation of gauged discharge along the Dudh Kosi River: Rabuwa Bazar (left) and Periche (right) stations. . . . 14
2.6 Comparison of flow distribution over the year at different sections of the Dudh Kosi River. 14
2.7 Landsat false colours image (May 22, 2014) showing Khumbu glacier. Supraglacial ponds and lakes are evident in dark blue. 18

3.1 Discretization of the wider catchment closed at Rabuwa Bazar with 3000x3000m cells (left) and of the small catchment closed at Periche with 300x300m cells (right). Ground stations and glacier extension are also included. . . 20
3.2 Comparison between theoretical and observed daily global radiation at Kala Patthar (5600 m a.s.l.) in the available period, from 2009 to 2013. . 26

4.1 Temperature mean daily values observed at stations (blue) and after gap-filling (red). Only the stations with the greatest amount of reconstructed data are shown. 34
4.2 Comparison of monthly means (2003-2013) from ground stations and MODIS temperatures at the station location. 35
4.3 Comparison of monthly means (2003-2013) of ground stations and MODIS temperatures at the station location after the removal of data affected by cloud cover. 36
4.4 Comparison of annual means of ground stations and MODIS scenes at the station location, after the removal of data affected by cloud cover. . . 37
4.5 Lapse rate estimates for temperature annual means. Months form June to September are not included in the computation of annual means due to the low reliability determined by cloud cover. 39
4.6 Original (blue) and corrected (magenta) mean daily temperature time series from the high altitude stations. 41
4.7 Rainfall time series (blue) and gap filling (red). Daily cumulated rainfalls from ground station, 2003-2013. 44

4.8 TRMM reliability with elevation: mean annual rainfall totals from ground stations and TRMM scenes at each station's location. 45
4.9 Comparison of monthly mean cumulative rainfall from ground stations and TRMM scenes at each station's location. 46
4.10 Mean Monthly Cumulative Rainfall over the available datasets (1970-2013 for low-altitude stations, left, 2003-2013 for high-altitude stations, right). 48
4.11 Lapse rate estimation from the monthly mean cumulative rainfall for low and high altitude stations and for each season. Data from ground stations only. 49
4.12 Lapse rate estimation from the annual mean cumulative rainfall for low and high altitude stations. Data from ground stations only. 49
4.13 Comparison between snow depth recorded at Pyramid AWS in 2003−2013 and albedo calculated from Pyramid shortwave radiation in the same period. 52
4.14 Comparison of observed daily rainfall and estimated total precipitation for high altitude stations, in the period 2003−2013. 55
4.15 Landsat 7 RGB image of Khumbu glacier and debris covered area resulting from the automatic classification. 58
4.16 Surface Temperature map of the debris cover, derived from Landat 8 thermal band 10 acquired on May 22, 2014. 60
4.17 Sampled locations: the letter w indicates clean ice samples, b location on debris covered ice. 61
4.18 Empirical interpolant function for the observed debris thicknesses and the Landsat surface temperatures. 62
4.19 Debris thickness map of Khumbu glacier, derived from Landsat surface temperatures. 62
4.20 Interpolation of mean daily ice ablation under various thicknesses of debris cover, sampled over the Khumbu glacier between May and October 2014. 64
4.21 The estimated ice thickness for Khumbu glacier, assuming laminar flow and basal sliding as motion type. 65

5.1 Calibration of the degree day factor for snow: observed and simulated time series of snow depth(left) and cumulative snow height (right). . . . 70
5.2 Validation of the degree day factor for snow: observed and simulated time series of snow depth(left) and cumulative snow height (right). 70
5.3 Calibration of the hybrid model parameters: observed and simulated time series of snow depth(left) and cumulative snow height (right). 71
5.4 Validation of the hybrid model parameters: observed and simulated time series of snow depth(left) and cumulative snow height (right). 71
5.5 Calibration of the hydrological model run with the two different input datasets. The degree day method is used for the melt module. 74
5.6 Monthly mean discharge and model efficiency for the calibration period. Satellite data as input. 74
5.7 Monthly mean discharge and model efficiency for the calibration period. Ground data as input. 75
5.8 Validation of the hydrological model run with the two different input datasets. The degree day method is used for the melt module. 76
5.9 Monthly mean discharge and model efficiency for the validation period. Satellite data as input. 76

5.10 Monthly mean discharge and model efficiency for the validation period. Ground data as input. 77
5.11 Calibration of the hybrid model parameters for snow: observed and simulated time series of snow depth(left) and cumulative snow height (right) at Pyramid AWS. 81
5.12 Validation of the hybrid model parameters for snow: observed and simulated time series of snow depth(left) and cumulative snow height (right) at Pyramid AWS. The charts at top show year 2012, those at bottom year 2013. 81
5.13 Comparison of observed and simulated volumes at Periche during the calibration (left) and validation (right) periods for optimizing the radiation parameters for ice melt. Last two months of 2012 are missing. 83
5.14 Calibration of the hydrological model. The best fitting hydrograph is shown (left) along with the contributions time series used to identify the time spans where to optimize the different parameters. 85
5.15 Monthly mean discharge and model efficiency for the calibration period. 85
5.16 Validation of the hydrological model (year 2012). The best fitting hydrograph is shown (left) along with the contributions time series used to identify the time spans where to optimize the different parameters. . . . 86
5.17 Monthly mean discharge and model efficiency for the validation period. . 86
5.18 Further validation of the hydrological model (year 2013). The best fitting hydrograph is shown (left) along with the contributions time series used to identify the time spans where to optimize the different parameters. . . 87
5.19 Monthly mean discharge and model efficiency for the validation period. . 87
5.20 Mean simulated ice velocities at stakes locations against observed values. Ice velocities are intended as averages over the vertical profile of the ice section. 90

6.1 Comparison of monthly mean simulated snow depth and MODIS monthly mean snow cover, expressed in percentage of time each cell is occupied by snow, from January to June. 95
6.2 Comparison of monthly mean simulated snow depth and MODIS monthly mean snow cover, expressed in percentage of time each cell is occupied by snow, from July to December. 96
6.3 Permanent snow cover extent from ASTER imagery for year 2006. Model cells are also represented for comparison with the simulations. 97
6.4 Comparison of monthly mean simulated rainfall field and long term TRMM monthly averages in the period 2003−2005. To be compared, data are normalized with the monthly maximum rainfall total. Represented period is the monsoonal season, from June to September. 99
6.5 Simulations in 2003 − 2005 from the hydrological altitude belts model (above) and the cells based model implemented in this thesis (below). . . 101
6.6 Simulations in 2007 − 2011 from the hydrological altitude belts model (above) and the cells based model implemented in this thesis (below). . . 102
6.7 Mean monthly contributions [%] to generation of river flow at Rabuwa Bazar (left) and mean annual shares of discharge sources (right) in the period 2003 − 2011. 103

6.8 Mean monthly contributions [%] to generation of river flow at Periche (left) and mean annual shares of discharge sources (right) in the period 2011 – 2012. 104
6.9 Comparison of the two modelling approaches in simulating river discharge at Periche. 105
6.10 Simulated debris thickness at stakes locations against observed values. . 107
6.11 Comparison between simulated and observed mean ice ablation rates under debris cover and in debris−free conditions at stakes locations. 107
6.12 Comparison between simulated mean ice ablation under debris cover, observed values and interpolative functions of observed and simulated ice ablation. 108
6.13 Simulated cumulative ice ablation during 2011. 109
6.14 Simulated cumulative ice ablation during each season, in 2011. 110
6.15 Simulated cumulative ice ablation at those stakes located on clean ice. The lines preprent the simulated values (2001−2013), the dots the observations (2014). 111
6.16 Simulated ice velocity, averaged over the vertical profile and in time during year 2011. 113

List of Tables

4.1 Temperature stations network 32
4.2 Rainfall station network used in this thesis. 42
4.3 Snow densities recorded for both fresh and old snow. Density from the snowpit is averaged along depth. Six snow cores were taken, the average value for density is reported. 53
4.4 Observed debris−free ice melt rates at three locations over Changri and Khumbu glaciers. 56
4.5 Observed debris−covered ice melt rates at four locations over Khumbu glacier. 56

5.1 Optimal snow and ice melt parameters from calibration. DDS and DDI are the degree day factors for now and ice respectively, TF and SRF the temperature and solar radiation factors for the hybrid model. 71
5.2 Calibrated values for the hydrological parameters. 73
5.3 Model efficiency and error for the calibration and validation periods; comparison between the input datasets is also provided. 79
5.4 Optimal snow melt parameters from calibration. DDS is the snow degree day factor, RF_{snow} the solar radiation factor. 82
5.5 Optimal ice melt parameters from calibration. DDI is the ice degree day factor, RF_{ice} the solar radiation factor. 83
5.6 Calibrated values for the hydrological parameters. 84
5.7 Summary of efficiency indexes and model error for the calibration and validation periods. 89

6.1 Calculated glacier surface velocities from GPS positioning at stakes locations performed in May and October, 2014. 112

Chapter 1

Introduction

The Himalayas and the adjacent Tibetan–Qinghai plateau are the source of the major Asian rivers which sustain the lives of hundreds of millions of people downstream; the water stored in the Himalayan cryosphere is the third world's largest in magnitude after the polar ice caps (Immerzeel et al. 2009). Thereby preservation of these water resources is crucial. At the same time, the Himalayas are a relatively young and fragile range, thus hydrogeological hazards such as flash floods, landslides, erosion, glacial lake outburst floods have a strong impact on local communities. This study addresses these issues by providing a comprehensive modelling approach for a high altitude glacierised catchment. The major physical processes are described in order to predict the river flow at different distances from the glaciers. The study area covers the Dudh Kosi River catchment, located in the Nepalese Himalayas and part of the Sapta Koshi basin, one of the three major river systems in Nepal (Hannah et al. 2005). The Dudh Kosi River originates in a glacierised high elevation basin that comprises some of the highest peaks in the world, among which Mount Everest.

This Chapter presents the background and driving motivations behind this study and details the objectives that have been set (Paragraph 1.1). A concise summary of previous works in the study area and on similar catchments is provided in Paragraph 1.2; in particular, the focus is set on the applied methodologies in order to describe the scientific framework in which this thesis is rooted. Finally, the structure of the thesis is delineated in Paragraph 1.3.

1.1 Background of the Study and Problem Statement

Almost 800 millions people live in the catchments of the Indus, Ganges, and Brahmaputra rivers and rely to varying extents (in particular during dry seasons and in mountain valleys) on the water released from glaciers that constitute the so called Water Towers, i.e. the most extensive glacier cover outside Alaska and the Arctic (Bolch et al. 2012). Glaciers store huge amounts of water that are gradually made available, as ice melts, to downstream communities that rely on this resource for agriculture, power generation and living. In the last decades, retreating trends have been observed for glaciers (Bajracharya et al. 2007) as well as changes in precipitation patterns, which are both likely to affect the hydrological budget in the region, thus undermining water availability and increasing the frequency of flood events. Intense monsoon rainfall or cloudbursts can cause devastating flash floods in the middle mountains (500–3500 m a.s.l.), and rapid melting of snow accumulated during winter is among the main causes of flash floods in the Hindu Kush and western Himalayas (Shrestha et al. 2011). Besides, retreating glaciers are forming supraglacial lakes naturally dammed by unconsolidated moraines, which are likely to fail generating destructive flash floods in the remote, and yet highly populated, HKH region.

For these reasons, it is of paramount importance to understand and predict the hydrological and glaciological processes taking place in the Himalayan catchments. However, detailed information about the integrated hydrological system analysis is still limited, as comprehensive knowledge and data about system dynamics, such as runoff components and snow and glacier ice melt, are not available (Nepal et al. 2014). Therefore, goal of this thesis is to set up a tool for representing the hydro−glaciological behaviour of a high altitude, extensively glacierised catchment, both at the mesoscale and at the glacierised area scale.

An unprecedented comprehensive approach is adopted to study the impact of rainfalls and stored water in the glacier on discharge at different distances from the glacier tongue. Attention is given to the main elements contributing to flow generation, so that the model replicates the river flow as accurately as possible, thereby being the ideal tool for a variety of scopes, from predictions under future climatic scenarios to flood forecast. The model targets the Dudh Kosi River catchment closed at Rabuwa Bazar (3700 km^2) in Eastern Nepal and its subcatchment closed at Periche (151 km^2) and encompassing, among others, Khumbu glacier.

In detail, major objectives of the study are:

- the analysis of the spatial distribution of meteorological variables (temperature and precipitation) over the study area;
- the implementation of a semi−distributed, cell−based hydrological model for simulating flow discharge at different sections along the Dudh Kosi River;
- the assessment of the best meteorological input dataset to feed the model, between sole ground observations and assimilation of ground observations with long term satellite averages;
- the detailed modelling of distributed ice melting on Khumbu glacier, explicitly accounting for the effects of the debris cover;
- the set up of a dynamics model for Khumbu glacier.

1.2 Review of previous studies

This section presents a state-of-the-art review in order to provide the framework of this thesis and to show its scientific contributions. First, the previous work targeting the study area with a hydrological modelling approach is illustrated, along with the improvements introduced in this thesis. Afterwards, a brief summary of hydrological modelling experiences in the Himalayan region is presented and compared to the current study. Noticeably, these works date back to no farther than 2012, indicating the topicality of the treated issues.

A previous thesis (Paramithiotti 2013) implemented an altitude-belts hydrological model for the Dudh Kosi River basin closed at Rabuwa Bazar, fed by weekly satellite rainfall data and ground observed temperatures. This study upgrades the spatial distribution of the model, re−parametrizing the variables and the input data in a more flexible configuration. First, instead of short term satellite data, long term averages are used to spatially distribute meteorological parameters, so that the employment of remote sensing data does not prevent the model from being used in forecast and nowcast mode for flow prediction, as only ground observed weather data are required as daily inputs. Here, the study area is divided in cell units instead of altitude belts, allowing for a more flexible and detailed simulation of hydrological and glaciological processes. Moreover, minor refinements are introduced in this study. To begin with, rainfall is corrected for solid precipitation instead of assuming a linear decay of snowfall with elevation. Then, gap filling is performed for both temperature and precipitation gauged time series, so that

a continuous input dataset is provided to the model. Finally, snow and ice melt models are calibrated with direct observations of snow depth time series and ice ablation rates; thus, fewer parameters are left to be calibrated on the hydrograph, reducing the degrees of freedom of the simulation. Improvements are observed in the hydrograph simulation, as discussed in detail in Paragraph 6.3. Furthermore, a finer scale hydro−glaciological model is implemented over the subcatchment closed at Periche, as the availability of new data from a field survey on Khumbu glacier in 2014 allows for introducing new modules in the model. In particular, the present thesis covers the main processes involving the cryosphere, such as glacier dynamics, simulation of debris and ice thicknesses, ice ablation under clean and debris−covered conditions, usage of combined radiation and temperature models for snow and ice melt, glacial hydrology flow routines. With these integrations, the model stands for a more complete simulation and understanding of a glacierised catchment in the Himalayas.

Nepal et al. (2014) implement an hydrological model on the catchment closed at Rabuwa Bazar to understand the system dynamics and thereby predicting climate change impacts. They use a fully−distributed process oriented model accounting for groundwater flow, water storages in soil and snow, infiltration and surface runoff; they evaluate potential snow and ice melt by calibrating air temperature and soil heat flux parameters, and they obtain good agreement with the observed discharge time series at Rabuwa Bazar. The flow route and the soil−water processes they implement are surely more advanced than those that will be adopted in this thesis; however, here a semi−distributed approach is chosen in order to limit the computational effort and given the lack of soil water content data and high resolution soil maps. Further, in this study a more detailed glaciological modelling is implemented. Indeed, Nepal et al. (2014) do not map debris cover on the glacier and do not apply a specific melt module for debris covered ice; moreover, they do not simulate ice thicknesses and glacier dynamics. Further, they are not provided with high altitude automatic weather stations data, thus they need to extrapolate rainfall and temperature gradients; satellite data are not considered to spatially distribute these variables.

Immerzeel et al. (2013) apply a similar methodology as that of this thesis by implementing a high resolution glacio-hydrological model in the Langtang watershed, located in the upper Ganges basin, and in the Baltoro watershed, in the upper Indus basin. They use temperature and precipitation calibrated lapse rates to derive spatial fields at the model resolution of 90m, and calculate snow and ice melt with a degree-day approach. Due to the lack of data, they do not explicitly simulate ice melt under debris and degree days are not discriminated between snow and ice; this shows the importance of continuous and extensive field campaigning for data collecting and sharing. Similar to this thesis, glacier dynamics is accounted for basal sliding by means of Weertman's law and

gravitational snow transport processes are included as well. In the subsequent study (Immerzeel et al. 2014), melt parameters are estimated using data from ablation stake measurements on Lirung and Yala glacier, different for debris covered and debris-free glacier areas, as it is done in this thesis. While adopting the same general modelling approach, in this thesis some more elements are investigated. First, spatial distribution of meteorological variables is tackled, as it is deemed relevant in large catchments with rugged topography. Then, estimates of debris cover role in glacier balance is extensively addressed.

To sum up, this thesis introduces significant and substantial advancement in the modelling a of a remote glacierised, scarcely gauged catchment with respect to the previous work. The implemented modelling approach is substantiated by current research, yet bringing some innovation, as a thorough approach for glaciological modelling is rarely tackled. Its philosophy and general objective is to provide a comprehensive depiction of the hydrology and the cryosphere of a large glacierised basin in order to be able to simulated the discharge along the Dudh Kosi River.

1.3 Executive Summary

The modelling approach is divided into two main blocks. First, a mesoscale hydrological model is applied to the catchment closed at Rabuwa Bazar at a horizontal resolution of 3 km. Afterwards, the focus is shifted to the subcatchment closed at Periche and mostly covered by glaciers, among which there is Khumbu glacier. The adopted horizontal resolution in this case is 300 m; the hydrological model of the subcatchment is integrated with a detailed glaciological model.

Chapter 2 presents the study area, its physiographic characteristics, the climate and the flow regime. In particular, discharge seasonality is analysed at different sections along the Dudh Kosi River, in order to qualitatively assess relative weights of rainfall and melting in the river flow composition. Further, the characteristics of the glaciers in the region are outlined, with particular focus on Khumbu glacier. Finally, the main issues that currently − and likely will increasingly − affect the study area are briefly described; special attention is dedicated to the glacial lake outburst floods as relevant hazard in the region.

Chapter 3 describes the adopted modelling approach. First, the hydrological processes are studied at a large spatial scale (3700 km^2 wide catchment). The hydrological budget is used to compute runoff generation, entailing assessment of snow and ice melt, evapotranspiration, recharge of groundflow by infiltration. Two methods for melt computation

are compared, being the temperature index model and the hybrid model. Afterwards, the glaciological processes implemented on the subcatchment are presented. They encompass ice melt under debris cover, glacier dynamics and glacial hydrology.

Chapter 4 illustrates the input data and their elaboration. Collected data mainly consist of meteorological variables from ground stations and satellite scenes, and of physical properties of the Khumbu glacier. First, gap filling, spatio−temporal distribution and merging with satellite data is carried out for temperature and rainfall; snow ground and satellite data are described, along with the correction of precipitation amounts at high altitudes. Ice melt rates are calculated from observed ice thickness variations, and the procedures for mapping debris cover extent and estimating their thickness is then illustrated. Finally, distributed ice thickness estimatio is carried out for the Khumbu glacier.

Chapter 5 treats the model calibration and validation procedure and shows the results in terms of simulated discharge, efficiency indexes and simulated snow depth and ice velocities. First, the results for the mesoscale hydrological model closed at Rabuwa Bazar are presented, then those for the subcatchment closed at Periche.

Chapter 6 discusses some interesting insights provided by the model on the hydrology of the catchment. Model performance in representing snow cover extent and rainfall spatial distribution is tested by comparison with satellite averaged data. The modelling approach is also assessed by comparing the simulated discharge series at Rabuwa Bazar with that resulting from the altitude belts model; further, discharge simulation at Periche is confronted between the mesoscale hydrological model and that run on the subcatchment. Cumulative ice ablation at stakes locations is analised. Hydrological contributions to river flow both at Rabuwa Bazar and Periche, and spatial distribution of ice melt and ice velocities are also analysed, as examples of valuable information that can be obtained from the model in a remote scarcely gauge basin.

Chapter 7 closes the study by showing the major achievements of this thesis along with its limitations and suggestions to overcome them; potential uses of the set up model are also indicated.

Chapter 2

Study area

The Dudh Kosi River belongs to the Sapta Koshi river system, which drains Eastern Nepal (Figure 2.1). It originates in the Mount Everest massif and flows across High Mountainous and Mountainous regions in the Nepalese Himalayas. The upper part of the catchment belongs to the Sagarmatha National Park and contains several glaciers, of which the Ngozumpa and Khumbu glaciers are the biggest. In this thesis, two sub-catchments are targeted; first, the focus is set on the Dudh Kosi River basin closed at Rabuwa Bazar, about 90 km downstream the head of the river. Then, the basin is closed far northern at Periche, only 3.7 km south to the Khumbu glacier tongue (Figure 2.3). In this way, it is possible to address the different features of the hydrological budget in the region.

This Chapter describes the physical characteristics of the study area (Paragraph 2.1), its climate (Paragraph 2.2) and flow regime (Paragraph 2.3). Further, the features of the glaciers in the region are presented (Paragraph 2.4), with a particular focus on the Khumbu glacier as it will be the target of the model. Finally, the most relevant challenges that the region is facing are summarized (Paragraph 2.5).

2.1 Physical features

Nepal is located north to India and south to China, with a relatively small latitude extent; it is 885 km east-west wide and about 200 km north-south large. Altitude rises from 60 m a.s.l. in the south to 8848 m a.s.l. in the north at Mt. Sagarmatha (Qomolangma or Everest), the highest peak in the world; physiographicaly, Nepal is divided in five regions (Plain, Hills, Middle and High Mountains, High Himalayas), as shown in Figure 2.1. The study area is located in the highest elevation region, in the

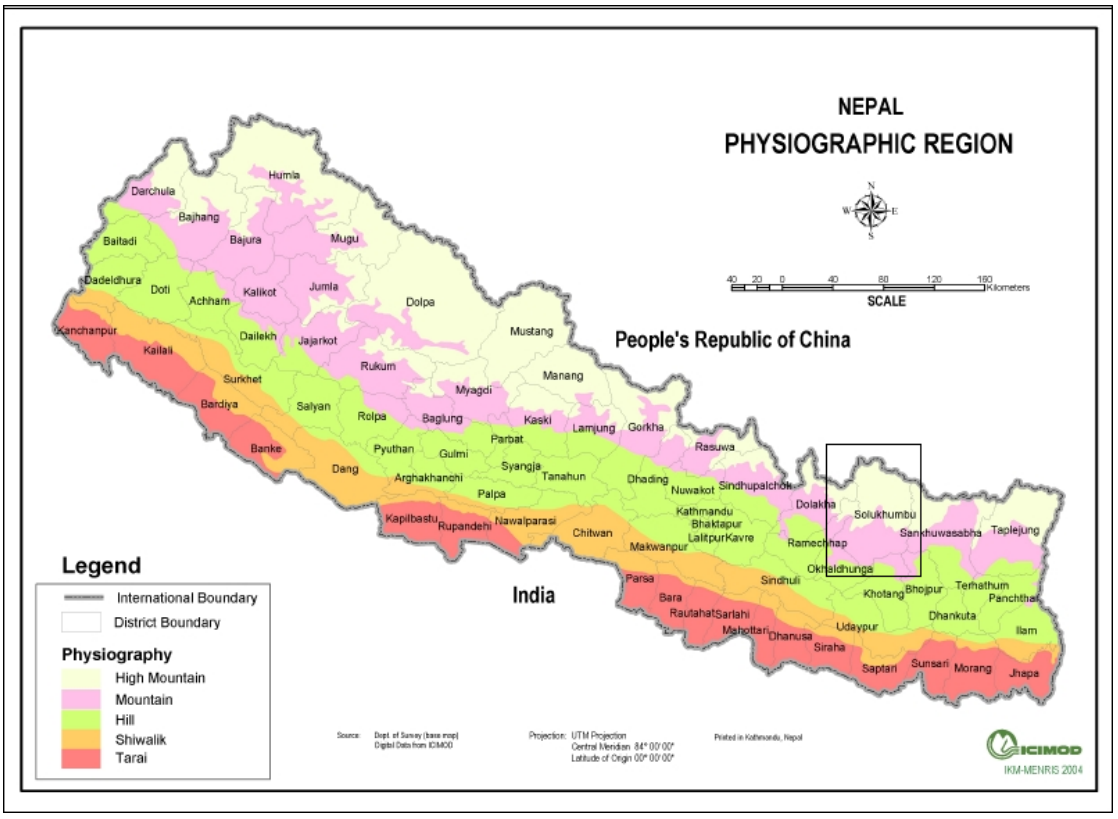

Figure 2.1: Physiographic regions of Nepal and location of the study area. Source: ICIMOD.

Himalayas. In central Himalayas, the mean topographic profile is characterized by a two step morphology, of which the outer step correspond to the Lesser Himalaya and the inner step to the Higher (Greater) Himalaya geologic unit (Bookhagen & Burbank 2010).

The Dudh Kosi catchment closed at Rabuwa Bazar covers an area of 3700 km^2 and a wide range of altitudes; minimum elevation is 480 m a.s.l., whereas the maximum amounts to the 8848 m a.s.l. of Mount Everest peak. The two−steps topography is evident from the hypsometry of the catchment (Figure 2.2). The first peak occurs at 2000 to 3700 m a.s.l., encompassing about 30% of the total area; the second peak takes place between 4300 and 5600 m a.s.l., with 32% of the catchment area; one third of the basin is located above 5000 m a.s.l.. The distribution of glacierised area against elevation is also shown in Figure 2.2. Glaciers are present between 4900 and 7500 m a.s.l., but mostly concentrated between 4800 to 6000 m a.s.l.; glacial area amounts to 25% of total area. Remarkably, a great fraction of the glacierised area is located at low altitudes, which may expose the glaciers to significant melt rates due to relatively high temperatures. The sub catchment closed at Periche extends to an area of 151 km^2; of these, 85.32 km^2 (56% of total area) is covered by glaciers. Elevation ranges from a minimum of 4230 m a.s.l. at Periche to 8848 m a.s.l. of Mount Everest.

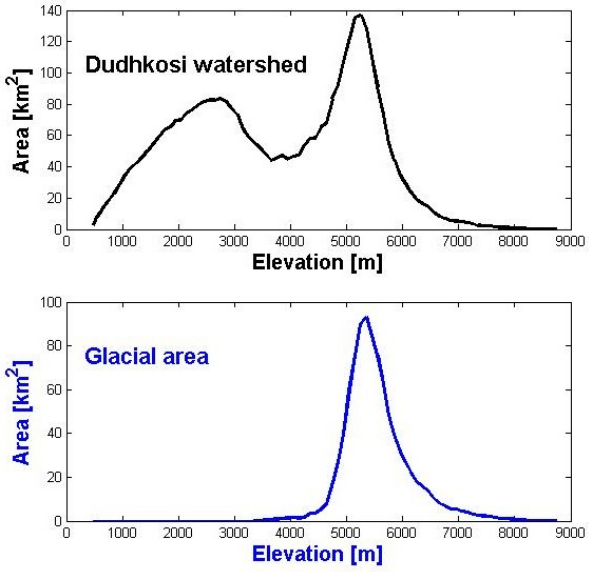

Figure 2.2: Hypsometry curve of the Dudh Kosi catchment closed at Rabuwa Bazar (top) along with the hyspometry of glacierised area (bottom). From Paramithiotti (2013).

Figure 2.3 shows the two sub catchments that will be studied in thesis. A 30 m x 30 m horizontal resolution Digital Elevation Model has been retrieved from the U.S.G.S.[1]. The glacier extent is retrieved from the glacier inventory prepared by ICIMOD in the form a shapefile[2].

Digital soil data of the study area are extracted from the FAO soil global dataset[3] , having cell resolution of approximately 10 km; the hydrological soil group to be assigned to each cell for CN estimation results to be D Mishra et al. (2008), corresponding to the most impervious soil type. The land cover map is retrieved from the global land cover classification made at the University of Maryland, Department of Geography, in 1998[4]. The land cover dataset has been prepared from AVHRR satellite imagery acquired between 1981 and 1994 at resolution of 1 km, and classifies cover types in 14 categories (Figure 2.4). From these datasets, the CN map of the study area has been prepared and compared with (Mishra et al. 2008), who provide a CN-based hydrological regionalization of Nepalese river basins. Figure 2.4 shows the land cover map and the calculated CN over the study area. CN dataset for the sub catchment closed at Periche is extracted by these ones.

[1]Available at http://gdex.cr.usgs.gov/gdex/ [Accessed 15th November 2014].

[2]Available at http://geoportal.icimod.org/indusbasin/Downloads/ [Accessed 15th November 2014].

[3]Available at http://www.fao.org/soils-portal/soil-survey/soil-maps-and-databases/regional-and-national-soil-maps-and-databases/en] [Accessed 12 February 2014].

[4]Hansen, M., R. DeFries, J.R.G. Townshend, and R. Sohlberg (1998), UMD Global Land Cover Classification, 1 Kilometer, 1.0, Department of Geography, University of Maryland, College Park, Maryland, 1981-1994. Available at http://glcf.umd.edu/data/landcover [Accessed 11 February 2014].

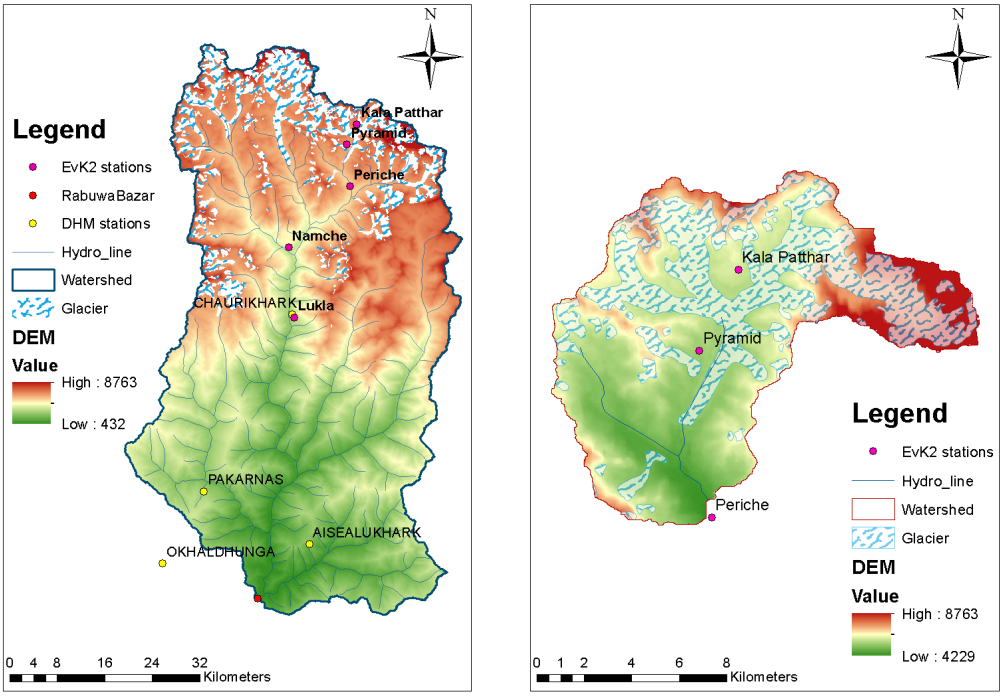

(a) Catchment closed at Rabuwa Bazar

(b) Catchment closed at Periche

Figure 2.3: Digital Elevation Model at 30 m resolution for the two studied catchments. Hydro− and meteorological stations are also included, along with the glacierised area.

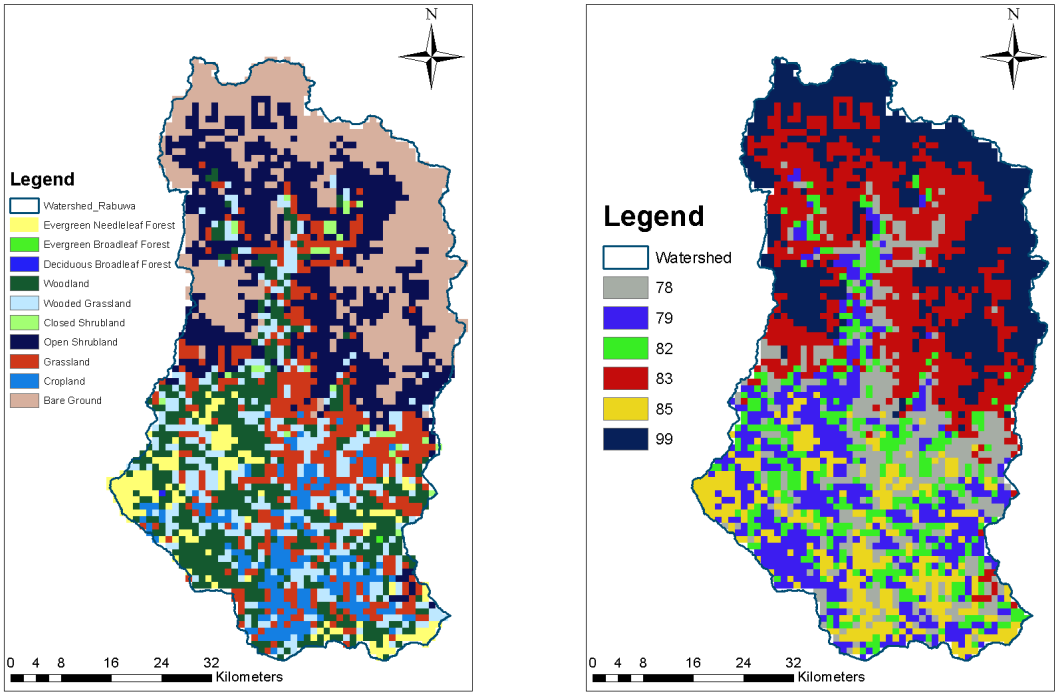

Figure 2.4: Land Cover from AVHRR satellite imagery (left) and CN (right) maps, obtained by intersection of the land cover map with the soil classifications.

2.2 Climate

The climate in the Hindu Kush Himalayan region is strongly influenced by the varying dominance of two independent climatic systems, i.e. the Asian monsoon and westerly winds. In particular, Central and Eastern Himalayas are mainly influenced by the Asian Monsoon pattern, the more the closer to the Indian Ocean, where the monsoon originates (Bookhagen & Burbank 2010). In summer, monsoonal vortexes form over the Bay of Bengal and generate heavy rainfall as they are forced towards the orographic barrier posed by the Himalayas range; therefore, eastern regions of Nepal are hit by larger amounts of rain. In winter, the extremely low temperatures over the Tibetan Plateau cool air masses and originate a pressure gradient by attracting warmer air masses from the ocean, thereby installing a north-eastern wind system.

In the study area, four seasons can be identified related to the precipitation (e.g. Immerzeel et al. (2014), Hannah et al. (2005)), as timing and amount of precipitation are governed by the annual monsoon system. The premonsoonal season (March to May) is characterized by dry weather, relatively high temperatures and limited cloud cover. The monsoon generally onsets in June, and rainfall is observed almost every day; around 80% of annual rainfall occurs during summer monsoon, from June to September. In the post-monsoonal season (October to November) the rainfall activity is substantially reduced; winter (December to February) is generally dry, with occasional precipitation related to the western circulation.

However, topography has a profound effect on spatial patterns of precipitation both globally and regionally. Mountains influence the flow of air and disturb the vertical stratification of the atmosphere by acting as physical barriers and as sources or sinks of heat (Barros et al. 2000). At the scale of entire mountain ranges (hundreds of km) the rain-shadow effect has a well-documented and significant influence on precipitation patterns (Anders et al. 2006), such as forced air masses ascent on the windward side, warming the air above them, drawing air from low levels up and triggering condensation or convection on the slopes. Barros et al. (2000) studied orographic precipitation in a limited, highly gauged region of the central Himalayas, revealing large gradients in seasonal precipitation totals over short (10 km) spatial scales that are not simply related to elevation. However, existing rain-gauge networks, especially in mountainous areas, are generally not dense enough to reveal variability in precipitation over spatial scales of tens of kilometres (Anders et al. 2006).

As a result, in the Himalayan foreland and at low and moderate altitude, i.e. in the lower part of the study area, precipitation is dominated by the Indian monsoon seasonal pattern (Bookhagen & Burbank 2010). Precipitation in the upstream, higher elevation

parts of the catchment falls as snow, posing a challenge in correctly quantifying the volumes and thus the seasonal patterns (see Paragraph 4.3.3 for further discussion). Nevertheless, it is evident that the steep rise in topography sensibly reduces rainfall amounts at higher elevation (Paragraph 4.2).

2.3 Flow regime

The flow regime of Himalayan rivers is strictly connected with the Indian summer monsoon, and without exception the Dudh Kosi River reflects the seasonal precipitation patterns. Thus, discharge peaks during the summer monsoon, meaning that sustained high flows are observed in July, August and September; part of summer discharge is expected to derive from ice and snow melt water as well. After the monsoon, river flow slowly decreases, as melting may still occur; the lowest flows are observed during winter months, when little or no rain falls in the lower part of the catchment and snowfall at high altitudes delays the runoff. Finally, the spring premonsoonal season correspond to the rising limb of the annual hydrograph, as snow − and to a lesser extent ice − melt takes place. Paragraph 6.4 further discusses the seasonal compositions of discharge, corroborated with results from simulations.

Two datasets of hydrometric levels for the Dudh Kosi River are available within the study area, i.e. those gauged at Rabuwa Bazar and at Periche (Figure 2.3). Rabuwa Bazar time series covers the years from 2003 to 2011, missing the year 2009, whereas discharge at Periche is only available from 2011 to 2013. Rabuwa Bazar belongs to the Nepalese Department of Hydrology and Meteorology network, whereas Periche stages are monitored by the italian CNR. Figure 2.5 shows the mean monthly discharges at these stations, along with the respective standard deviations; Figure 2.6 compares the discharge distribution over the year at the two gauged sections of Dudh Kosi River.

At both sections, a strong seasonal pattern is observed, with highest flows during summer (June to September) and lowest discharge in late winter−early premonsoonal season. Mean monthly flows in the postmonsoonal season are more relevant at Periche than downstream at Rabuwa Bazar. Moreover, monthly discharge at Periche displays lower inter annual variation than at Rabuwa Bazar, as it can be seen by the lower standard deviation in Figure 2.5. These observations are related to the different discharge composition at the two stations, that will be discussed in Paragraph 6.4. For instance, the differences in standard deviation are likely due to the fact that summer discharge at Rabuwa Bazar is mainly originated by rainfalls, thereby being subjected to stronger and quicker variations than the flow at Periche, dominated by ice melt; for the same reason, less seasonal variation is observed in the mean monthly discharge recorded Periche.

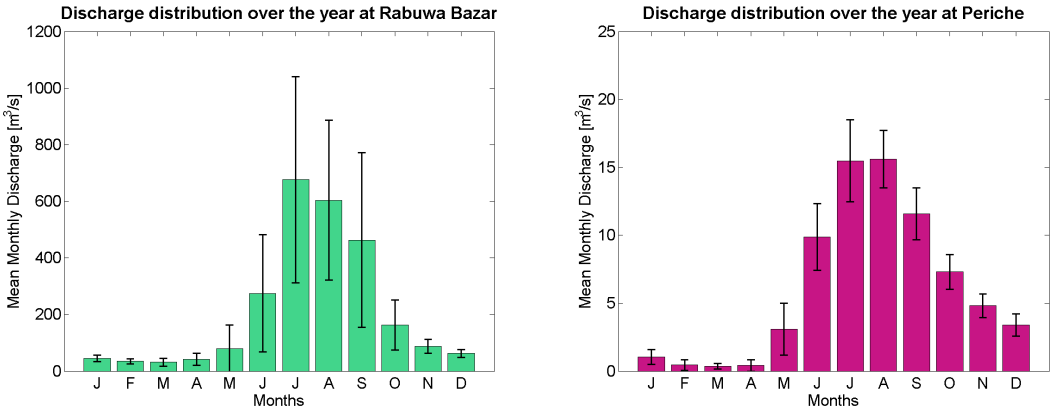

Figure 2.5: Monthly mean and standard deviation of gauged discharge along the Dudh Kosi River: Rabuwa Bazar (left) and Periche (right) stations.

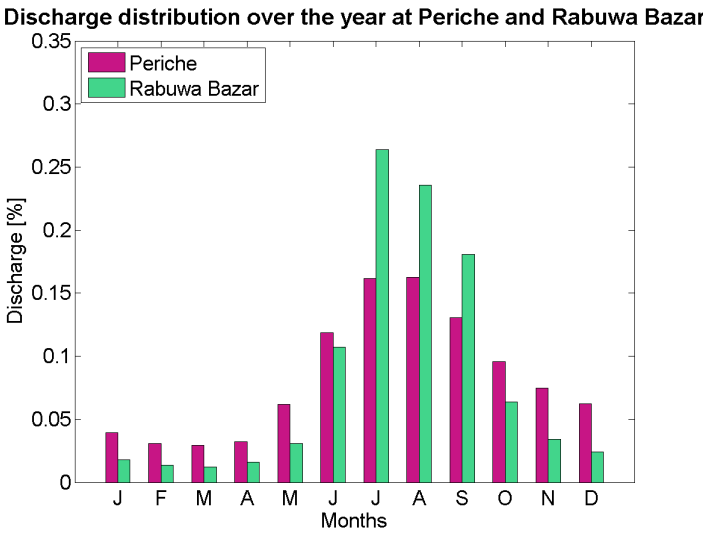

Figure 2.6: Comparison of flow distribution over the year at different sections of the Dudh Kosi River.

In conclusion, seasonal discharge patterns are observed along the entire Dudh Kosi River; however, river flow at higher altitudes shows lower variation during the year than that at lower altitudes, where discharge is strictly related to the monsoonal precipitation seasonality.

2.4 Glacier characteristics

One of the most conspicuous morphological features on the southern slope of the Himalayan Mountains is the abundance of debris−covered glaciers (Watanabe et al. 1986), as a consequence of the steep rocky terrain and in situ morphological processes. The

study area comprises several glaciers, of which the Khumbu (15 km long) and Ngozumpa (18 km long) are the biggest; in addition, there is a large number of small glaciers and glacier-like features, such as rock glaciers. The finer scale, glaciological model is applied to a smaller catchment closed at Periche (Figure 2.3), thereby focussing the analysis on the Khumbu and Changri Nup glaciers, because of the exceptional availability of field and meteorological data over these glaciers. As a matter of fact, more glaciological research has been undertaken on their ablation area than on any other debris-covered glacier in the Himalayas (Benn et al. 2012).

Khumbu glacier is a typical Himalayan valley glacier, having a 11 km long and almost 1 km wide debris covered tongue, bounded by massive moraine ridges. It is fed mainly by the snow fields located between Mount Everest, Lhotse (8511 m) and Nuptse (7861 m); the main accumulation zone (named West Cwm) lies on the south−west slopes of Mount Everest and feeds the ablation zone throughout the Khumbu Icefall just above the Everest Base Camp (5300m a.s.l.). The upper limit of the glacier is around 6800 m a.s.l., on the south west face of Mt. Sagarmatha (Qomolangma or Everest, 8848 m) and 7500 m on the west face of Lhotse (8511 m); the altitudes of the equilibrium line and the glacier terminus are about 5600 m and 4900 m, respectively (Figure 2.3, Watanabe et al. (1986)). The low elevation of the terminus, along with the low latitude of the area, exposes the glacier to relevant ablation rates; indeed, Nakawo et al. (1999) report the active terminus being about 3 km upstream the apparent one.

In the upper part of the glacier, ablation occurs by melting of bare ice and ice under the thin debris cover. At 5-7 km from the terminus, dominant ablation around the supraglacial lakes and streams occurs, in addition to inactive ice melting under the debris cover (Watanabe et al. 1986). In the downstream area of the glacier, the thick debris cover protects the ice from ablation, though slight melting can occur in subglacial or englacial channels, thus the glacier ice in this terminal zone is slowly diminishing in volume (Nakawo et al. 1999). Khumbu glacier, as most glaciers in the eastern and central Himalayas, belong to the summer-accumulation type, gaining mass mainly from summer-monsoon snowfall (Bolch et al. 2012); the basin is thus characterized by synchronous accumulation and ablation during the monsoon season. On the other hand, in this thesis it will be shown that ice melt is not limited to the summer season, even though it is more pronounced at that time (Chapter 6).

In the study area, it has been calculated (see Paragraph 4.5) that glaciers extend over about 85.32 km^2 (56% of total area), of which 38.25 km^2 (45% of glaciered area) are covered with debris. Therefore, debris melting is treated explicitly and separately from clean ice melting, as it is acknowledged that debris cover deeply influence glaciers' evolution.

2.5 Challenges

Understanding the hydro−glaciological budget of Himalayan catchments is of foremost importance for anticipating present and future hazards and criticalities. Many elements suggest that hazard levels are increasing in the Everest massif region, possibly as a consequence of climate change. Indeed, many glaciers exhibit features that indicate recent downwasting and glacial lakes formation, such as surface ponding and exposed inner lateral moraine flanks; particularly impressive are those visible on Khumbu glacier from photos and satellite images. Several Glacial Lake Outburst Floods have been observed in past decades, some of them hitting local activities and population. Further, Fukui et al. (2007) estimate that permafrost lower limit in the region has risen 100 to 300 m in altitude between 1973 and 1991.

Barnett et al. (2005) analyses the possible impacts on flow regime in the Hindu Kush Himalayan rivers, which depend at different degrees on ice melt as water source. In the HKH region they observe a regression of the maximum spring stream flow period in the annual cycle of about 30 days, and an increase in melt runoff of about 35%. Indeed, for the Dudh Kosi catchment, Paramithiotti (2013) shows a decrease in the spring rising limb of the annual hydrograph, and an increase in the post monsoon season. As a result, in the future water shortages may occur in the spring season, while floods may harness local communities during the monsoonal and postmonsoonal seasons, with implications for both food security and human safety. Combined with the exceptional population living in the HKH area (about 50% − 60% of world population), these considerations stress the importance of thorough, reliable hydrological modelling of high altitude catchments in the Himalayas.

A major issue in addressing these challenges is the leading uncertainties mainly attributed to deficient information in high altitude regions; extensive field campaigns and permanent meteorological stations are fundamental for modelling the hydrological and glaciological behaviour of the basin. In the Khumbu region such data are being collected, thereby allowing a comprehensive, unprecedented modelling of a Himalayan catchment.

2.5.1 Glacial Lake Outburst Floods

This section deepens the Glacial Lake Outburst Floods (GLOFs) phenomenon as it is recognized that a major natural hazard in the Himalayas is posed by retreating glaciers forming supraglacial lakes (Bajracharya et al. 2007). Indeed, it is important to study glaciers' state not only for assessing water availability in the downstream communities, but also for monitoring natural risks.

ICIMOD reports that all of the valley glaciers in the Dudh Koshi subbasin that could be studied are retreating by at least 10 to 59 m per year; the glaciers show a remarkable change from the 1960s to 2001. In general, glaciers are shrinking and valley glaciers are retreating. Consequently, an increasing number of moraine−dammed lakes are forming. In particular, Khumbu glacier retreated at a mean rate of 20 m/y between 1960–2001, decreasing in length from 12.040 km to 11.198 km (Bajracharya et al. 2007).

Ice cored moraines and the generation of supraglacial melt are key characteristics of debris covered glaciers (Casey 2011), since they progressively form as the glacier melts and moraines act as natural dams by preventing water from leaving the glacier. Benn et al. (2012) recognise a fundamental distinction between two types of supraglacial lakes, according to their elevation relative to the base level of the glacial hydrological system. Perched lakes are located above the level at which water leaves the glacier and may drain through englacial conduits within the ice sheet. In contrast, base-level lakes are located at the elevation at which water leaves the glacier. Such lakes will persist as long as the moraine dam remains intact, thus involve potential catastrophic outbreaks. At present, a number of large lakes and surface ponds exist in the study area (Figure 2.7). From Landsat images, Khumbu's tongues appears to be scattered with ponds, and a lake can be observed in the valley to the right of Kala Patthar.

Several glacial lake outburst floods (GLOFs) have occurred in the Everest region in the recent past, causing significant erosion and loss of agricultural land, settlements, infrastructures and power plants. The major recorded events have occurred in 1977, 1985, 1998, with peak discharges reaching $1500 - 2300$ m^3/s few km downstream the breaches, i.e. 6 to 70 times the normal climatic floods (Cenderelli & Wohl 2001); such frequency and magnitude highlight the need for further studies on natural hazards in Nepal. From high resolution satellite images, it is evident that glaciers in the Everest region present several supraglacial lakes and ponds, displaying an increasing trend in number and extension with time (Bajracharya et al. 2007); this suggests an increase in hazard level for the Dudh Kosi and similar Himalayan catchments. Twelve of the glacial lakes in the Dudh Koshi basin have been classified as potentially dangerous, the largest number in any sub-basin of Nepal studied so far (Bajracharya et al. 2007); all twelve potentially dangerous glacial lakes are moraine dammed lakes, i.e. possibly evolving in catastrophic outbursts.

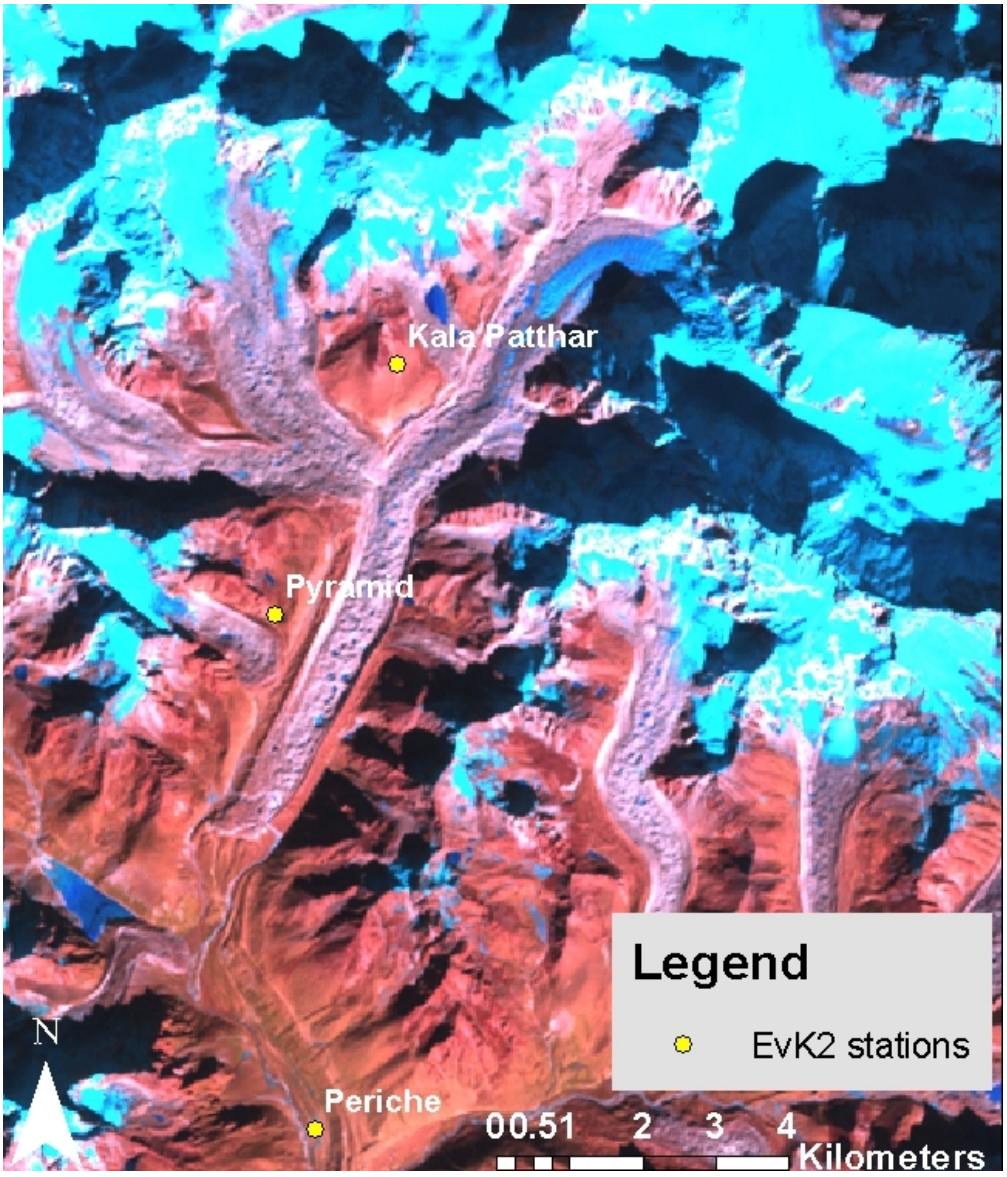

Figure 2.7: Landsat false colours image (May 22, 2014) showing Khumbu glacier. Supraglacial ponds and lakes are evident in dark blue.

Chapter 3

Model description

Purpose of the study is to simulate the main processes occurring in the glacierized catchment, leading to flow generation and glacier evolution. This will allow for the understanding of the interactions between the multiple components of the system and thereby predicting its response to any sequence of events. Different approaches are available to the hydrologist, ranging from empirical (black-box) models, establishing a mathematical relation between inputs and outputs, to white-box models, which in turn analytically describe the physics of the system. By their nature, black-box models consider the system as a single unit (lumped models), while white-box models distribute and vary the parameters dividing the system in multiple cells (Jajarmizadeh & Salarpour 2012).

In this thesis, a grey-box (conceptual) model has been implemented, as it relates inputs and output by parametrizing the physical processes. This approach realizes a compromise between the need for a physically-based understanding of the system and the large amount of data and computational costs required for a mechanistic white-box model. The model can be classified as semi-distributed, as the study area has been divided in cells; the runoff generated at each cell is directly routed to the outlet, thereby the modelling approach is not fully-distributed.

The spatial resolution has been chosen in order to capture the spatial variability of the processes while limiting the computational efforts. Thus, two different scales have been used, with different purposes. First, the hydrological model is run over the wider catchment closed at Rabuwa Bazar (3717.7 km^2), divided in 3000 x 3000 m cells. Afterwards, the focus is shifted to the cryosphere, in order to thoroughly describe the processes over Khumbu glacier. Being the glacier at maximum 1 km wide, a finer scale (300 x 300 m cells) is implemented over a smaller catchment (151.8 km^2) closed at Periche (Figure 3.1). Daily temporal resolution is used in the simulation.

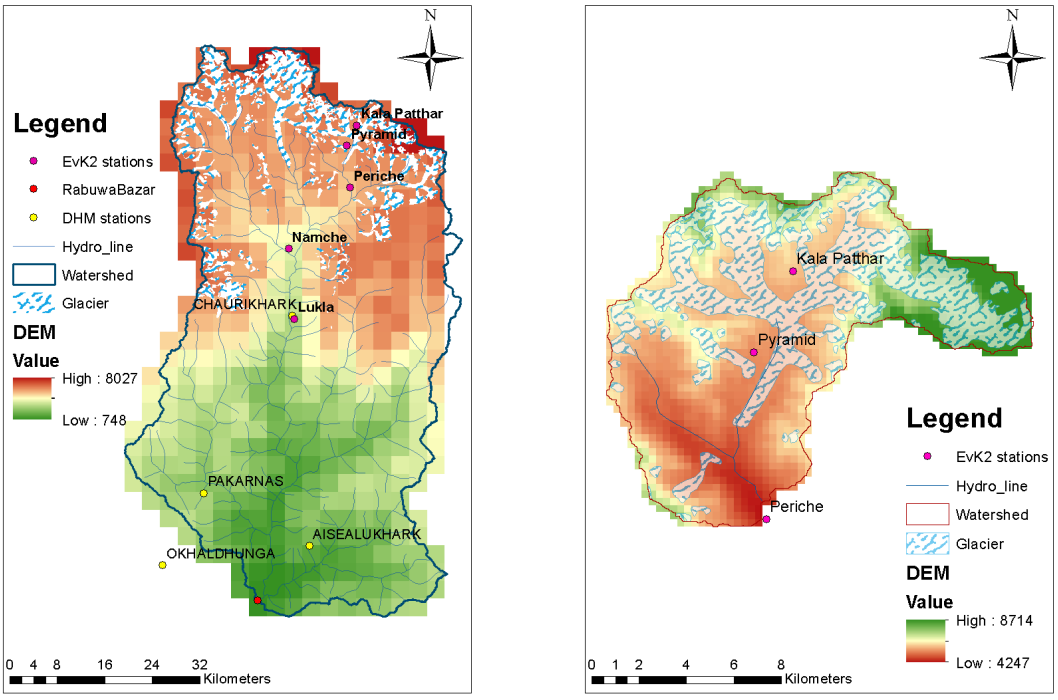

Figure 3.1: Discretization of the wider catchment closed at Rabuwa Bazar with 3000x3000m cells (left) and of the small catchment closed at Periche with 300x300m cells (right). Ground stations and glacier extension are also included.

This chapter illustrates the components of the double−scale modelling approach; Section 3.1 describes the general hydrological model, whereas Section 3.2 the additional modules simulating the cryosphere at finer scale.

3.1 Hydrological model

The hydrological model is derived from the Distributed Hydrological Model (DHM) (Wigmosta et al. 1994, Chen et al. 2005, Groppelli et al. 2011). It is based on the mass balance of the water content in the ground between two consecutive time steps:

$$S^{t+\Delta t} = S^t + R + M_i + M_s - ET - Q_g \tag{3.1}$$

where S is the soil water content, R the liquid precipitation, M_s the snow melt, M_i the ice melt, ET the actual evapo-transpiration and Q_g the groundwater discharge. The time step Δt is 24 hours. The surface runoff Q_s is then generated for each cell when the

maximum soil water content S_{max} is exceeded (eq.(3.2)):

$$\begin{aligned} Q_s &= S^{t+\Delta t} - S_{max} && \text{if} \quad S^{t+\Delta t} > S_{max} \\ Q_s &= 0 && \text{if} \quad S^{t+\Delta t} \leq S_{max} \end{aligned} \tag{3.2}$$

S_max is evaluated for each cell according to the Curve Number (SCS-CN) method proposed by the USGS (1986):

$$S = S_0 \left(\frac{100}{CN} - 1 \right) \tag{3.3}$$

where S_0=254mm. The CN parameter is estimated from the land cover map prepared from AVHRR satellite imagery[1] and soil data prepared by FAO[2]. Figure 2.4 shows the land cover and CN maps, obtained by intersection of land cover and soil grids. The values of CN for each hydrological soil group and land cover have been validated with those obtained by Mishra et al. (2008), who provide a CN-based hydrological regionalization of Nepalese river basins.

3.1.1 Snow and ice melt

The cumulated snow in each cell is calculated as:

$$SWE^{t+\Delta t} = SWE^t + P_{snow} - M_s - ET_{eff\ snow} \tag{3.4}$$

where SWE is the snow water equivalent [mm], P_{snow} the solid precipitation, M_s the snow melt and $ET_{eff\ snow}$ the effective evapotranspiration from snow:

$$ET_{eff\ snow} = 0.2\ ET_p \tag{3.5}$$

where the potential evapotranspiration ET_p is illustrated in Paragraph 3.1.2. Solid precipitation is rainfall falling below the freezing temperature; Paragraph 4.3.3 describes how snowfall amounts are calculated.

The ice mass balance at each time step is given by:

$${h_{ice}}^{t+\Delta t} = {h_{ice}}^t - M_i \tag{3.6}$$

The following Paragraph illustrates the calculation of the melt rates M_s and M_i [mm/d].

[1]Hansen, M., R. DeFries, J.R.G. Townshend, and R. Sohlberg (1998), UMD Global Land Cover Classification, 1 Kilometer, 1.0, Department of Geography, University of Maryland, College Park, Maryland, 1981-1994. Available at http://glcf.umd.edu/data/landcover [Accessed 11 February 2014].

[2]Available at http://www.fao.org/soils-portal/soil-survey/soil-maps-and-databases/regional-and-national-soil-maps-and-databases/en] [Accessed 12 February 2014].

Surface melt amounts M_s can be calculated by means of two different approaches: physical energy-balance models and empirical temperature-index models. The former quantifies melt by simulating the energy fluxes between surface, atmosphere and cryosphere, thus requiring a considerable amount of data to characterize the meteorological variables (Pellicciotti et al. 2005). The latter assumes an empirical relation between melt and air temperature as sole explicative variable. Many studies have revealed a high correlation between melt and positive air temperature sums (Hock 2003), thereafter the temperature-index model has been widely used due to its simplicity and the wide availability of temperature data. However, it has been acknowledged that at high altitude the incoming solar radiation generates meltwater at temperatures below the freezing level (Bookhagen & Burbank 2010). Therefore, in this study both the temperature-index and the temperature-index and radiation (hereafter hybrid) model are alternatively implemented for simulating snow and ice melt.

3.1.1.1 Temperature index model

According to the temperature-index method, the snow or ice melt produced within a time step is proportional to the cumulated positive temperatures during that period. The proportional factor, named *degree day factor* (DDF), lumps the complex processes of heat transfer at the surface of the glacier or snow pack. Typically, the degree day for ice is higher than that for snow at the same site, due to the higher albedo of the latter, which determines the absorption of a lower amount of energy. The model assumes the form:

$$M = \begin{cases} DDF(T - T_0) & \text{if} \quad T > T_0 \\ 0 & \text{if} \quad T \leq T_0 \end{cases} \tag{3.7}$$

where M is the rate of snow or ice melt $[mm/d]$, DDF the degree day factor, T the air mean daily temperature and T_t the threshold value above which the melt is assumed to occur. In this study, T_t has been taken as $-5°C$ in order to account for the aforementioned melt occurring below the freezing level; refer to Paragraph 5.2.1 for further details. The degree day factors are considered constant over time and space. Indeed, spatial variations are expected over the study area due to differences in elevation, shading and surface covers. However, the spatial resolution of the model does not allow for resolving these variations in the wider catchment, nor the effects of the debris cover; these are implemented for the finer scale model (Paragraph 3.2.2).

In this thesis, the degree day factor for snow is calibrated from the observed cumulated snow at one location and validated with the MODIS satellite snow product. Conversely, the degree day factor for ice is derived from actual ablation rates measured over the Khumbu glacier; the procedure is detailed in Paragraph 4.4.

3.1.1.2 Hybrid model

This type of snow and ice melt models attempts to keep the simplicity of the degree day approach and at the same time to provide a more physical representation of the surface energy balance. The most common addition to temperature index models has been the incorporation of measured shortwave radiation or net radiation (see Konz 2009, Martinec 1989, Brubaker et al. 1996). The approach used in this thesis follows Pellicciotti et al. (2005), who propose a hybrid temperature-radiation model that separates the temperature-dependent and temperature-independent contributions to melt, as shown in eq. (3.8):

$$M = \begin{cases} TF\mathrm{T} + SRF(1-\alpha)G & \text{if} \quad T > T_t \\ 0 & \text{if} \quad T \leq T_t \end{cases} \tag{3.8}$$

where TF and SRF are two empirical coefficients, G the incoming shortwave radiation $[W/m^2]$, T the air mean daily temperature, T_t the threshold air temperature for melting and α is the albedo, computed as ratio of outgoing and incoming shortwave radiation. The value assigned to T_t is discussed in Paragraph 5.2.1.

3.1.2 Evapotranspiration

Several methods have been developed in order to model the potential evapotranspiration in semi-arid environments (Weiß & Menzel 2008). In this study, the Hargreaves formulation is adopted:

$$ETP = 0.0023\ S_0\ \sqrt{\delta_t}\ (T + 17.8) \tag{3.9}$$

where S_0 is the water equivalent of extraterrestrial radiation $[mm/d]$, T the mean daily air temperature $[°C]$, δ_t the mean monthly temperature excursion $[°C]$. The variable S_0 accounts for the effects of climatic conditions at a definite time and location. However, given the scarcity of the data for a high-altitude basin, it is evaluated from geographical quantities and kept constant. The potential error derived by this simplification is deemed to be irrelevant, as the evapotranspiration does not play a key role in the mass balance of a high-altitude glacierized catchment (Bookhagen & Burbank 2010).

Subsequently, the actual evapotranspiration ET is computed as summation of the effective evaporation from the ground, E_s, and the effective transpiration from the vegetation, T_s. Both these quantities are functions of the potential evapotranspiration, depending on the water content of soil θ and the fraction of vegetated soil over the basin:

$$E_s = \alpha(\theta)\ ETP\ (1 - f_v) \tag{3.10}$$

$$T_s = \beta(\theta)\ ETP\ f_v \tag{3.11}$$

$$\alpha(\theta) = 0.082\ \theta + 9.173\ \theta^2 - 9.815\ \theta^3 \tag{3.12}$$

$$\beta(\theta) = \begin{cases} \frac{\theta-\theta_w}{\theta_l-\theta_w} & \text{if} \quad \theta > \theta_w \\ 0 & \text{if} \quad \theta \leq \theta_w \end{cases} \tag{3.13}$$

$$ET = E_s + T_s \tag{3.14}$$

where θ_w is the wilting point water content, θ_l the water content at field capacity and θ derives from the ratio $S/Smax$. Lacking any observations, the values of θ_w and θ_l are set from literature to 0.15 and 0.35 respectively, not to further increase the number of parameters requiring calibration.

3.1.3 Recharge of groundwater reservoir

The flow Q_g recharging the groundwater reservoir by infiltration is calculated as a function of the soil water content S and the hydraulic conductivity K (Chen et al. 2005):

$$Q_g = K \left(\frac{S}{S_{max}} \right)^{k_g} \tag{3.15}$$

where K and the exponent k_g are calibrated from the hydrograph.

3.1.4 Flow routing

The mass balance (eq. (3.1)) is evaluated for each cell at each time step. The generated stream discharge is then routed to the outlet by means of a semi-distributed flow routing algorithm (Groppelli et al. 2011). The Nash linear cascade of reservoirs algorithm is chosen, assuming two parallel linear systems (one for groundwater and one for surface). Each system is composed by a number of reservoirs and is characterized by a time constant. These parameters are calibrated from the hydrograph. In particular, the surface reservoirs' parameters are calibrated with the peaks of the observed hydrograph, while the groundwater ones with its low-flow parts.

3.2 Finer-scale modelling over the glacierized catchment

A thorough description of the physics of the cryosphere is needed to meaningfully predict the behaviour of the glaciers. The focus is set on the Khumbu glacier, where several datasets have been collected (see Chapter 4).

First, the higher resolution topography allowed for including a distributed radiation component in the snow and clean-ice melt model (Paragraph 3.2.1). Further, ice melt under debris cover is separately simulated, as shown in Paragraph 3.2.2. Glacier dynamics such as basal sliding and avalanches mass transport are illustrated in Paragraph 3.2.3. Finally, a simplified approach for differential flow routing through the different components of the system (soil, ice, snow) is applied (Paragraph 3.2.4).

3.2.1 Snow and clean ice melt

The smaller catchment is modelled at a ten-fold finer spatial resolution, thus local effect of topography can be included in the melt module in order to provide a more physically-based representation. The use of temperature index models over large basins and more data-intensive physically-based melt models is recommended (Brubaker et al. 1996) to provide realistic, processed based evaluations of runoff. Here, solar radiation is spatially distributed in each cell depending on sun position at each time step, and then corrected for topographic shadowing effects. The hybrid melt model (Pellicciotti et al. 2005) is:

$$M_{snow} = \begin{cases} DDF_{snow}(T - T_0) + RF_{snow}\ G\ (1 - \alpha) & \text{if} \quad T > T_t \\ 0 & \text{if} \quad T \leq T_t \end{cases} \tag{3.16}$$

$$M_{cleanice} = \begin{cases} DDF_{ice}(T - T_0) + RF_{ice}\ G\ (1 - \alpha) & \text{if} \quad T > T_t \\ 0 & \text{if} \quad T \leq T_t \end{cases} \tag{3.17}$$

where DDF and RF are calibration parameters (degree day and radiation factor respectively), G the distributed global radiation $[W/m^2]$, α the albedo, T the air mean daily temperature, T_t the threshold air temperature for melting. T_t is assumed to be $-5°C$ (Paragraph 5.2.1). The coefficients DDF and RF are differentiated for snow and clean ice, and have been separately calibrated as shown in Chapter 5.

This melt model is similar to the hybrid model implemented for the wider catchment (eq. (3.8)). However, here solar radiation is calculated for each cell, which was formerly impossible due to the coarse topographical resolution and the scarcity of observed data. First, the theoretical incoming solar radiation is computed for each cell in each day of the year, based on latitude, date and the digital elevation model. Afterwards, the theoretical radiation is rescaled with the observed daily global radiation at Kala Patthar (5600m a.s.l.), in order to account for the meteorological conditions at each day of the simulation. This is achieved by using a *clearness index* coefficient, defined as ratio of observed and theoretical global radiation during each day of the simulation. Figure 3.2 compares the theoretical and observed daily radiation. The lower radiation pattern in the second half of year is due to the extensive cloud cover during the monsoonal season.

Albedo is defined based on the land cover (bare soil, ice, snow, debris covered ice) update at each simulation step. Albedo values are retrieved from literature, being 0.2 for soil, 0.4 for ice, 0.7 for snow, 0.3 for debris covered ice if the debris thickness is below the critical value (see Paragraph 4.5.2), 0.2 otherwise.

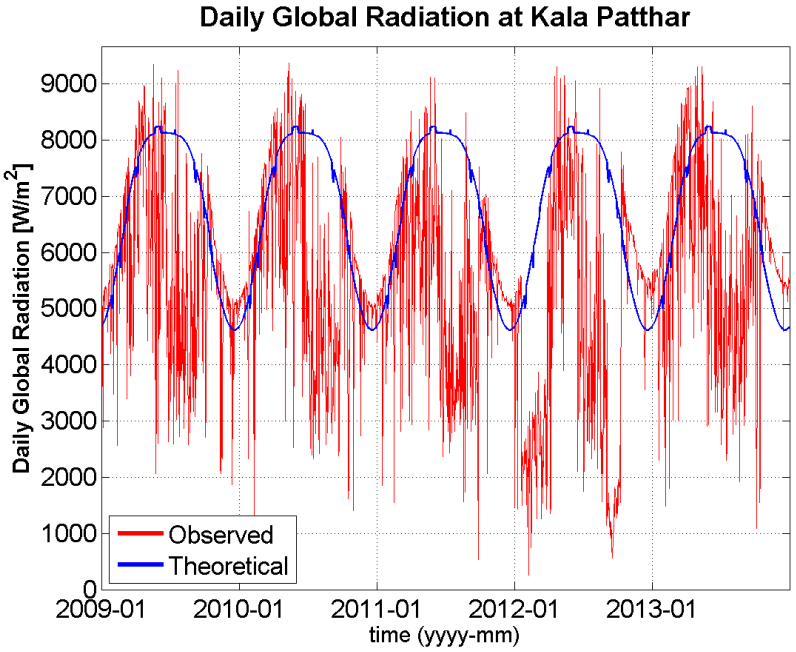

Figure 3.2: Comparison between theoretical and observed daily global radiation at Kala Patthar (5600 m a.s.l.) in the available period, from 2009 to 2013.

3.2.2 Ice melt under debris cover

As anticipated in Paragraph 3.1.1.1, ice ablation is treated separately whether occurring under debris covered ice or for clean ice. Indeed, debris material has lower albedo than ice or snow, thus adsorbs more shortwave radiation and higher ice ablation is expected. However, as the debris layer exceeds a critical thickness, its thermal resistance prevents heat propagation, thereby hindering ice ablation. Hence, thin debris layers increases ablation compared to clean ice, whereas thick layers lowers it. The thickness at which the ablation rate is the same as that of clean ice is named *critical thickness*.

Paragraph 4.5 explains how debris cover is mapped over the study area, assigned thickness values and related to ice ablation. Here, it is illustrated how surface temperatures and debris thicknesses are used to predict mean daily ice ablation in the debris covered portion of the glacier.

A distributed surface energy−balance modelling approach is used after Mihalcea et al. (2008), driven by meteorological variables observed from ground stations and debris

thicknesses distribution from remote sensing (see Paragraph 4.5). The debris module is run only on the catchment closed at Periche, thus with a spatial resolution of 300 m.

Buried−ice melt strongly depends on debris's thermal resistance and surface temperatures over the glacier. In order to predict surface temperatures, Mihalcea et al. (2008) found a correlation with global radiation and debris thickness. Indeed, thicker debris display lower albedo and lower influence from underlying ice, thereby increasing the surface temperature. However, it is reasonable to assume that also meteorological conditions do alter debris surface temperature; thus, the global radiation is considered while estimating surface temperatures. The best estimated regression is given in eq. (3.18):

$$Ts_x = 0.0031\ G_x + 15\ DT_x \tag{3.18}$$

where Ts_x [K] is the daily surface temperature for cell x, G_x and DT_x respectively the daily global radiation [W/m^2] and the debris thickness [m] at the same location. G_x is calculated with eq. (3.19). DT is retrieved from remote sensing and ground observations (Paragraph 4.5.2). Lacking surface temperature measurements, those estimated from Landsat (Paragraph 4.5.1) are used to calibrate the parameters in eq. (3.18). Parameters are found so that the error between the predictions and Landsat data has null mean and is as evenly distributed over the glacier as possible. The best fitting equation (3.18) yields a R^2 of 0.2, a mean error of 0.87 K (underestimate with respect to Landsat temperatures), maximum and minimum errors of +60 K and -10 K, respectively. Maximum errors are observed in few cells where the debris is thicker, typically on lateral moraines, and might derive from the uncertainties affecting great debris thickness values, extrapolated by means of an exponential functional; these cells also lower the R^2 coefficient value. Compared to the Landsat scene, surface predicted temperatures are slightly overestimated in the upper part of the glacier (above the Everest Base Camp), overestimated on the moraines and slightly underestimated on the glacier tongue.

Daily mean global radiation is distributed over the study area according to Oerlemans (2001):

$$G_x = G_{ref}\ (1 + 2.4{\times}10^{-5}\ \ (h_x - h_{ref})) \tag{3.19}$$

where G_{ref} is the observed daily global radiation at the reference station, here Kala Patthar due to the proximity to the glacier and the completeness of the record, h_x the elevation at cell x and h_{ref} that of the reference AWS. Radiation could be also distributed by means of the topography−based model used in Paragraph 3.2.1. Indeed, the two methods yield similar results; here, Oerlemans (2001) is preferred as its use is better documented in literature for predicting ice melt beneath the debris cover (Mihalcea et al. 2008).

Afterwards, the effective thermal resistance over the debris covered area is estimated from a relation found by least−squares analysis by Mihalcea et al. (2008). Thermal resistance is defined as the ratio of debris thickness and thermal conductivity (Zhang et al. 2011). However, it is very difficult and time−consuming to estimate or measure the thermal resistance directly in the field (Nakawo & Rana 1999). Therefore, lacking field data in this study, it is accepted the correlation found by Mihalcea et al. (2008) for the debris cover of Baltoro glacier, in the upper Indus basin:

$$R_x = 19.841\ DT_x + 1.0262 \tag{3.20}$$

where R_x is the effective thermal resistance $[m^2\ °C/W]$ and DT_x the debris thickness, both for the generic cell of location x.

Finally, the mean daily ablation under debris cover for each cell (M_x) is calculated as:

$$M_x = \left(\frac{Ts_x}{R_x}\right)\ \left(\frac{1}{L_f\ \rho_l}\right)\ 8.64 \times 10^4 \tag{3.21}$$

where L_f is the latent heat of phase change of ice ($334{\times}10^3\,\mathrm{kg}^{-1}$), ρ_l the density of ice ($900kg/m^3$) and the constant the number of seconds per day.

3.2.3 Glacier dynamics

Glacier flow is driven by gravitational forces, i.e. the ice mass weight acting on a sloped plane. Here, only the sliding of ice over the bed is taken into account, neglecting the deformation of the bed by assuming it to be hard. Glacier motion is further assumed to be at the base of the ice sheet, thereby disregarding plastic deformation of the ice. A simple approach is chosen as understanding basal slip remains a major problem in glacier physics (Cuffey & Paterson 2010, p. 236).

The driving stress of glacier sliding is computed from the estimated ice thickness at each cell (see Paragrph 4.6) for each time step:

$$\tau_b(x, y, t) = \rho_{ice}\ g\ h_{ice}(x, y, t)\ sin(\alpha) \tag{3.22}$$

where τ_b is the basal shear stress [Pa], $\rho_{ice} = 917\ kg/m^3$ the ice density, g the gravitational attraction (9.81 m/s^2), h_{ice} the ice thickness [m] and α $[rad]$ the local slope, derived from the 300 m DEM. The slope values are previously filtered in order to reduce abrupt variation on small distances. In this formulation, the driving stress is balanced by the sole base drag, whereas actually lateral moraines drag, confinement from surrounding ice, creep deformation and ice compression and elongation generate forces that

restrain glacier flow. Therefore, basal drag is overestimated, which may result in higher ice velocities than would derive from physically based analyses. This is corrected by assuming a maximum shear stress that can be developed at the slip surface; calculations of basal shear stress suggest that in valley glaciers the value of 200 kPa is reasonably not exceeded (Cuffey & Paterson 2010).

From the calculated basal driving stress, glacier velocities are computed by means of Weertman's formula (Weertman 1957), which accounts also for the frictional effects of asperities on the sliding bed, i.e. glacier bottom motion is modelled as a combination of regelation and basal creep; this formulation does not consider internal creep or deformation:

$$u_{ice}(x,y,t) = \begin{cases} \left(\frac{\tau_b(x,y,t)-\tau_{eq}}{\nu^2\ R}\right)^{\frac{n+1}{2}} & \text{if} \quad \tau_b(x,y,t) > \overline{\tau_{eq}} \\ 0 & \text{if} \quad \tau_b(x,y,t) \leq \overline{\tau_{eq}} \end{cases} \tag{3.23}$$

where u_{ice} is the ice velocity, non negative when the local driving stress outweighs the equilibrium stress τ_{eq}, set to 80 kPa according to (Immerzeel et al. 2013), n is the creep constant of Glen's flow law (3 in most cases) (Weertman 1957); ν [−] and R [Pa s$^{1/3}$], respectively roughness of the bedrock and material roughness coefficient, are calibration parameters. A superior limit to velocity is set to 250 m/y in order to compensate for possible numerical instabilities.

Once the flow velocity is known, the ice height loss is calculated for each cell:

$$\Delta h_{ice}(x,y,t) = \frac{h_{ice}(x,y,t)\ u_{ice}(x,y,t)\ dt}{ice_{\%}(x,y,t)\ l_{cell}} \tag{3.24}$$

where Δh_{ice} is the height loss from the cell, l_{cell} the length of the cells sides, dt the time step and $ice_{\%}$ the cell fraction covered by ice.

The ice loss is then shifted to downstream cells along three directions, weighted depending on the local slope, so that the new ice height is given by

$$h_{ice}(x,y,t+1) = h_{ice}(x,y,t) - \Delta h_{ice}(x,y,t) + h_{3flow}(x,y,t) \tag{3.25}$$

being h_{3flow} the weighted average of the ice loss from upstream cells.

Finally, snow mass transport due to quick gravitational movements, such as avalanches, is also included. This process may be relevant for glacier nourishment especially for valley glaciers surrounded by steep topography, as it is the case in the study area. For each cell, a slope dependent snow holding depth is defined. Once a year, arbitrarily April 1st, if the snow depth of a cell exceeds the cells' snow holding depth, snow is redistributed to the next lower cell in the flow direction. This approach has been used in literature

e.g. by Immerzeel et al. (2014). Debris avalanches are not simulated, thereby assuming a constant debris thickness over the simulation period.

3.2.4 Glacial Hydrology

The catchment closed at Periche is mainly constituted of glaciated area (85 km^2, amounting to 56% of the total area). Therefore, it is necessary to model the different hydrological processes occurring within and around the ice body, which are likely to dominate the hydrological behaviour of the basin. In a high altitude, glacierised catchment water can flow through three means, i.e. ice, snow and soil. In particular, water may infiltrate ice and snow, move through fractures and pipes within the ice body, flow over the glacier surface and at the glacier bed, in addition to the previously described (Paragraph 3.1) surface runoff and ground infiltration regarding the soil. Usually, ice is considered impervious to infiltration, since the discharge through major fractures far outweighs that within the ice porous matrix.

In this study, a simplified approach is implemented, representing the catchment as a series of parallel ice, snow and soil reservoirs, each subdivided in fast and slow reservoirs. Fast reservoirs account for surface and endoglacial-pipes runoffs, whereas slow reservoirs model water storage within soil, snow and ice cavities. Interactions between the three means are neglected, as well as those with the basal sliding and glacier motion. Thus, each means is represented by means of a linear cascade of reservoirs (Nash route flow) as explained in Paragraph 3.1.4, having a different lagtime for fast flow and one for the slow flow. For soil, runoff and infiltration are separated according to eq. (3.15); however, for snow and ice two empirical parameters are introduced to divide the fast and slow flows. This approach entails eight parameters, that will be calibrated from different parts of the hydrograph as illustrated in Chapter 5.

Chapter 4

Data and Methods

This chapter describes the data acquired to run and calibrate to model, and the methods applied to these data. The model is run with a daily time step on both the wider and smaller catchment. Necessary inputs for the hydrological model are temperature, rainfall and snowfall, presented in Paragraphs 4.1, 4.2 and 4.3 respectively. Ice ablation rates, debris thicknesses and ice thicknesses, surface temperatures are inputs to the glaciological modules (Paragraphs 4.5 and 4.6).

A number of automatic weather stations (hereafter AWS) is located in the study area, measuring the main meteorological variables. However, the roughness of the topography determines a high spatial variability of these quantities, and at the same time the amount of stations in the catchment is limited by the harsh climate and accessibility. Therefore, ground data are integrated with information from remote sensing, which provides the spatial distribution of data, but on the other hand requires to be substantiated with ground observations.

Compared to the previous thesis (Paramithiotti 2013), this study presents important innovations. First of all, new types of data have been collected in a field survey on Khumbu glacier in 2014, providing relevant knowledge about the cryosphere and thus allowing for a more complete modelling approach. These measurements include ice ablation rates, ice flow velocities, debris cover thickness and fresh and old snow densities. Moreover, the acquisition of the hydrometric level time series in a river section farther north than the already available one made possible focus on modelling the glaciological components in a smaller catchment. Secondly, the AWS time series is extended of two years, which means for some stations that the observation period has doubled. Finally, new methods for merging ground− and remote sensing data are implemented. In particular, the use of long term averages of satellite data rather than hourly or 8−days

time resolutions opens the possibility for more flexible uses of the model, not requiring the costly update of remotely sensed inputs.

4.1 Temperature

Mean daily temperature plays a fundamental role in driving the model, as it partitions solid and liquid precipitation and governs snow and ice melting. Fairly extended time series are available from six stations, mostly located in the upper part of the catchment; these are integrated with MODIS monthly averages for distributing the temperature over the basin. A gap-filling procedure preserving monthly averages is implemented over the ground data, so that the model can be run continuously. Finally, a correction is applied to temperatures at high altitude so that it is possible to model melting processes occurring when the daily mean temperature is below the freezing level but the daily maximum exceeds it.

4.1.1 Ground stations data

Temperature data are retrieved from the stations listed in Table 4.1. Apart from Okhaldunga, which belongs to the Nepalese Department of Hydrology and Meteorology (DHM), the stations are part of the SHARE (Stations at High Altitude for Research on the Environment) network, installed and managed by EvK2-CNR. Okhaldunga station does not lie within the watershed; however, given its geographical proximity and the absence of other ground observations in the lower part of the catchment, it has been included.

Table 4.1: Temperature stations network

StationID	Elevation [m a.s.l.]	Period	Frequency	Network
Okhaldunga	1720	1996-2013	daily	DHM
Lukla	2660	2003-2013	hourly	EvK2-CNR
Namche	3570	2003-2013	hourly	EvK2-CNR
Periche	4260	2003-2013	hourly	EvK2-CNR
Pyramid	5035	2003-2013	hourly	EvK2-CNR
Kala Patthar	5600	2009-2013	10 minutes	EvK2-CNR

Each time series has been reduced to the daily temporal resolution; the model is indeed fed with daily minima, maxima and averages. Data quality control is operated by EvK2-CNR.

4.1.1.1 Data issues and Gap filling

High altitude stations work in extreme climatic conditions, and therefore observations present relevant gaps. Each measurement is provided with its quality indication, being good, dubious, bad or missing. In this study, only good data are taken into account; hence, no-data periods up to six month long are found in the datasets. The low amount of stations and the fact that often multiple stations are simultaneously out of order prevents from adopting spatial statistics for reconstructing the missing data. Therefore, it is necessary to implement a method based on each single station's data.

First, a linear interpolation over the missing data period was tried. Whereas it provided acceptable results for few days long time spans, it proved to be insufficient to re-create extended gaps. Subsequently, a simple but effective technique has been made up. It consists in substituting the missing daily temperatures with the mean value of the specific days over the whole period of observation; this procedure is applied to daily minima, maxima and averages. Figure 4.1 illustrate the outcomes for the mean daily values in the stations with the higher amount of data replaced.

The main limit of this approach is that, when the same days are missing from different years, it creates a time series with same temperature values on same dates. However, as can be seen in Figure 4.1, seasonal variations are reproduced. The gap filled series is deemed to be a better option than running the model on monthly averages, as it has been done in the previous thesis. Such a procedure is necessary in order to run the model in a continuous and consistent way, as the presence of missing data would impede the spatial distribution of the variables.

4.1.2 Remote sensing data

The satellite sensor from which distributed surface temperatures are retrieved is the Moderate Resolution Imaging Spectroradiometer (MODIS)[1]. In particular, the MOD11C3 product has been used, which provides monthly averaged land surface temperature at $0.05°$ latitude/longitude grids (ca. $5.5km$ at $28°$ latitude). These data have been acquired over the same period as the ground station data, i.e. from 2003 to 2013. The dataset is first compared with the monthly averages observed at the stations (Figure 4.2).

From Figure 4.2 it is clear that MODIS data fail to represent the actual temperatures from June to September, both in daily and nightly records. This is due to the fact that

[1]MODIS product is courtesy of the online Data Pool at the NASA Land Processes Distributed Active Archive Center (LP DAAC), USGS/Earth Resources Observation and Science (EROS) Center, Sioux Falls, South Dakota (https://lpdaac.usgs.gov/ [Accessed 1st November 2014]).

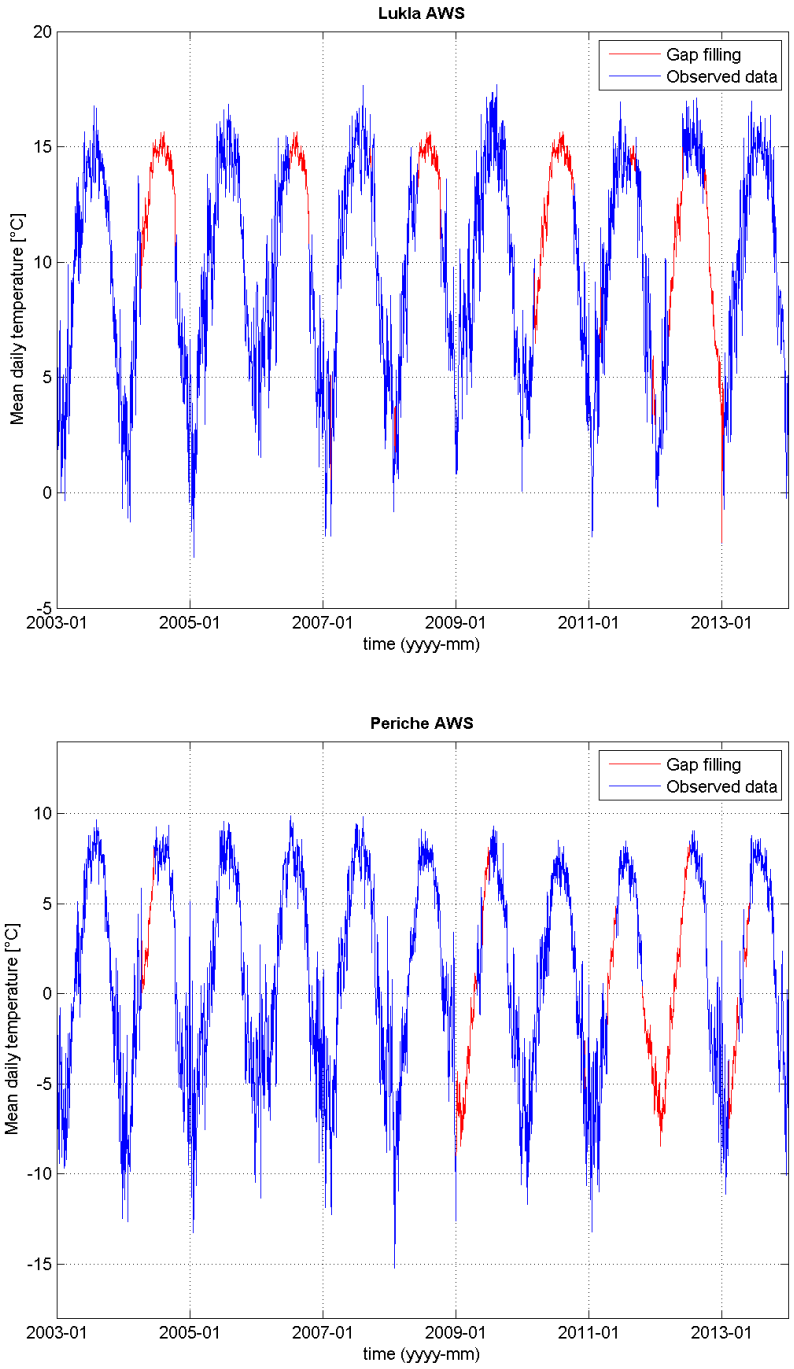

Figure 4.1: Temperature mean daily values observed at stations (blue) and after gap-filling (red). Only the stations with the greatest amount of reconstructed data are shown.

during these months, corresponding to the monsoon, the basin is frequently covered with clouds which prevent the sensors from measuring land surface temperature. This is confirmed by the Quality Control flag associated to each pixel of each MODIS scene; indeed, data quality during the monsoon is reported as bad, for both daily and night

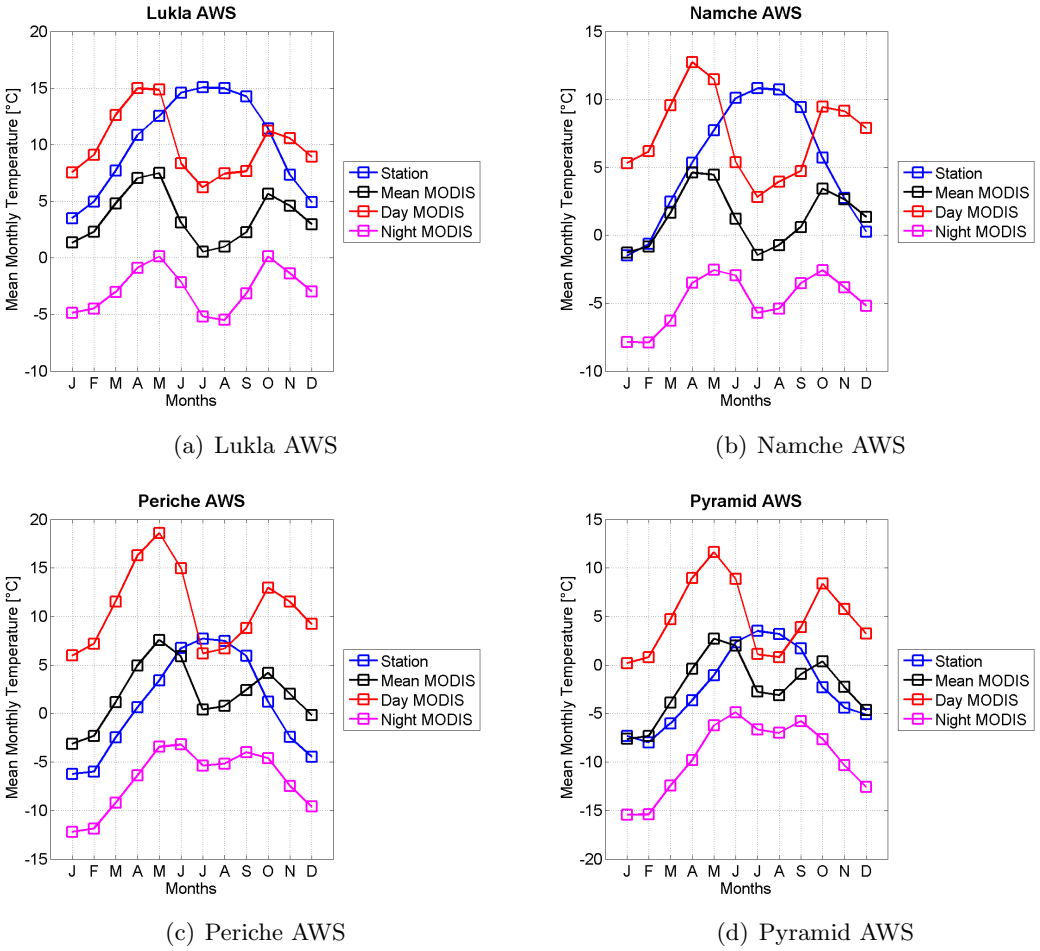

(a) Lukla AWS

(b) Namche AWS

(c) Periche AWS

(d) Pyramid AWS

Figure 4.2: Comparison of monthly means (2003-2013) from ground stations and MODIS temperatures at the station location.

measurements. Wan et al. (2004) advice that land surface temperature may be retrieved from MODIS TIR data only in clear-sky conditions so that it is not mixed with cloud-top temperature. Because TIR signals cannot penetrate clouds, cloudy pixels must be skipped in the land surface temperature processing. Therefore, the period from June to September has been excluded from the lapser ate estimates.

This issue could be overcome by using a higher time resolution for the satellite data, such as the 8−days product MOD11C2, in order to remove the scenes with a relevant cloud cover, which determines the overall bad quality in the monthly mean product. However, such a choice would determine a four−fold rise in the computational cost associated with the retrieval and elaboration of the data. Moreover, it would require a continuous acquisition of new data as the model is run over new periods, making it slower and less appropriate for possible real−time applications.

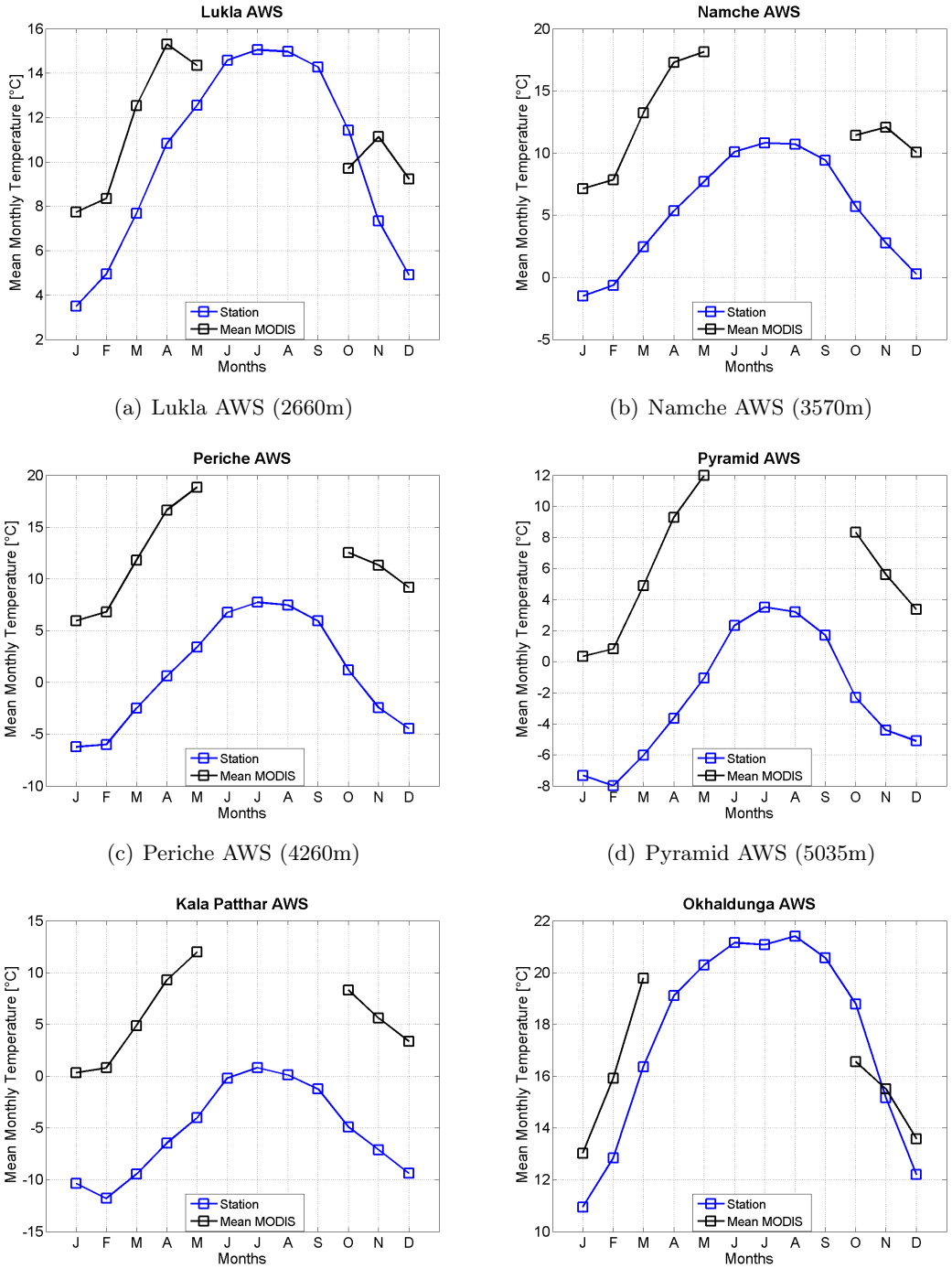

(a) Lukla AWS (2660m)

(b) Namche AWS (3570m)

(c) Periche AWS (4260m)

(d) Pyramid AWS (5035m)

(e) Kala Patthar AWS (5600m)

(f) Okhaldunga AWS (1720m)

Figure 4.3: Comparison of monthly means (2003-2013) of ground stations and MODIS temperatures at the station location after the removal of data affected by cloud cover.

Figure 4.3 compares the ground− and remote sensing datasets after the removal of the measurements affected by cloud covers. As can be seen in Figure 4.2, the mean of MODIS day and night observations seem to better reproduce the ground data, and thus

it will be used in the following analysis. It is also evident that the absolute values of MODIS temperatures cannot be trusted but need to be re-adjusted to the ground ones. Indeed, satellite temperatures tend to be higher than the observed ones, especially at high altitudes, as also Paramithiotti (2013) had observed.

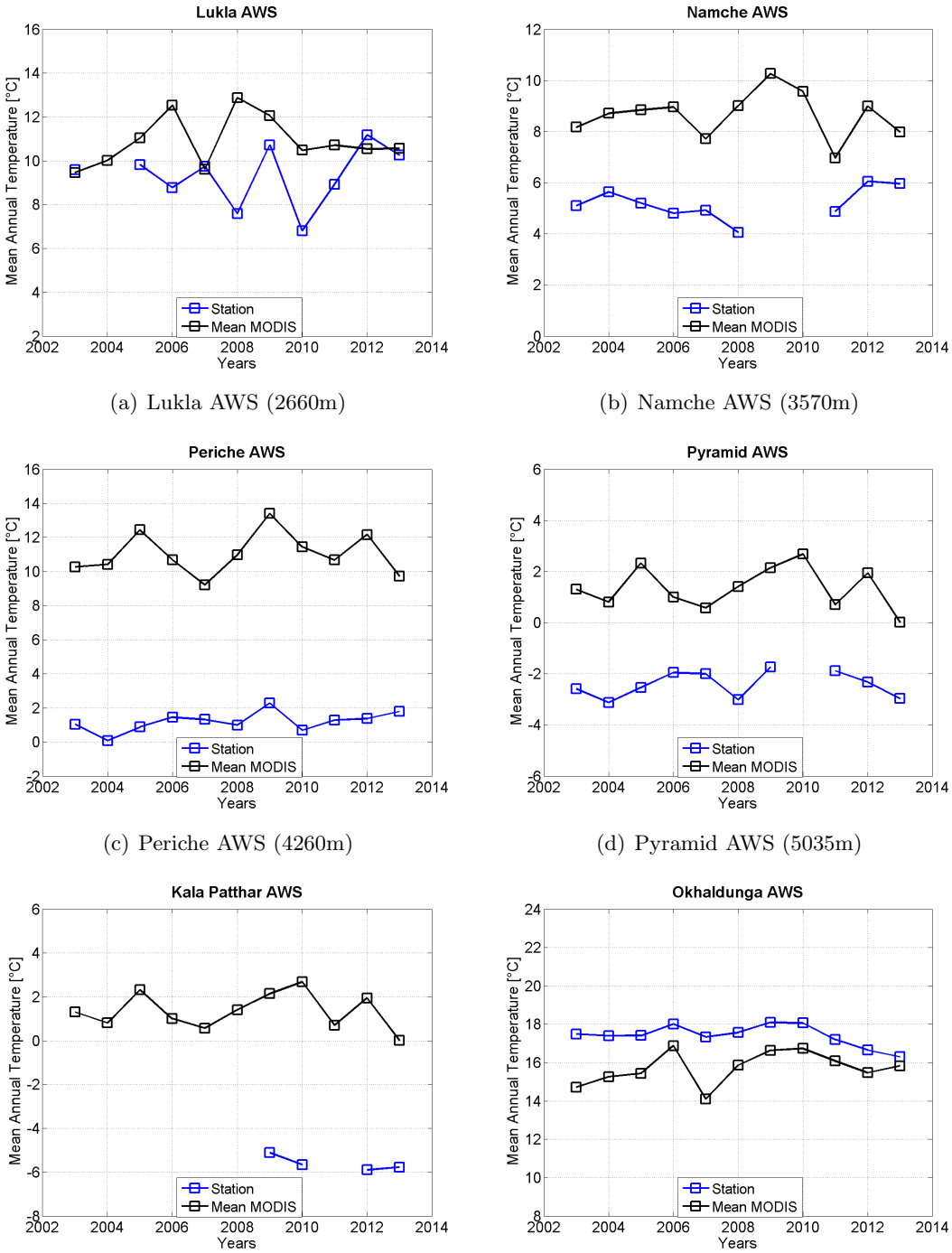

(a) Lukla AWS (2660m)

(b) Namche AWS (3570m)

(c) Periche AWS (4260m)

(d) Pyramid AWS (5035m)

(e) Kala Patthar AWS (5600m)

(f) Okhaldunga AWS (1720m)

Figure 4.4: Comparison of annual means of ground stations and MODIS scenes at the station location, after the removal of data affected by cloud cover.

The inter-annual variability of the ground stations and remote sensing series is also checked (Figure 4.4). The variations of mean annual MODIS temperatures display fairly similar oscillations as the ground data, whereas as expected absolute values need to be adjusted. Some deviations are anyway expected, as MODIS data are averages over the $5km\ x\ 5km$ pixel, while ground stations provide point measurements. Figure 4.4 suggests that, in order to be adjusted to the ground values, MODIS data can be shifted, while rescaling is not necessary.

4.1.3 Data merging

Two different methods are alternatively implemented in order to distribute the temperature observations over the study area. First, a linear gradient based on altitude is estimated from ground data and remote sensing temperatures. This method provides a good fit for the observations but neglects temperature patterns other than that associated with altitude. Thus, MODIS scenes are merged with ground observations so that the spatial distribution of temperatures is fully represented. Both the methods are used to create the input grids for the model, and model results for both datasets are compared in Chapter 5.

4.1.3.1 Lapse rate estimation

Initially, a linear gradient is estimated from monthly means for both ground and satellite data. With respect to the previous study in the basin, it was possible to include also the highest station in the basin (Kala Patthar, 5600m a.s.l.) as a longer (5 years) time series has become available. Whereas ground observations returned good correlation coefficients with altitude, the aforementioned low quality of satellite temperatures did not allow for good interpolations on a monthly basis and thus could not be compared with the ground stations. Therefore, a different approach has been carried out. Only those months which are not affected by cloud cover (October to May) are considered in the analysis, for both the stations' and the satellite observations. Linear gradients with altitude are then estimated, as shown in Figure 4.5. The lapse rate is evaluated using all the available stations, each used as refernce station within an influence area defined by means of Thiessen polygons.

Both ground and satellite data have high correlations in terms of R^2 coefficient, even though that is higher for ground observations. This is likely due to the fact that satellite temperatures have a coarse spatial resolution, being the averaged values over an area of $5km\ x\ 5km$. Therefore, only the stations lapse rate ($-5.7°C$ per km) will be used to predict temperature for each pixel location as input to the model. This value is in

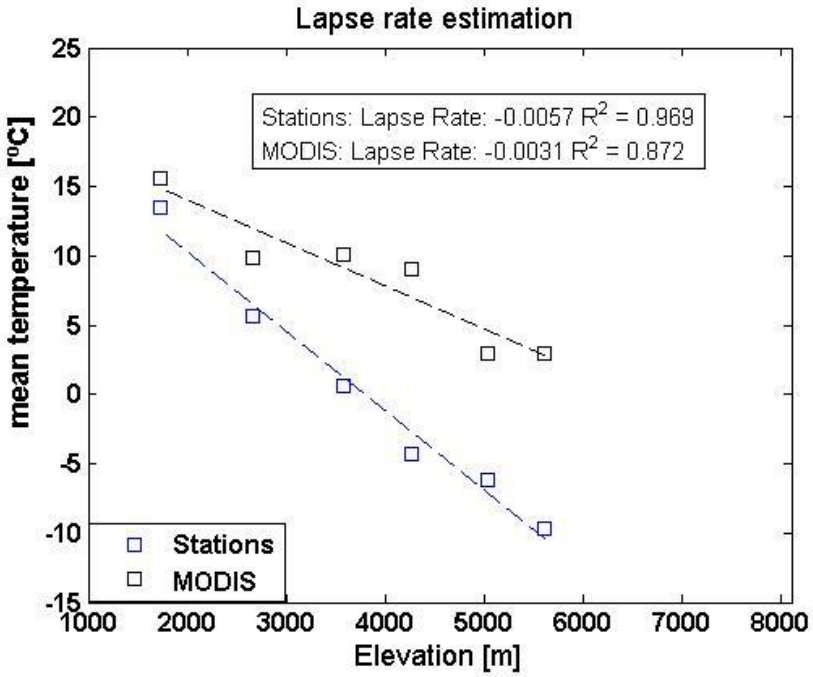

Figure 4.5: Lapse rate estimates for temperature annual means. Months form June to September are not included in the computation of annual means due to the low reliability determined by cloud cover.

accordance with the lapse rate of $-6.3°C$/km found by Immerzeel et al. (2012) for the Langtang River basin, 150 km west to the study area, and with those used by Nepal et al. (2014) for the Dudh Kosi basin, being $-5.5°C$/km for summer and $-6°C$/km for winter. Kattel et al. (2013) estimated a lapse rate of $-5.4°C$/km for the southern slopes of central Himalayas.

4.1.3.2 Spatial distribution

The advantage of using satellite data is that they do carry information on the spatial distribution of the variables. Indeed, on a very complex topography, climatic variables are expected to vary not only based on altitude, but also according to the effect of local terrain on the atmospheric circulation, which are difficult to model (Kattel et al. 2013). The adopted merging approach consists in re−adjusting MODIS scenes so that at each station's location they do match the observed data; the procedure is explained as follows. Initially, the MODIS grids are rescaled to the same spatial resolution as that used in the model, i.e. $3km\ x\ 3km$. For each month, the mean value in each pixel is calculated by averaging the monthly grids over the period $2003 - 2013$; in this way the inter-annual variability will not affect the outcomes. The ground stations are assigned an influence area in the basin by means of Thiessen polygons. At each time step of the simulation, the difference between the MODIS mean temperature at the reference station and the

daily ground observation is calculated (eq. (4.1)). This difference is then used to shift the MODIS values of all the cells within the Thiessen polygon in order to provide daily temperature estimates at each cell (eq. (4.2)).

$$\Delta = \bar{T}_{ref}^{MODIS} - T_{ref}^{station} \tag{4.1}$$

$$T_{cell} = \bar{T}_{cell}^{MODIS} - \Delta \tag{4.2}$$

where $\bar{T}_{ref}^{MODIS}$ is the monthly mean temperature from MODIS at a ground station location, $T_{ref}^{station}$ the daily observation from the same station, $\bar{T}_{cell}^{MODIS}$ the monthly mean temperature from MODIS at the generic cell location within the Thiessen polygon of the reference station and T_{cell} the predicted daily temperature for that generic cell.

This bias−adjustment method is one of the simplest available for satellite and ground data merging. It could be argued that more sophisticated methods for spatial predictions of climatic variables, such as kriging, may provide more accurate results. However, it has been shown that on complex topography, fitting a robust variogram is challenging, especially when the station network is sparse, thus simpler methods are preferable (Dinku et al. 2014).

4.1.4 Temperature correction at high altitude

At high altitude, it is not infrequent to see periods with day-time melting and night-time freezing of the snow and ice cover, so that melted volume is generated even though the mean daily temperature lies below the freezing level. In this conditions, the daily time step used in the simulation would lead to underestimating the snow and ice melt. A correction to the input temperature grids, obtained with one of the aforementioned methods, is thus applied following Wulf et al. (2011):

$$T = \begin{cases} T_{max}\ 0.5 \left(\frac{T_{max}}{T_{max}-T_{min}}\right)^{0.2} & \text{if} \quad T_{dailymean} < T_t \\ T_{dailymean} & \text{if} \quad T_{dailymean} > T_t \end{cases} \tag{4.3}$$

where T_t is the freezing temperature as described in Paragraph 5.2.1. The corrected temperature at the station locations are shown in Figure 4.6.

As emerges from Figure 4.6, the corrected temperatures at Pyramid and Kala Patthar remain below the freezing level, while at Periche the correction raises the temperatures above the freezing point. Thus, by means of this formula it is possible to model the daily snow and ice melt during night-freezing periods at intermediate altitudes (3000 to 5000m).

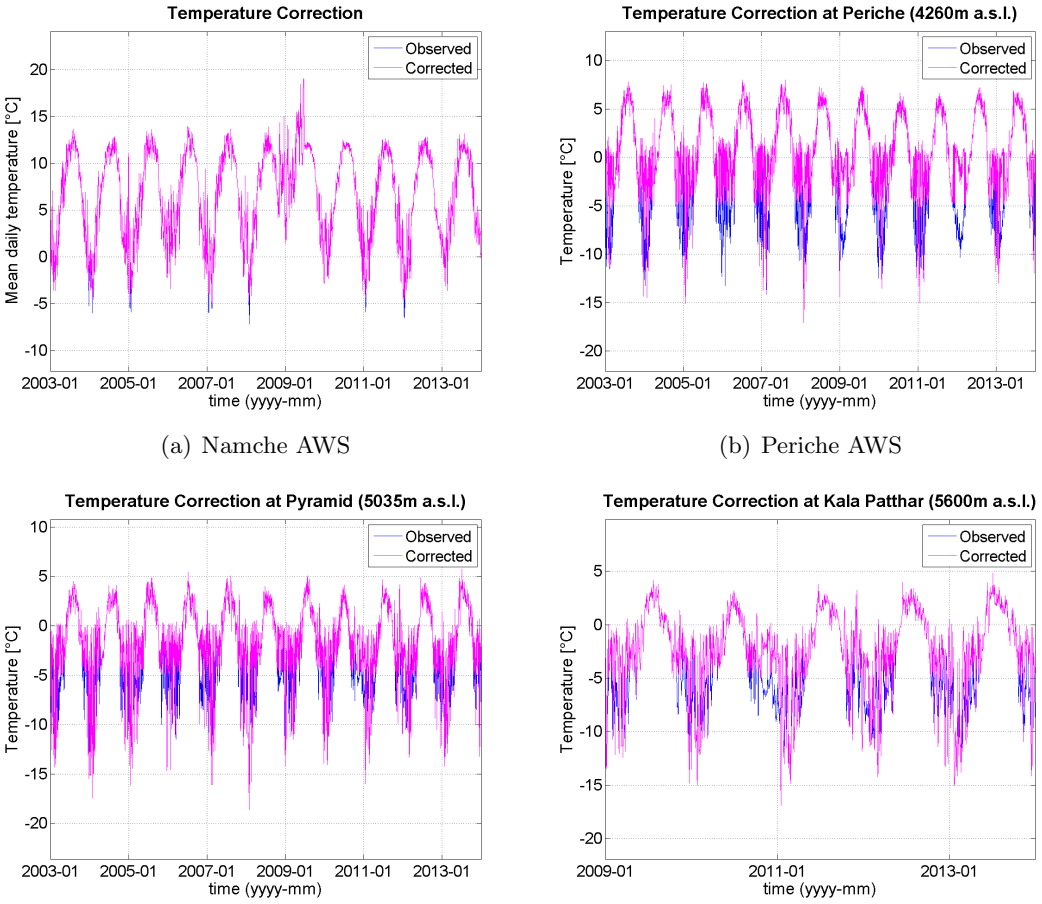

(a) Namche AWS

(b) Periche AWS

(c) Pyramid AWS

(d) Kala Patthar AWS

Figure 4.6: Original (blue) and corrected (magenta) mean daily temperature time series from the high altitude stations.

4.1.5 Temperature distribution in the double scale modelling approach

In the hydrological simulations over the catchment closed at Rabuwa Bazar, both the lapse rates and the MODIS bias adjustment techniques are implemented to generate the temperature input grids, so that the influence on model performance can be analysed. At the smaller catchment scale, however, the spatial resolution of MODIS grids is deemed too rough to accurately describe temperature spatial variability. Therefore, the lapse rate approach is used, which on the other hand showed better efficiency at high altitudes.

4.2 Rainfall

Precipitation data are of paramount importance as inputs to the model, as they dominate the mass balance of the system. Given the complex topography of the Dudh Kosi catchment, it is extremely challenging to simulate the spatial patterns of precipitation, as they are deeply influenced by smallscale ridgevalley gradients as well as from largescale orographic effects and circulation. Several studies have been carried out in order to establish a relation between precipitation and its control variables in the Himalayas, mainly topographical quantities (e.g. see Bookhagen & Burbank (2010, 2006), Barros et al. (2000)). However, precipitation patterns in the Himalayas vary considerably over small spatial scales (Anders et al. 2006).

The study area is equipped with several rain gauges, both at low and high altitude; however, the network density is still poor, especially at the higher altitudes. In this study, the input precipitation grids are constructed after ground station data and satellite data. Paragraphs 4.2.1 and 4.2.2 describe these datasets and the procedures for their elaboration. Subsequently, Paragraph 4.2.3 illustrates the methods for merging and distributing the data over the study area.

4.2.1 Ground stations data

Rainfall time series are acquired from both the Nepalese Department of Hydrology and Meteorology (DHM) and the EvK2 networks, just as temperature data. Table 4.2 lists the available datasets. Lower-elevation stations (1720 to 2619m) belong to the Nepalese Department of Hydrology and Meteorology (DHM), whereas the higher-altitude ones (3570 to 5600m) are part of the aforementioned SHARE project, promoted by EvK2-CNR. The SHARE stations have been installed much more recently if compared with those from the DHM; however, nowadays they are provided with ten−years−long time series, which is fairly good for these altitudes.

Table 4.2: Rainfall station network used in this thesis.

StationID	Elevation [m a.s.l.]	Period	Frequency
Okhaldunga	1720	1970-2013	daily
Aisealukhark	1849	1970-2013	daily
Pakarnas	1982	1970-2013	daily
Chaurikhark	2619	1970-2013	daily
Namche	3570	2003-2013	hourly
Periche	4260	2003-2013	hourly
Pyramid	5035	2003-2013	hourly
Kala Patthar	5600	2009-2013	10 minutes

Lukla AWS (2620m), used for temperature data, measures rainfall as well, but due to the bad quality of the data it is substituted with the close DHM station Chaurikhark. Each time series has been reduced to the daily temporal resolution; the model is indeed fed with daily cumulated rainfalls.

4.2.1.1 Data issues and Gap filling

Rainfall data are affected by the same issues described in Paragraph 4.1.1.1. DHM time series were not acquired along with an indication on their quality ans thus are assumed to be validated. EvK2 stations on the contrary, being at higher altitude, operate in very challenging climatic condition, thus returning several bad and dubious data, which are discarded from the analysis, in addition to the missing ones. The relevant extent of the No−Data series requires to implement a gap filling procedure in order to run the model over consecutive periods. As explained in Paragraph 4.1.1.1, the simultaneous lack of data from multiple stations makes it impossible to apply geostatistical methods from neighbouring stations. Therefore, an original simple method is applied.

The criterion is that the cumulated monthly rainfall in incomplete months has to match the mean monthly cumulated rainfall for that month in each station. Then, to each missing day it would be attributed a rainfall amount corresponding to the difference from the monthly mean divided by the number of missing day. However, this approach does not realistically represent the occurrence of separate rain event, which are typically represented as a a temporal Poisson process. Due to the scarcity of data, it is not possible to simulate such an occurrence by stochastic methods. Therefore an alternative solution is implemented. First, it is noticed that Aisealukhark station time series is affected by only minor gaps (1%) over the simulation period (2003 − 2013), which are filled with zero−values. Then, for each station it is evaluated a rainfall−occurrence correlation coefficient by counting the days in which both the generic station and the reference one (Aisealukhark) agree in measuring either rainfall or no rainfall. This coefficient results to be quite high for all the stations (agreement above 75%), suggesting that rainfall occurrence at Aisealukhark can be used as a proxy to re−create rainfall events at other locations. Accordingly, the missing rainfall volume of each month is divided between those days in which rainfall occurs at Aisealukhark. The re-constructed time series are shown in Figure 4.7.

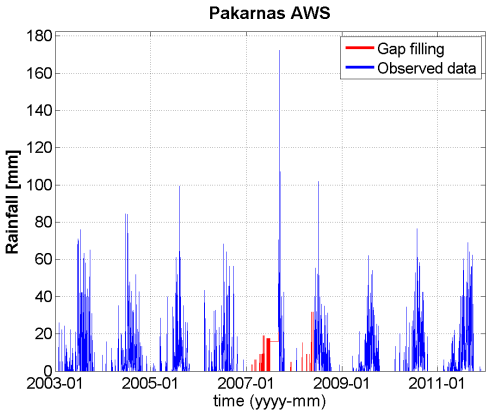

(a) Pakarnas AWS

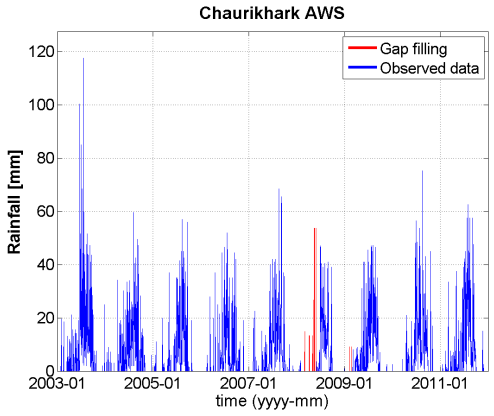

(b) Chaurikhark AWS

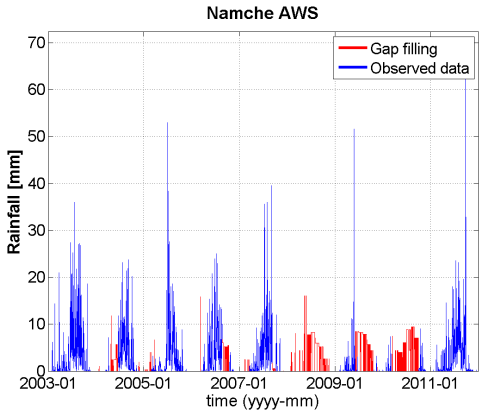

(c) Namche AWS

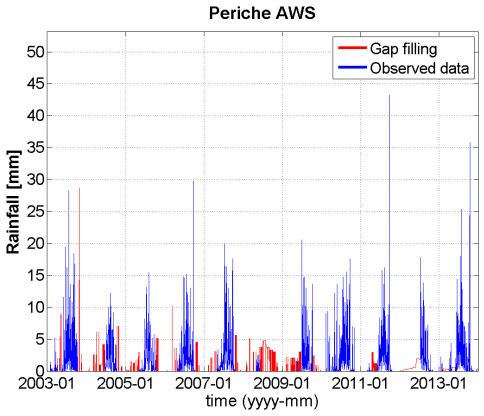

(d) Periche AWS

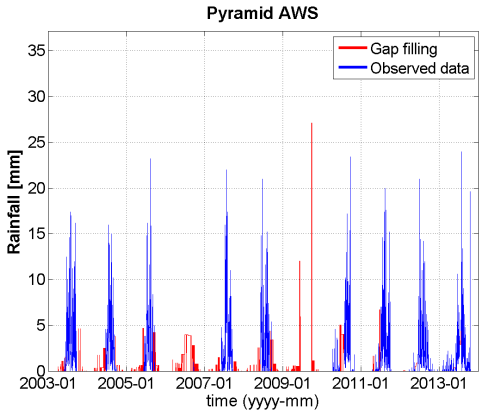

(e) Pyramid AWS

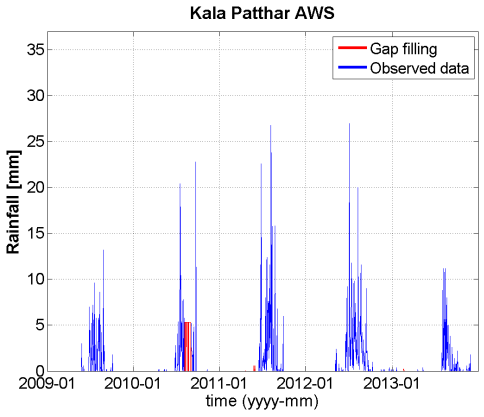

(f) Kala Patthar AWS

Figure 4.7: Rainfall time series (blue) and gap filling (red). Daily cumulated rainfalls from ground station, 2003-2013.

A major limitation of this technique, evident from Figure 4.7, is that extended periods with No−Data values are replaced with constant daily amounts, thereby loosing the temporal variability of rainfall intensities, especially in terms of occurrence of intense events. In particular, the year 2006 will be removed from the simulation as all the three

high altitude stations measured bad−quality data, so that the reconstructed rainfall field over such an extended time and space may be insufficient for creating the input rainfall grids. A similar correlation based approach is used in Wagner et al. (2012), based on annual rather than monthly totals, as best available technique for precipitation gap filling in data scarce region.

4.2.2 Remote sensing data

Satellite estimates of rainfall are retrieved from the Tropical Rainfall Measuring Mission (TRMM), which detects precipitation by means of two instruments on board, i.e. the TRMM microwaver radiometer (TMI) and the precipitation radar (PR). TRMM is a joint mission between NASA and the Japan Aerospace Exploration Agency (JAXA) designed to monitor and study tropical rainfall, launched in 1997 and so far the best product for investigating rainfall patterns in scarcely gauged areas such as high elevations in the Himalayas (Andermann et al. 2011).

As for temperatures, long term TRMM averages are used in this study, not to hinder a future real−time use of the model by requiring the acquisition and processing of satellite scenes. The data product 24B31 is used, a combined Precipitation Radar (PR) / TRMM Microwave Imager (TMI) rain-rate product at 4km (0.25° horizontal and 250m vertical resolution, averaged over 12 years (1998 to 2009)[2], courtesy of Bookhagen (2012).

TRMM scenes are first resampled at the model cell size (3km x 3km) in order to be used in the simulation, and then validated with ground averages from the stations' network on the corresponding period (1998 to 2009 for DHM, 2003 to 2013 for EvK2, lacking earlier data), see Figure 4.8 and Figure 4.9.

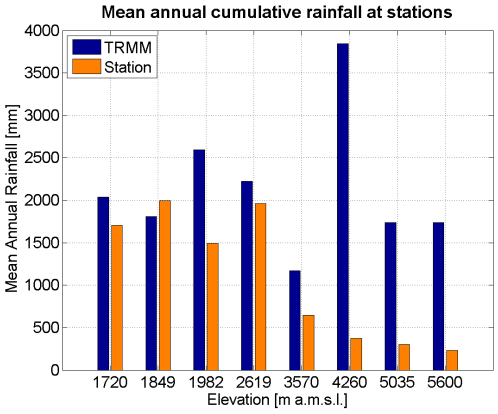

Figure 4.8: TRMM reliability with elevation: mean annual rainfall totals from ground stations and TRMM scenes at each station's location.

[2]Available at http://www.geog.ucsb.edu/ bodo/TRMM/ascii [Accessed 29th October 2014]

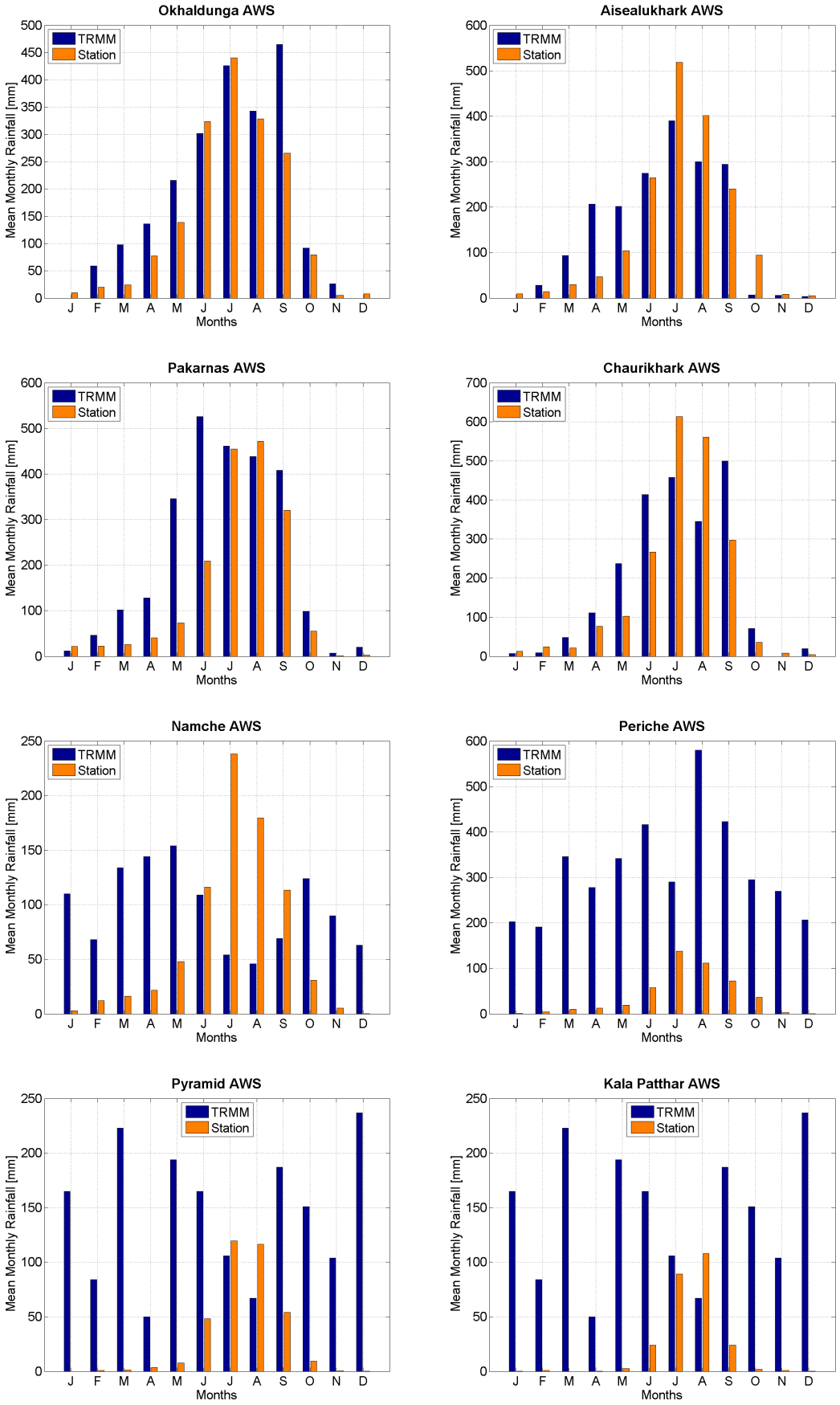

Figure 4.9: Comparison of monthly mean cumulative rainfall from ground stations and TRMM scenes at each station's location.

It is evident from Figures 4.8 and 4.9 that TRMM rainfall totals need to be adjusted to the ground values. Noticeably, at low-altitudes TRMM presents the same seasonal patterns as ground measurements, whereas above 3000m a.m.s.l. it shows huge differences, namely higher precipitation during cold months. This could be due to the fact that, for the microwave sensor, it is hard to separate the scattering and emission signature of the snow in the air from the signature of snow on the ground[3], so that the winter snow cover, relevant at high elevations, affects the rainfall amounts' signal.

4.2.3 Data merging

Different strategies have been developed in order to combine ground measurements, ground truth for absolute values of rainfall totals, and remote sensing data, embedding the spatial distribution of liquid precipitation. First, lapse rates are estimated from ground data, secondly TRMM scenes are merged and scaled with station data.

4.2.3.1 Lapse rate estimation

Rainfall's lapse rates are solely based on ground measurements, as the TRMM signal is not trustworthy at high elevations, as discussed in Paragraph 4.2.2 (see Figures 4.8 and 4.9). Moreover, the variability of elevation within each TRMM pixel is too high to allow for lapse rate computation.

Figure 4.10 illustrates the monthly cumulative means for the ground network. At low altitudes, the rainfall totals increase with elevation, even though they do not appear to vary greatly. Conversely, at high altitude they display a strong negative relation with elevation, with higher stations having lower rainfall totals. At first this could be attributed to the fact that part of the precipitation is solid and thus not measured by the non−heated rain gauges. However, this trend is evident throughout the whole year. The actual explanation lies in the fact that most of the monsoonal precipitation falls on the southern slopes of the Greater Himalayas (Bookhagen & Burbank 2010) before reaching the northern valleys, so that little moisture content is left in the atmosphere at higher elevations after that barrier. This pattern is particularly visible in the TRMM scenes, as shown in Chapter 6.

[3]From http: //trmm.chpc.utah.edu/prainfall.html [Accessed 25th October 2014]

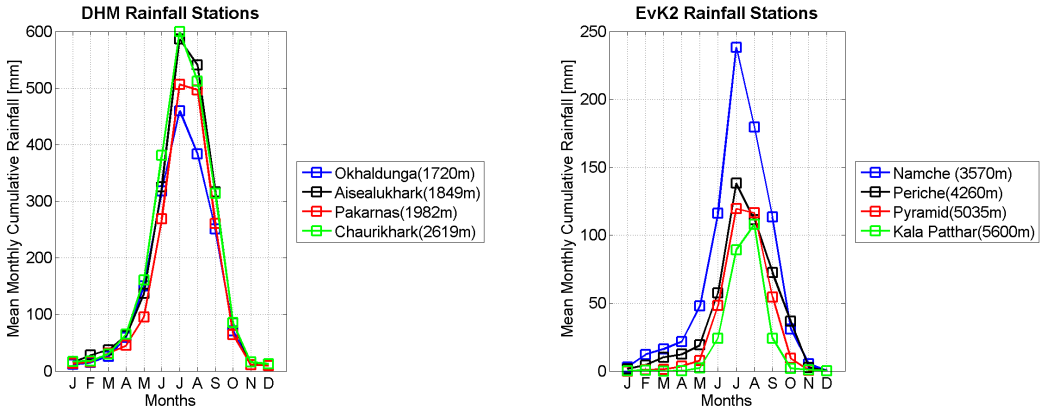

(a) DHM Stations (b) EvK2-CNR Stations

Figure 4.10: Mean Monthly Cumulative Rainfall over the available datasets (1970-2013 for low-altitude stations, left, 2003-2013 for high-altitude stations, right).

Linear gradients relating rainfall and elevation are found, as shown in Figures 4.11 and 4.12. Initially, months have been grouped into seasons based on the pluviometric regime desbribed in Chapter 2 (April to May, June to September, October and November to March), and lapse rates are estimated for each group (Figure 4.11). Secondly, the lapse rate is estimated from the mean annual cumulative rainfall (Figure 4.12). Both DHM and EvK2 stations' data are averaged over the period $2003 - 2013$, so that inter-annual variability and possible climate changes are not affecting the analysis.

As reported in Figure 4.11, low altitude stations display a positive lapse rate, whereas high altitude ones have a negative lapse rate; the same pattern is observed for annual totals (Figure 4.12) and is expected as previously discussed. Similarly, Higuchi et al. (1982) found that precipitation along the main valley of the Dudh Kosi River decreases with altitude in the range from 2800 m to 4500 m a.s.l, while Putkonen (2004) found that in the Annapurna precipitation peaks at about 3000 m altitude and then decreases to the north in the rain shadow of the Himalayan crest.

To build the input rainfall grids, the catchment is divided in Thiessen polygons, and within each polygon the lapse rate is applied with respect to the reference station of the polygon. The annual lapse rate is chosen since the seasonal ones display lower R^2 coefficients, especially for low altitude stations. A possible source of error in this analysis is given by the fact that rainfall measurements neglect the contribution of solid precipitation, hence the high altitude lapse rate might not represent correctly the physical reality. The correction for snowfall amounts, presented in Paragraph 4.3.3, is applied to the input precipitation grids, but not included in the lapse rate estimates. Another source of uncertainty is the fact that only the main valley of the Dudh Kosi

River is gauged, Consequently, the estimated lapse rate at high altitude might resent from topographical effects, thereby not being representative for the whole catchment.

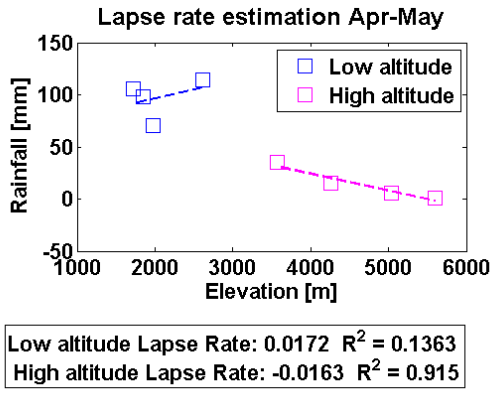

(a) Pre-monsoon season

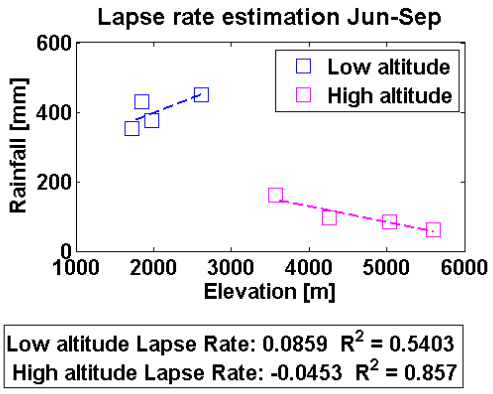

(b) Monsoon season

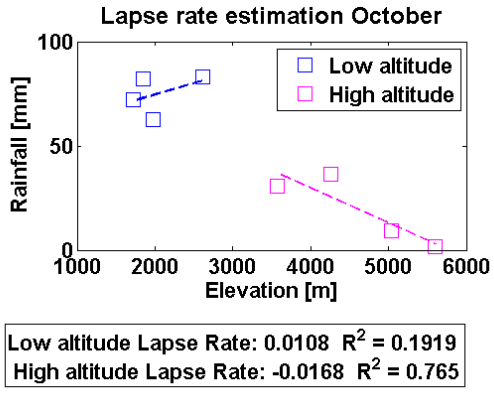

(c) Post-monsoon season

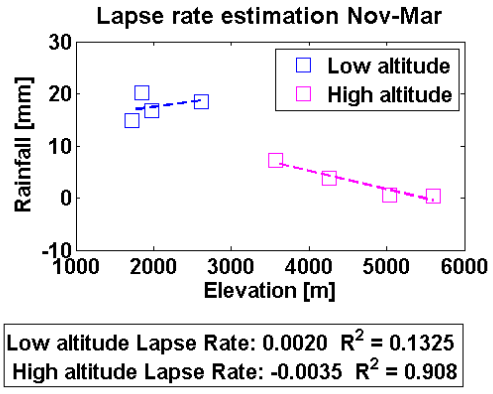

(d) Winter season

Figure 4.11: Lapse rate estimation from the monthly mean cumulative rainfall for low and high altitude stations and for each season. Data from ground stations only.

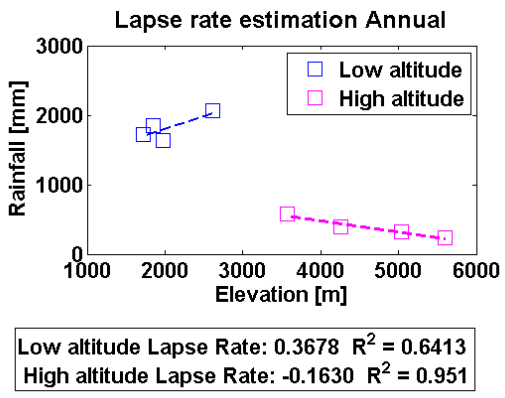

Figure 4.12: Lapse rate estimation from the annual mean cumulative rainfall for low and high altitude stations. Data from ground stations only.

4.2.3.2 Spatial distribution

The objective is to create rainfall fields that agree with the known values of precipitation, i.e. at ground stations, and at the same time entail the spatial patterns described by remote sensing data. TRMM scenes are re-scaled so that the rainfall amount at the stations' pixels match the observed ground data. Indeed, TRMM is well−known for overestimating rainfall totals (Bookhagen & Burbank 2006). Given the previously discussed unreliability of TRMM for high altitudes, TRMM scenes are used only at low altitudes, i.e. in the Thiessen polygons having DHM stations as reference stations. At higher altitude, the lapse rate method is used. TRMM scaling is in the form

$$R_{cell} = \left(\frac{\bar{R}_{cell}^{TRMM}}{\bar{R}_{ref}^{TRMM}} \right) R_{ref}^{station} \tag{4.4}$$

where $\bar{R}_{ref}^{TRMM}$ is the monthly mean cumulative rainfall from TRMM at a ground station location, $R_{ref}^{station}$ the daily observation from the same station, $\bar{R}_{cell}^{TRMM}$ the monthly mean cumulative rainfall from TRMM at the generic cell location within the Thiessen polygon of the reference station and R_{cell} the predicted daily rainfall for that generic cell.

At first, the mean monthly TRMM scenes were used throughout the whole year. However, it came out that during the driest months the use of lapse rates is preferable, as TRMM scenes often do not detect any rainfall, thus hindering the distribution of ground data. Therefore, the TRMM spatial distribution is applied only to the monsoon season (June to September) at low altitudes. The effect of such a distribution may still be relevant, as the bulk of annual rainfall totals occur during the monsoon season (Figure 4.10).

Noticeably, in this thesis a long−term mean monthly TRMM product is chosen rather than a finer temporal resolution. Indeed, Bookhagen & Burbank (2010) observed that satellite data are not acquired continuously but at maximum every three hours, whereas rainstorms in the Himalayas have a relatively short lifetime. Therefore, satellite data need to be averaged over long time scales in order to provide statistically robust rainfall amounts.

4.2.4 Precipitation distribution in the double scale modelling approach

The wider−scale model is run on both the two input rainfall grids, in order to assess the impact of rainfall distribution methods on the outcomes. However, the finer−scale model is run only on ground stations−lapse rate estimates for precipitation, for two reasons. First, the TRMM resolution is far too coarse to describe the spatial variability

at a few hundreds metres scale, and secondly, TRMM does not perform well at high altitude (Paragraph 4.2.2). Indeed, Bookhagen & Burbank (2010) advance that TRMM spatial resolution poses a limit on the minimum extent of the catchment area that can be accurately studied, being at least 100 km^2, while the catchment closed at Periche extends for merely 151 km^2.

The choice of these two different techniques for the models at two different scales finds a substantiation in literature. For instance, Wagner et al. (2012) argue that at small scales, the use of measurements from individual rain gauges might be appropriate. However at larger scales, it is required to draw special attention to the appropriate representation of the spatial precipitation patterns, which are usually interpolated from point measurements.

4.3 Snow

Snow data are obtained from different sources. Ground data consist of snow depth measurements at Pyramid AWS (5035m a.m.s.l.) for eleven years, from 2003 to 2013. Remote sensing data are retrieved from the Moderate Resolution Imaging Spectroradiometer (MODIS), located aboard the Aqua and Terra satellites. An important breakthrough compared to the previous thesis is the availability of measured snow density, both fresh and from snow-pits. These data have been collected in a field survey in May 2014 at two locations along Khumbu valley, i.e. at Pyramid station and on the Changri Nup glacier.

4.3.1 Ground station data

Pyramid AWS is the only active snow depth gauge in the catchment. It provides hourly measurements, being reduced to the daily temporal resolution of the simulation, and occasionally presents No-Data values, which are not corrected in this study. Figure 4.13 shows the dataset along with the albedo evaluated as ratio of outcoming and incoming shortwave radiation recorded at Pyramid.

Peaks in albedo correspond fairly well with peaks in recorded snow depth, suggesting that the impact of missing data on the snow measurements is limited. Some issues are visible in 2012, in which radiation data are reconstructed following the procedure detailed for temperatures in Paragraph 4.1.1.1. Snow depth measurements in 2013 were not accompanied by quality data indicators, thus they are assumed to be good not to loose information.

Figure 4.13 also shows that at Pyramid's elevation, the snow cover is absent for long periods during the year, typically from May to October.

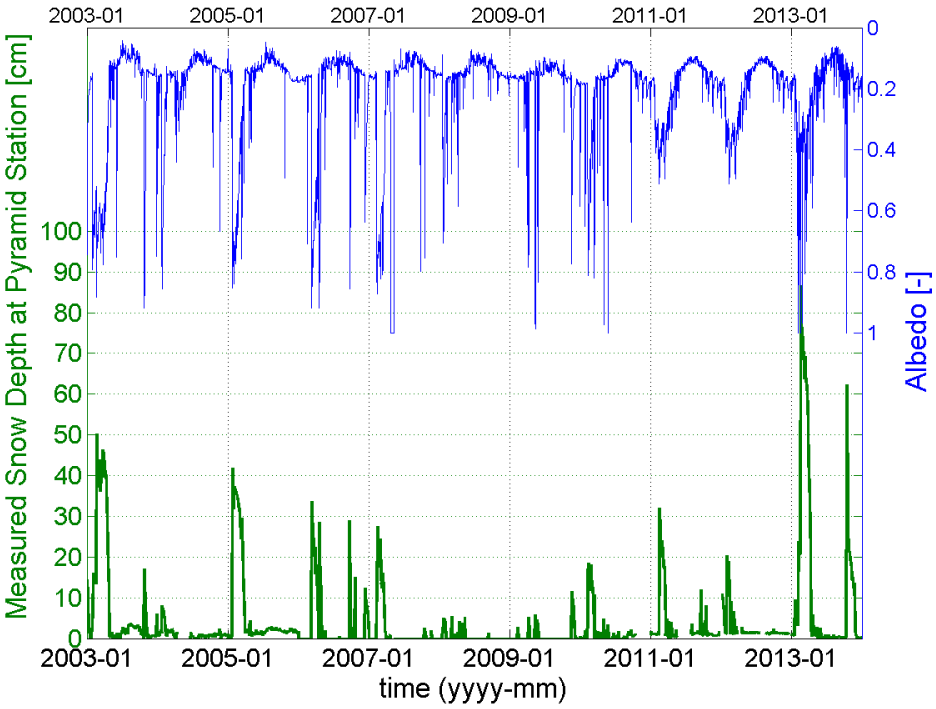

Figure 4.13: Comparison between snow depth recorded at Pyramid AWS in 2003 − 2013 and albedo calculated from Pyramid shortwave radiation in the same period.

Regarding the field survey, different data have been collected in May 2014, being the sole available measurements for snow density and Snow Water Equivalent (hereafter SWE) volume (Table 4.3). A snowpit 1.70 m deep has been realized on the Changri Nup glacier at 5613 m a.m.s.l.elevation, sampling snow cores each 15 cm along the depth. This provides an estimate for the cumulated SWE at the site. Furthermore, six snow cores have been taken on Changri Nup, up to 1.2 m deep above the ice sheet. These measurements estimate the perennial snow density. Finally, fresh−snow density are being measured at Pyramid AWS from October 2014 on, allowing for estimating the fresh snow water equivalents.

These data are used for correcting the amount of precipitation by adding the solid contribution (Paragraph 4.3.3) and, together with the remote sensing data, for calibrating the snow melt rates in the model. Given the availability of both fresh− and old−snow densities, it is possible to define two SWEs, one for freshly deposited snow for inclusion in the computation of to liquid precipitation, and another one for snow melt in the snow depletion curve at the end of the winter season (see Chapter 5).

Table 4.3: Snow densities recorded for both fresh and old snow. Density from the snowpit is averaged along depth. Six snow cores were taken, the average value for density is reported.

Type of survey	Location	Elevation [m a.s.l.]	Date	ρ [kg/m^3]
Snow cores	Changri Nup	5600	May 2014	312
Snow pit (depth 1.68 m)	Changri Nup	5613	May 2014	296
Fresh snow − sample A	Pyramid	5035	October 2014	210
Fresh snow − sample B	Pyramid	5035	October 2014	160

4.3.2 Remote sensing data

It is acknowledged that remote sensing allows detection of spatial–temporal patterns of snow cover across large areas in inaccessible terrain, providing useful information on a critical component of the hydrological cycle (Immerzeel et al. 2009).

Given the scarcity of snow gauges, satellite data are retrieved in order to gain knowledge about the extent and seasonal behaviour of snow cover in the study area. The MODIS product MODIS Snow Cover Monthly L3 Global CMG (MOD10CM)[4] is acquired from both Aqua and Terra satellites. Terra's orbit around the Earth is timed so that it passes from north to south across the equator in the morning, while Aqua passes south to north over the equator in the afternoon[5]. The product that is chosen has 0.05° horizontal resolution and monthly temporal resolution. MODIS grids are resampled at model cells size and snow pixel are extracted over the study area. Possible issues with the MODIS product could be given by cloud cover, but no quality status is associated to the data.

It has to be noticed that MODIS scenes only provide information about the extent of the snow cover rather than on snow depth. Thus, they will be used to calibrate the snow melt rates by comparing the simulated and observed presence of snow in each cell of the basin, at a monthly temporal resolution.

4.3.3 Precipitation amounts correction

As mentioned in Paragraph 4.2, neither rain gauges nor TRMM scenes provide a good estimate of solid precipitation. Ground stations are not equipped with heaters, hence the snowfall cannot be converted in Snow Water Equivalent heights. TRMM microwaves sensor faces problems in separating falling snow from ground snow and ice sheets, whereas

[4]Hall, Dorothy K., George A. Riggs, and Vincent V. Salomonson. 2006, updated monthly. MODIS Snow Cover Monthly L3 Global 0.05Deg CMG V005, 01/01/2003 to 01/01/2014. Boulder, Colorado USA: National Snow and Ice Data Center. Digital media.

[5]http://modis.gsfc.nasa.gov/about/ [Accessed 30th October 2014]

the space-borne radar can see atmospheric snow but introduces great uncertainties in converting it to equivalent water amounts[6].

Therefore, it is necessary to correct the observed rainfall for the missing solid precipitation. In this study, this has been made possible by the snow density measurements executed in the field survey on May, 2014. The daily snowfall amount is computed by differentiating the daily snow depth time series recorded at Pyramid AWS. By means of the fresh snow density, the daily snowfall is converted in water equivalents with the well known formula

$$SWE = h_{snow} \left(\frac{\rho_s}{\rho_w} \right) \tag{4.5}$$

where h_{snow} is the daily snowfall, i.e. the positive difference between two consecutive days of the measured snow depth, ρ_w is the liquid water density (1000 kg/m^3) and ρ_s the fresh snow density, as given in Table 4.3.

The snow water equivalent volume is then added to the daily liquid precipitation observed at the high altitude stations (above 3000 m a.s.l.), i.e. Namche, Periche, Pyramid and Kala Patthar. Lower stations are not considered as mean daily temperatures at their locations are incompatible with solid precipitation. With respect to spatial distribution, the high altitude lapse rate calculated in Paragraph 4.2.3.1 is applied to snowfall, lacking any further information.

Figure 4.14 shows the outcomes of the correction procedure. Unfortunately, information about snow depth data quality was not made available, hence it is not possible to assess the reliability of the precipitation peaks observed in Figure 4.14. As expected, the effects are relevant for the months from October to April/May, when snowfall occurs at Pyramid. Although this holds for cells at lower elevations than Pyramid, at higher altitudes it results impossible to accurately model the precipitation amounts occurring during summer months, having to extrapolate the rainfall gradient. As discussed in Paragraph 4.2.3, this issue might not be very relevant as the bulk of summer (monsoonal) precipitation occurs before the southern storm cells can reach the upper parts of the valleys.

Quantitatively, rainfall constitutes the 87%, 80%, 77% and 64% of estimated total precipitation at Namche, Periche, Pyramid and Kala Patthar station, respectively. These percentages represent a rough estimate and may not be accurate; nevertheless, this approach is the only practicable way to account for the missing volumes from the observations, and allows for good snow depth simulations.

[6] http://trmm.gsfc.nasa.gov/ [Accessed 30th October 2014]

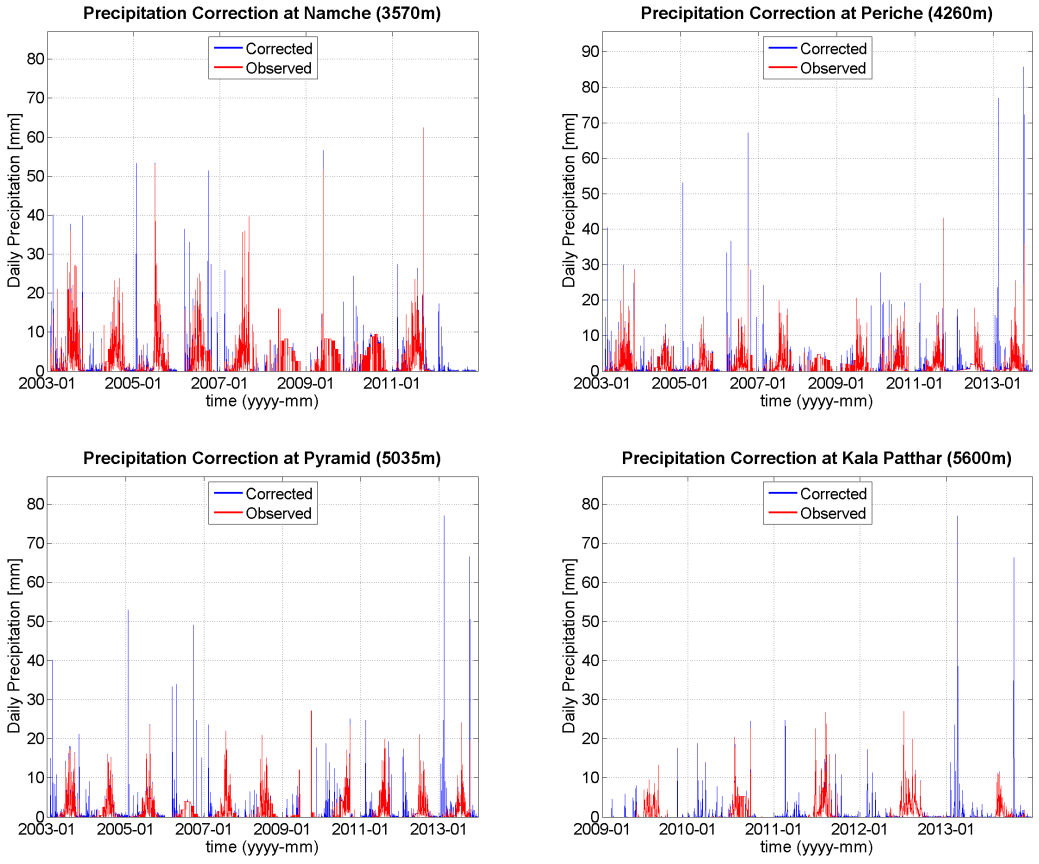

Figure 4.14: Comparison of observed daily rainfall and estimated total precipitation for high altitude stations, in the period 2003−2013.

4.4 Ice melt rates

Melt parameters are estimated using data from ablation stake measurements on Changri Nup and Khumbu glaciers during the period May 2014 to October 2014. Melt parameters are discriminated between debris covered and debris−free glacier areas, in order to take into account the melt enhancing or reducing effect of the debris cover. Tables 4.4 and 4.5 show the observed mean ice ablation for clean and debris covered ice, respectively. The stakes locations are shown in Figure 4.17.

Ice melt is computed by measuring the distance from stake top and ice surface in different moments of the year; since the time interval is known, it is immediate to retrieve melt rates.

For clean ice, the degree day factor is also estimated (Table 4.4), whereas for debris covered ice a distributed surface energy balance modelling approach is used (Paragraph 3.2.2). The degree day factor for clean ice (hereafter DDI) is calculated as ratio of the mean daily ablation and the mean daily cumulated positive temperature. The mean

value of the resulting DDDIs is 7, and it will be used in the temperature index model. Hybrid model parameters, instead, are not estimated separately for ice and snow, thus will be calibrated (see Paragraph 5.2.1).

Table 4.4: Observed debris−free ice melt rates at three locations over Changri and Khumbu glaciers.

Stake ID	Date	Local Time	Elevation [m]	Mean daily ablation [mm/d]	DDI [mm/d°C]
Cw1	4-May-14	13:16	5612.76		
	18-Jun-14	-		8.91	1.70
Kw1	8-May-14	18:14	5255.70		
	8-Jul-14	13:30		36.13	6.73
	4-Sep-14	10:30		44.07	8.15
Kw2	8-May-14	16:21	5237.22		
	8-Jul-14	13:30		29.34	5.46
	4-Sep-14	10:30		38.31	7.08
	9-Oct-14	10:30		29.17	10.58

Table 4.5: Observed debris−covered ice melt rates at four locations over Khumbu glacier.

Stake ID	Date	Local Time	Elevation [m]	Debris Thickness [cm]	Mean daily ablation [mm/d]
Kb1	9-May-14	9:53	5257.2		
	8-Jul-14	13:30		5	19.4
	4-Sep-14	10:30		2	22.9
	9-Oct-14	10:30		4	10.6
Kb2	9-May-14	11:25	5234.5		
	8-Jul-14	13:30		8	13.8
	4-Sep-14	10:30		4	22.6
	9-Oct-14	10:30		5	14.0
Kb4	8-Jul-14	13:30	5055.6		
	4-Sep-14	10:30		4	47.1
	9-Oct-14	10:30		4	32.9
Kb5	10-May-14	11:10	5053.0		
	8-Jul-14	13:30		5	40.3
	4-Sep-14	10:30		4	29.6
	9-Oct-14	10:30		4	19.7

4.5 Spatial distribution of debris thickness and ice melting

Debris cover affects the glacier melting process by altering surface ablation rates and spatial patterns of mass loss. In the Khumbu Hymalayas, debris covered glaciers are, on average, 15 times larger in area and 5 times longer in length than clean−ice glaciers (Fujii & Higuchi 1977), and constitute 80% of the glacieted area; hence modelling ice ablation under debris cover is of paramount importance. As discussed in Paragraph 3.2.2, ice melt under debris cover strongly depends on the thickness of the debris cover, thus a spatially distributed model for debris thickness is required.

In this study, debris thickness data at four locations on the Khumbu and Changri Nup glaciers are available, along with measurements of ice depths over five months, so that ablation rates can be estimated and related to the corresponding debris thickness. Punctual ground data are integrated with remote sensing estimates of debris thickness in order to distribute this quantity, thereby creating a debris−thickness map over the glacier.

The following steps are implemented. Paragraph 4.5.1 describes the procedure to process remote sensing data in order to obtain the debris cover map and the surface temperature over the debris layer. Paragraph 4.5.2 illustrates how to retrieve debris thickness from surface temperatures and finally Paragraph 4.5.3 shows the relation between ice ablation and debris cover thickness.

4.5.1 Landsat Imagery

Landsat represents the world's longest continuously acquired collection of space-based moderate-resolution land remote sensing data[7]. It is a joint initiative between the U.S. Geological Survey (USGS) and the NASA, intended for the acquisition of high-quality data for observing land use and land change. In this study, both Landsat 7 Enhanced Thematic Mapper Plus (ETM+) and Landsat 8 scenes are used. Landsat 7 data are retrieved over the simulation period in order to map the debris cover area at that time. A Landsat 8 scene is used to determine the surface temperature at the same time as the debris thickness and ablation rates were sampled - i.e., on May 4, 2014. Landsat 8, launched in 2013, is preferred to Landsat 7 as it does not present the No−Data stripes produced by the failure of the Scan Line Corrector (SLC), which compensates for the forward motion of Landsat 7. Moreover, the data quality (signal to noise ratio) is higher for Landsat 8than previous Landsat instruments[7].

[7]http://landsat.usgs.gov/ [Accessed 1st November 2014].

4.5.1.1 Debris cover map

The glacier's area covered by debris is outlined by means of an automatic image classification procedure. A Landsat 7 scene is selected dating to the simulation period and being as free as possible from clouds and snow on the ground. The scene from December 2002 is chosen, as it lacks the SLC-off stripes which would condition the classification. A number of Regions of Interest (ROI) is drawn on the debris covered areas, recognized by visual inspection of the RGB Landsat image. The ROIs are chosen to be as representative as possible of the debris characteristics, as they are used to train the Supervised Maximum−Likelihood Classification. This algorithm extracts the debris covered areas depending on their probability to resemble the ROIs, once a probability threshold is set. Finally, the classified image is clipped with the glaciated area from the ICIMOD gacier inventory in order to select only the pixels effectively belonging to the glacier. Figure 4.15 shows the input RGB image and the output debris cover map.

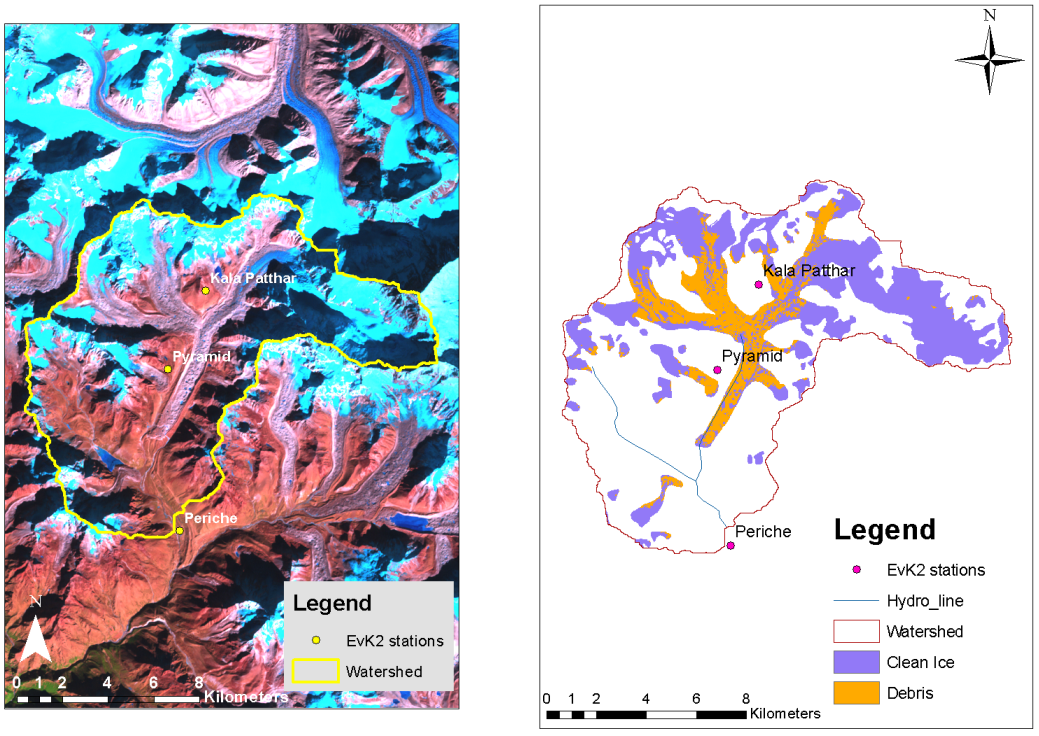

(a) Landsat RGB

(b) Debris cover map

Figure 4.15: Landsat 7 RGB image of Khumbu glacier and debris covered area resulting from the automatic classification.

By visual comparison of the two images, the result of the classification is deemed good. Only at the terminus it indicates the presence of clean ice where probably it is covered by

debris. The several spots along Khumbu glacier may correspond to supraglacial ponds; finally, the debris map performs well in the area of the Icefall, where no debris cover is seen.

4.5.1.2 Surface temperature calculation

The Landsat 8 scene which is closest in time to the field work dates May 22, 2014, as the Landsat 8 satellite images the entire Earth every 16 days[7]. The thermal Infrared Sensor (TIRS) band 10 is downloaded from the U.S. Geological Survey Earth Resources Observation and Science (EROS) Data Center[8], having an horizontal resolution of 100 m. Landsat scenes consist of digital numbers (DNs) representing the acquired data in each band. The DNs are converted to temperature in a three step process[9].

First, DNs of the thermal band are converted to spectral radiance:

$$L_\lambda = M_L \; DN \; + A_L \tag{4.6}$$

where L_λ is the spectral radiance $[W/m^2 \; srad \; \mu m]$, M_L and A_L the band-specific rescaling factors from the metadata, DN the band Digital Numbers.

A scene-specific atmospheric correction is applied according to Coll et al. (2010):

$$L_{corrected} = \frac{L_\lambda - L_{up}}{\epsilon\tau} - \frac{1-\epsilon}{\epsilon} \; L_{down} \tag{4.7}$$

where $L_{corrected}$ is the atmospherically corrected radiance value $[W/m^2 * srad * \mu m]$, L_λ the radiance from eq. (4.6), L_{up} and L_{down} respectively the upwelling and downwelling radiance, ϵ the emissivity (set to 0.95 as suggested if no information is available) and τ the transmittance. These parameters are calculated by means of the Atmospheric Correction Parameter Calculator[10] based on geographical and temporal coordinates of the Landsat data.

Finally, the inverse of the Planck function is applied to derive temperature values at each pixel:

$$T = \frac{K_2}{\ln\left(\frac{K_1}{L_{corrected}} + 1\right)} \tag{4.8}$$

where T is the at-satellite brightness temperature $[K]$, $L_{corrected}$ the spectral radiance $[W/m^2 * srad * \mu m]$, K_1 and K_2 band-specific thermal conversion provided in the metadata.

[8] http://earthexplorer.usgs.gov/ [Accessed 1st November 2014].

[9] The procedure is taken from http://landsat.usgs.gov/Landsat8-Using-Product.php [Accessed 1st November 2014]

[10] http://atmcorr.gsfc.nasa.gov/ [Accessed 1st November 2014].

The resulting surface temperature map is shown in Figure 4.16.

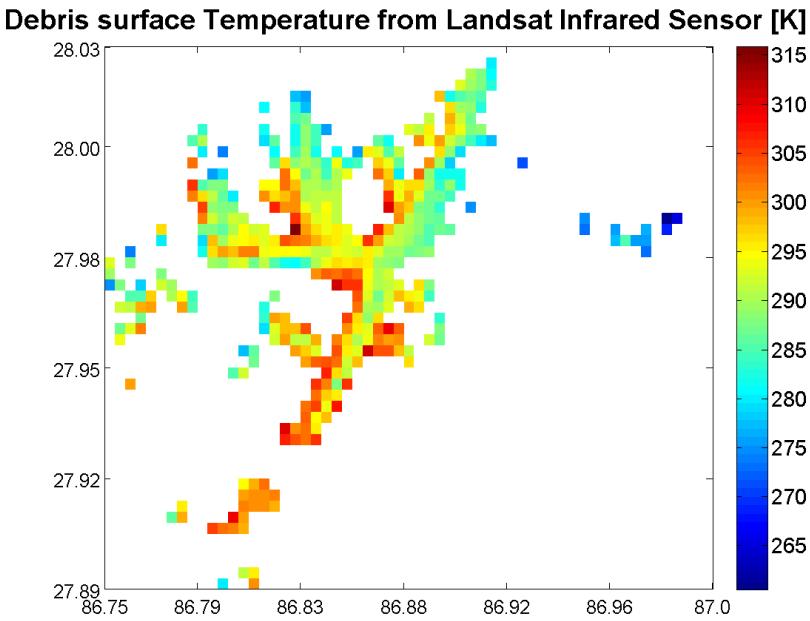

Figure 4.16: Surface Temperature map of the debris cover, derived from Landat 8 thermal band 10 acquired on May 22, 2014.

The surface temperatures in 4.16 are similar to those found by Casey et al. (2012), both in distribution and absolute values. Noticeably, pixels covering the lateral moraines display high temperatures, up to 315 K. Indeed, Coll et al. (2010) reports that Landsat thermal data may provide surface temperature estimates within an accuracy of ± 1 K, but targets such as bare surfaces and semiarid areas may have lower emissivities (hence increasing the impact of reflected downwelling sky irradiance), with larger variability and uncertainty. However, as expected, in the areas close to the Khumbu Icefall and mountain ridges, where bare ice is exposed, surface temperatures drop to 0°C and below.

4.5.2 Debris thickness estimation

Two datasets of debris thicknesses are used in this study, both sampled between May and October 2014 via manual excavation. They are extremely valuable for modelling the cryospheric processes, also given that few other surveys of debris thickness have been performed in the Everest area, due to the labor-intensive nature of this work (Rounce & McKinney 2014). The first dataset consists of random samplings in a circular area of 30m radius. The sample circle is divided into 4 zones equally sized, and for each zone 5 samples are taken randomly; the final thickness is the average value from these samples, thereby being representative of the area. The second dataset comprises

punctually sampled thicknesses; although less representative, these data are necessary to increase the size of the sample and thereby allowing for interpolation, as described in the following. Figure 4.17 shows the location of the sampled points on the glacier, over the 300 m resolution debris map.

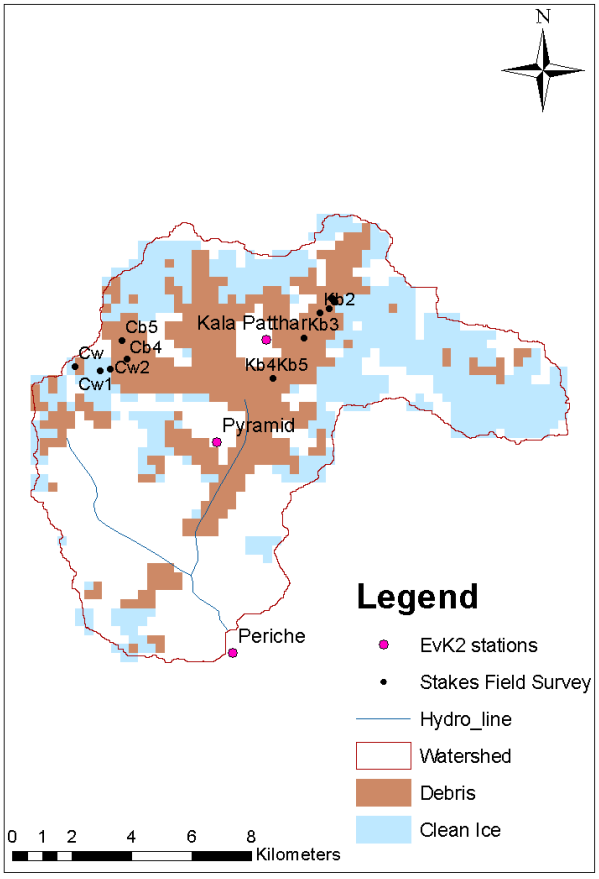

Figure 4.17: Sampled locations: the letter w indicates clean ice samples, b location on debris covered ice.

Land surface temperatures are used to spatially distribute the observed debris thicknesses. An empirical relation is established between Landsat temperatures at the field survey samples' locations, and the sample thicknesses, in the form

$$DT = exp(0.237\ T_s - 66.95) \tag{4.9}$$

where DT is the debris thickness and T_s the surface temperature $[K]$. This function fits the data very well ($R^2 = 0.92$). Also Mihalcea et al. (2008) found the best interpolant function to be exponential. Figure 4.18 shows the interpolation, while Figure 4.19 illustrates the debris cover map obtained by applying the interpolant function to the Landsat temperature grid. The horizontal resolution is 100 m.

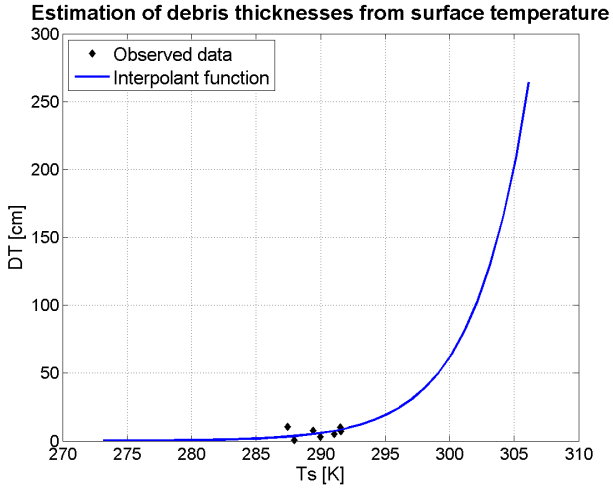

Figure 4.18: Empirical interpolant function for the observed debris thicknesses and the Landsat surface temperatures.

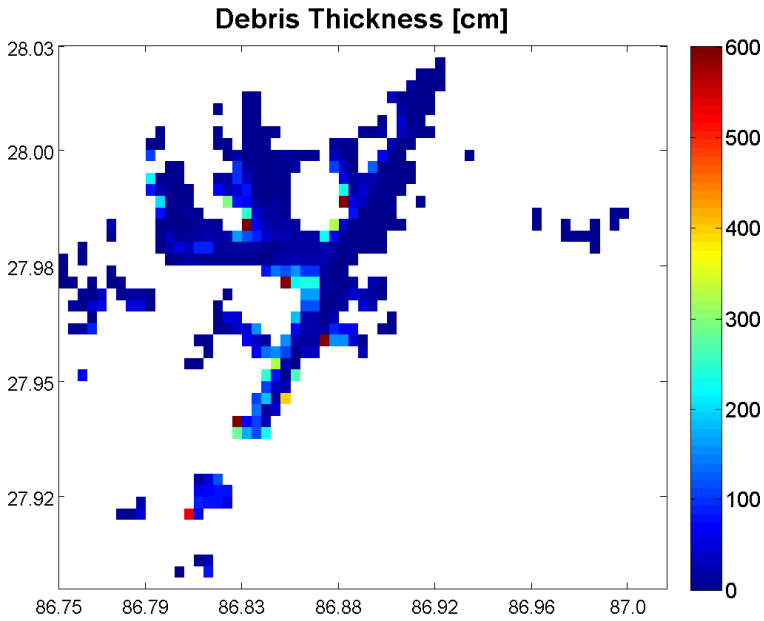

Figure 4.19: Debris thickness map of Khumbu glacier, derived from Landsat surface temperatures.

As can be seen in Figure 4.19, the debris thickness increases towards the tongue of the glacier, being few centimetres (0 to 5 cm) close to the Everest base camp and up to 200 cm on the terminus. This is expected, since slopes are gentler towards the tongue, thus debris do not move downwards. Higher values are observed for the lateral moraines, as Rounce & McKinney (2014) and Nakawo et al. (1986) also found. The debris thicknesses in Figure 4.19 and their spatial distribution are consistent with those found by the few other studies in the Everest region (Nakawo et al. 1986, Mihalcea et al. 2008, Nicholson

& Benn 2013, Rounce & McKinney 2014).

Two main limitations are recognized in this analysis. First, no debris thickness has been sampled downglacier, where thicknesses are higher, thus the relation with surface temperatures is calibrated for small thicknesses and has to be extrapolated for greater ones. This could lead to inaccuracy in estimation of the debris thickness at the glacier's terminus. Secondly, as can be easily recognized from pictures of the study area, debris thickness varies widely over small distances. Nicholson & Benn (2013) reports that, on Ngozumpa glacier, debris thickness varies between 0.5 and 2.0m within an area of few tens of square metres, both as cause and result of the uneven surface topography. However, Landsat scenes provide information averaged in a 100m x100m pixel, thus the resulting thickness map cannot model trends related to slope and aspect. Nonetheless, it has to be acknowledged the value of remote sensing in this analysis, since it allows for deriving reasonable debris thicknesses over the whole study area.

4.5.3 Ice melting and debris thickness relation

The relation between debris thickness and underlying ice ablation is investigated. Observations consist of ice and debris thicknesses at four locations on Khumbu glacier during the melting season, from May to October. Ice ablation rates are evaluated from the differences of ice heights recorded by stakes observation over the known periods of time. An empirical relation is interpolated from the dataset, as shown in Figure 4.20. Two constraints are imposed, i.e. the ice ablation for clean ice (null debris thickness), calculated from field measurements on bare ice, and the ablation at 40 cm debris thickness, which in literature is accepted to be 0.4 cm/d (Mattson 1993). Both debris thickness and ice ablation varies with time.

As it can be immediately seen in Figure 4.20, measurements are highly dispersed; indeed, the interpolant function scores only $R^2 = 0.34$. This is probably due to the aforementioned extreme spatial variability of debris thicknesses over short distances; however, there might be other control factors for ice ablation other than debris thickness, e.g. the solar radiation and meteorological conditions. Another limitation lies in the fact that with the Landsat horizontal resolution is too coarse to analyse the effects of slope and aspect, as already discussed.

Some information can be derived from the interpolated relation. The maximum estimated ablation rate is 3.24 cm/d, corresponding to a debris depth of 1.4 cm. For deeper debris layers, ice ablation decreases. The critical thickness, i.e. the thickness that determines the same ablation as for clean ice (3.14 cm/d, on average), amounts to 3.15 cm; at any greater thickness ice ablation is hindered by the debris cover. Instead,

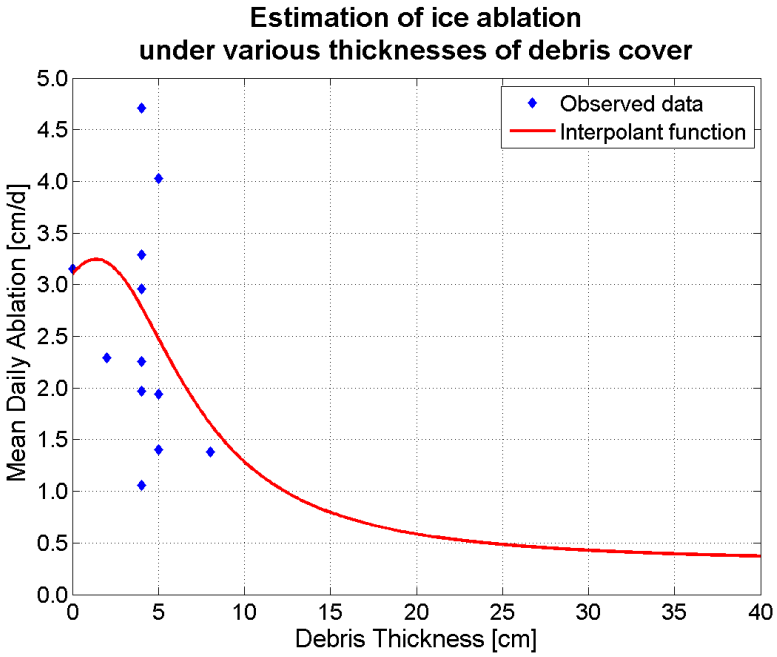

Figure 4.20: Interpolation of mean daily ice ablation under various thicknesses of debris cover, sampled over the Khumbu glacier between May and October 2014.

with thicknesses up to 3.15 cm, the debris cover enhances ice ablation. Mattson (1993) reviews the results of similar analysis carried out in the Himalayas. Critical thicknesses range from 2 to 4 cm, while maximum ablation is estimated between 1 cm and 2 cm. For Khumbu glacier, Takehuci (2000) found that thicknesses from 0 to 5 cm enhance ice ablation, peaking at 0.3 cm, whereas debris thicker than 5 cm retards ablation. The results in this thesis are aligned with the ones from previous studies.

4.6 Ice thickness and basal shear estimation

Ice thickness and basal shear stress are needed in order to quantify the flow velocity of the glacier. Few studies have been carried out estimating ice thicknesses, and even fewer directly measuring it, due to the intrinsic difficulties in sampling and consequently in modelling the control factors of glacier flow.

On Khumbu glacier, Kodama & Mae (1976) retrieved ice thickness from measured surface velocities, ranging from 350 m below the Everest Base Camp (EBC) to 110 m at Gorak Shep (GS); however, the following year, the estimate at GS is 400 m, showing the huge uncertainties affecting these calculations. Moribayashi (1978) estimated ice thickness by gravimetrical profiles being 400 m at EBC, 220 m at GS and 50 m at Lobuche, about 2 km from the terminus. More recently, Gades et al. (2000) executed radio echo

sounding through the debris layer finding that ice thickness varied from 440 m about 0.5 km below the icefall (EBC) to less than 20 m at Lobuche.

At first, basal shear stress is estimated according to the measured ice thicknesses found in literature and from the observed surface slope on the Digital Elevation Model (DEM) of the area. The glacier is modelled as a parallel-sided slab of ice, resting on an indefinite plane of slope α. Hence, surface slope governs the flow and small scale irregularities are neglected. Here ice flow is assumed to be unidimensional along the local direction of maximum slope.

$$\tau = \rho_{ice}\ g\ h_{ice}\ sin(\alpha) \tag{4.10}$$

where τ is the basal shear stress [Pa], $\rho_{ice} = 917\ kg/m^3$ the ice density, g the gravitational attraction (9.81 m/s^2), h_{ice} the ice thickness [m] and α $[rad]$ the local slope, derived from the 30 m DEM. It has to be noticed that local slope displays great spatial variability, so that it might introduce uncertainties in the calculation. However, the resulting shear stress from (4.10) is deemed to be unreliable, as affected by too large uncertainties. Indeed, ice thickness values date back to 2000 and might have changed in such a long time span, also given the well known disequilibrium state of the glacier.

Therefore, the average value of 150 kPa (Cuffey & Paterson 2010, p. 297) is attributed to the shear stress and ice thickness is computed by inverting (4.10). The resulting map of ice thicknesses is shown in Figure 4.21.

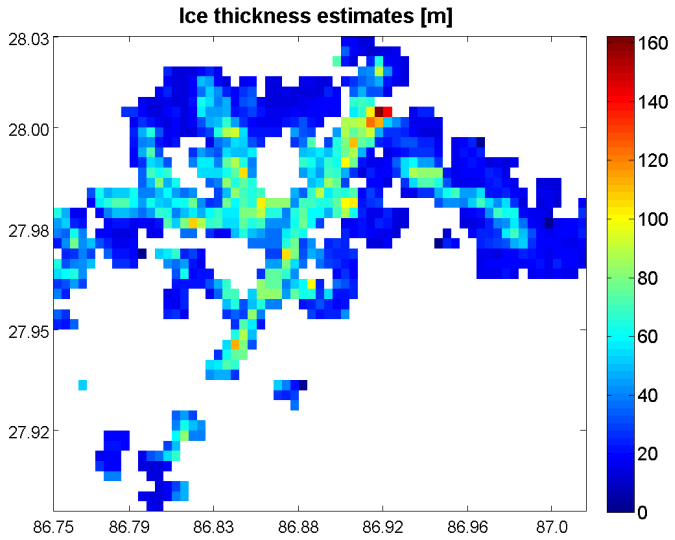

Figure 4.21: The estimated ice thickness for Khumbu glacier, assuming laminar flow and basal sliding as motion type.

Reasonably, the ice is thicker at the BC, where an accumulation zone might develop as the slope abruptly decreases and the glacier turns left; at the icefall, where the slope is maximum, the thickness is minimum. Estimated thicknesses thus range from 160 m under the BC, to 100 m at GS and 40 m at the terminus. The spatial distribution of ice thickness is consistent with expectations; however these values could not be validated with field observations.

Chapter 5

Results

The hydrological model set up in Chapter 3 and fed with input data described in Chapter 4 is tuned with historical records of meteorological and hydrological data. Two separate calibration routines are applied for the wider and smaller catchments. In both cases, the model presents several calibration parameters, so that tuning all of them on a single discharge time series constitutes a badly conditioned problem. Therefore, snow and ice melt modules are optimized with recorded snow depths and ice melt observations.

Paragraph 5.1 illustrates the adopted calibration strategies. Paragraph 5.2 shows the results for the catchment closed at Rabuwa Bazar; model performance is discussed for the different flow regimes and furthermore the influence of the meteorological input dataset choice is examined. Paragraph 5.3 presents the tuning process for the catchment closed at Periche. The implementation of detailed glacial hydrology routeflow allows for a more accurate, physically based calibration of discharge series (Paragraph 5.3.3). Observed snow depth and ice ablation rates allows for calibrating the melt model parameters (Paragraphs 5.3.1 and 5.3.2), whereas velocity measurements are used to optimize the glacier dynamics parameters (Paragraph 5.3.4).

5.1 Calibration technique

Conceptual models as those implemented in this study entail parameters that are either difficult or impossible to directly measure. Applications of these models therefore require that model parameters are adjusted so that model predictions closely replicate the observed environmental system response data. There exist a number of strategies for calibrating model parameters, from manual adjustment to automatic optimum search algorithms. In this thesis, because of the complex and non-linear nature of the model,

an automatic calibration based on the Uniform Random Sampling method, a simple probabilistic approach to global optimization, is implemented.

First, for each parameter the domain is defined, based on the literature values retrieved along with the formulas (see Chapter 3 for references). Second, for each parameter a set of values is randomly generated by sampling from a probability distribution defined over the domain. A uniform probability distribution is assumed for all parameters. Third, several (thousands) sets of input parameters are created by combining the randomly sampled values, and the model is run for each set of randomly sampled parameters. For each run, the goodness of fit is evaluated by means of indexes or visual inspection of the output time series, as detailed in Paragraphs 5.2.1 and 5.2.2). Once the automatic procedure has returned the optimal set of parameters, manual tuning of those is performed, as it occasionally allows for improvements in the fit.

As objective function for the calibration, a number of indexes of goodness of fit are calculated and maximized or minimized, depending whether they describe the efficiency or the model error, respectively:

$$NSE = 1 - \frac{\sum_{i=1}^{n} (O_i - P_i)^2}{\sum_{i=1}^{n} \left(O_i - \overline{O}\right)^2} \tag{5.1}$$

$$\ln_{NSE} = 1 - \frac{\sum_{i=1}^{n} (\ln O_i - \ln P_i)^2}{\sum_{i=1}^{n} \left(\ln O_i - \ln \overline{O}\right)^2} \tag{5.2}$$

$$R^2 = \left(\frac{\sum_{i=1}^{n} \left(O_i - \overline{O}\right)\left(P_i - \overline{P}\right)}{\sqrt{\sum_{i=1}^{n} \left(O_i - \overline{O}\right)^2} \sqrt{\sum_{i=1}^{n} \left(P_i - \overline{P}\right)^2}} \right)^2 \tag{5.3}$$

$$RMSE = \sqrt{\frac{\sum_{i=1}^{n} (P_i - O_i)^2}{n}} \tag{5.4}$$

$$d = 1 - \frac{\sum_{i=1}^{n} (O_i - P_i)^2}{\sum_{i=1}^{n} \left(|P_i - \overline{O}| + |O_i - \overline{O}|\right)^2} \tag{5.5}$$

where P_i denotes discharge predictions at step i, O_i discharge observations and n is the length of the simulation.

Several efficiency criteria are confronted in order to gain indications on different aspects, and to compensate for the individual disadvantages (Krause et al. 2005). By squaring the differences, the Nash−Sutcliffe Efficiency (NSE, eq. (5.1)) weights more large values, therefore is used to describe the goodness of fit of high flows. Conversely, by taking

the logarithm of the NSE (eq. (5.2)), higher weight is given to the accordance of low values, i.e. to low flows. NSE ranges between 1 (perfect fit) and $-\infty$, with negative values indicating that the mean of the observation is a better predictor than the model. The coefficient of determination (eq. (5.3)) estimates the combined dispersion against the individual dispersion of the observed and predicted series, ranging from 0 (no correlation) to 1 (full correlation). R^2 thus describes the dispersion but does not provide any information on possible systematic errors. The root mean square error (eq. (5.4)) indicates the magnitude of the error in predictions. Finally, the index of agreement (eq. (5.5)) represents the complement to the ratio of the mean square error and the potential error, ranging from 0 to 1. As the NSE, it is very sensitive to peak flows and insensitive for low flow conditions (Krause et al. 2005).

These indexes provide an useful tool for choosing the best combination of parameters; however, they are not intended to substitute the visual comparison of modelled and simulated time series, since they all suffer from some limitation in globally assessing the fit. Further, multiple sets of parameters could return the same model error or efficiency, as they are merely lumped indicators of the goodness of fit. Visual inspection remains thus fundamental for hydrological calibration.

5.2 Wider-catchment calibration and validation

The hydrological model for the catchment closed at Rabuwa Bazar is alternatively fed with ground stations data or satellite data; the performances of the temperature index and hybrid models are also compared. Discharge records at Rabuwa Bazar are available over the period $1992 - 2011$, missing year 2009; however, climatic data from EvK2 only starts in 2003, thereby previous years cannot be covered by the simulation. Furthermore, as discussed in Paragraph 4.2.1.1, rainfall observations are missing at multiple stations in 2006, thus it has been chosen to exclude that year from the simulation, as it is believed that not enough input data are present. Hence, the interval $2003 - 2005$ is taken as calibration period, whereas the model is validated over the years $2007 - 2008$ and $2010 - 2011$.

The hydrological model has six parameters that need to be optimized; calibrating all of them on a single discharge time series still leaves five degrees of freedom, i.e. the problem is badly conditioned. Therefore, further constraints are sought for within the available data. First step of the calibration consists in finding the optimal values for the snow and ice melt module. Afterwards, the remaining routeflow parameters are tuned with the observed discharge.

5.2.1 Snow and ice melt parameters - calibration and validation

For both the temperature index and the hybrid models, snow melt parameters are calibrated with the observed snow depth series at Pyramid AWS, being the sole snow gauge in the basin. The degree day factor for ice, instead, is calculated by averaging the observed ice melt rates; ice melt is not discriminated between debris−covered or debris−free cells as the spatial resolution at this scale is too coarse for that (Paragraph 4.4). Noticeably, snow and ice melt parameters for the hybrid model are kept the same not to excessively increase the degrees of freedom in the model. On the other hand, Pellicciotti et al. (2005) do not use different values for ice and snow.

Figure 5.1 shows the snow depth and cumulative time series used for calibrating the degree day factor for snow. The validation period is shown in Figure 5.2. Noticeably, a very good agreement with observations is obtained for the calibration period. The validation period is worse reproduced, nonetheless still satisfactorily; the presence of several missing data might affect the comparison of the cumulative snow depth.

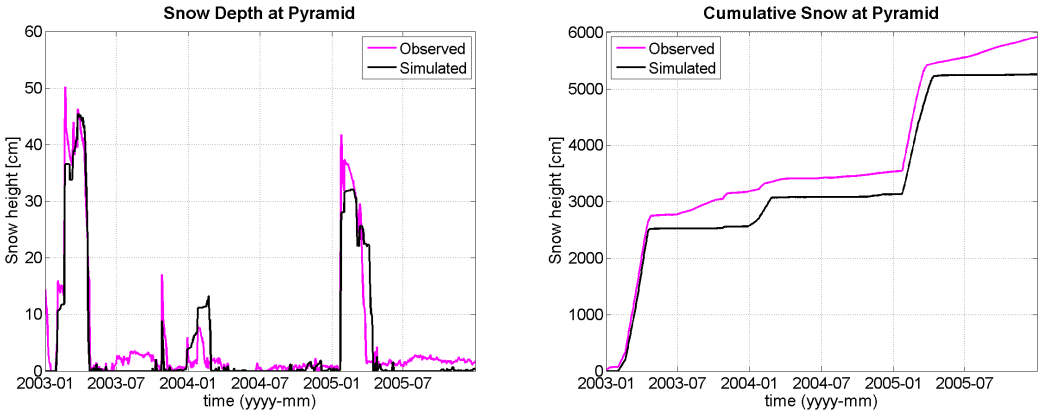

Figure 5.1: Calibration of the degree day factor for snow: observed and simulated time series of snow depth(left) and cumulative snow height (right).

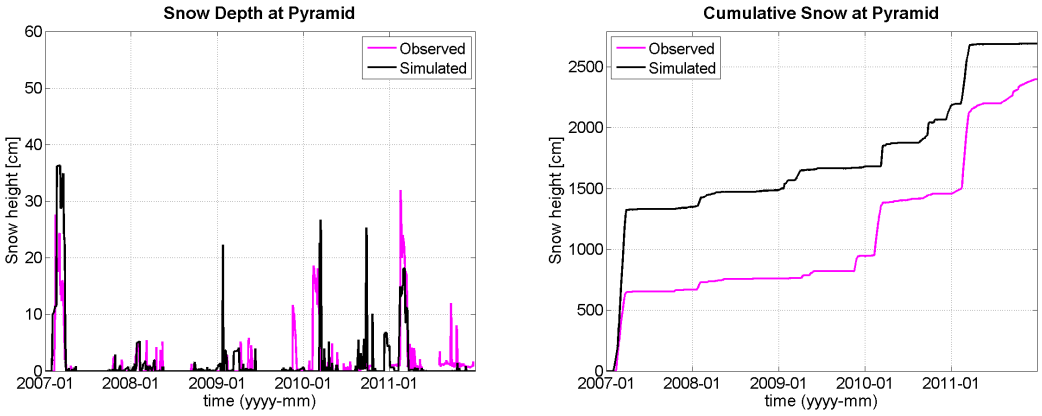

Figure 5.2: Validation of the degree day factor for snow: observed and simulated time series of snow depth(left) and cumulative snow height (right).

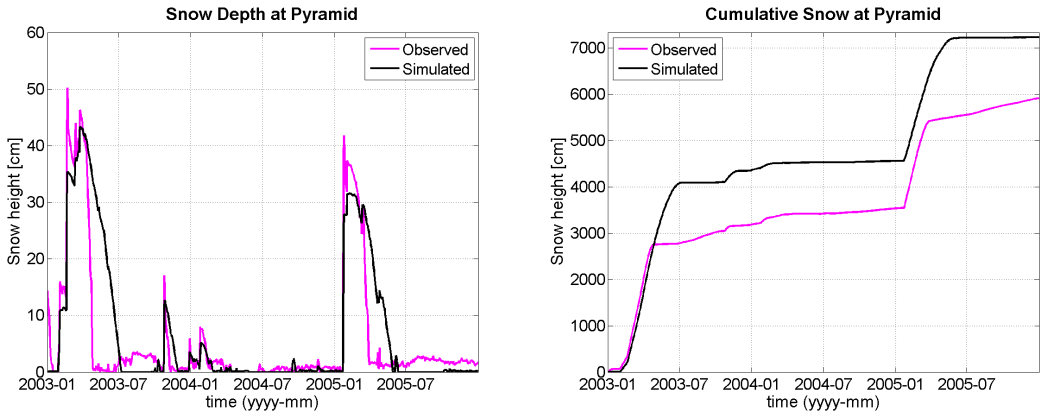

Figure 5.3: Calibration of the hybrid model parameters: observed and simulated time series of snow depth(left) and cumulative snow height (right).

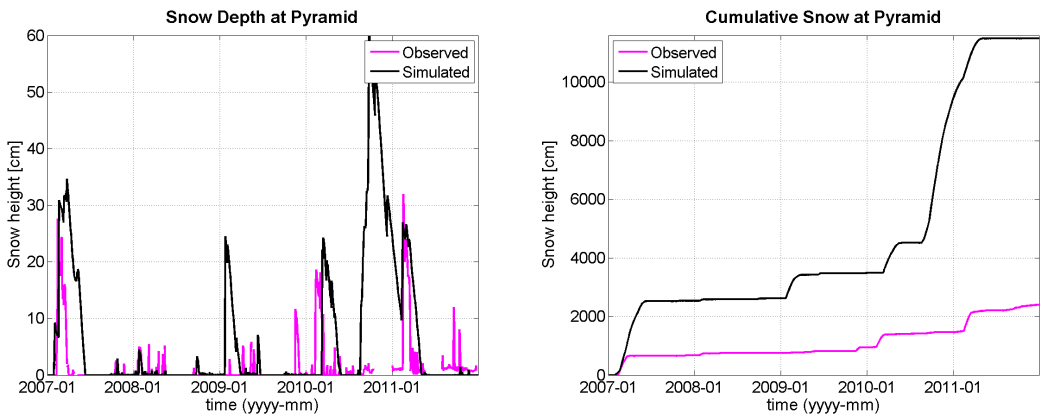

Figure 5.4: Validation of the hybrid model parameters: observed and simulated time series of snow depth(left) and cumulative snow height (right).

Thereafter, the calibration (Figure 5.3) and validation (Figure 5.4) time series for the hybrid model are shown. The calibrated parameters for both the models are reported in Table 5.1.

Table 5.1: Optimal snow and ice melt parameters from calibration. DDS and DDI are the degree day factors for now and ice respectively, TF and SRF the temperature and solar radiation factors for the hybrid model.

Parameter	Value	Range	Method
DDS [mm/d°C]	6	2 -10	Calibrated
DDI [mm/d°C]	7	2 -10	Calculated
TF [mm/d°C]	0.208	0.02-0.3	Calibrated
SRF [mm m^2/dW]	0.00029	0.0002-0.02	Calibrated
Threshold melt [°C]	-5	-	Calibrated

Correctly, the calibrated DDS results smaller than the calculated DDI. Indeed, ice is characterized by lower surface reflectivity, thereby more energy is available for melting.

Further, heat fluxes over snow are reduced to the lower roughness length of snow if compared with ice (Konz 2009).

With respect to the degree day method, the hybrid model predicts less accurately the snow depth, particularly in the depletion periods; nonetheless, the simulation is acceptable. The cumulated snow on the ground is slightly overestimated, but more importantly, the hybrid model predicts longer snow cover on the ground, thereby preventing ice from melting, which could lead to misrepresent the glacier state. Thus, the degree day method is chosen to simulate at the rougher scale.

The hybrid approach is likely limited by the requirements of albedo and shortwave radiation as inputs, for three reasons. First, it is not possible to evaluate albedo from ground cover nor distribute solar radiation over the study area accounting for topographical influence such as shadowing, because of the coarse dimension of the model cells. Secondly, given the aforementioned limit, albedo variation in time is computed from observations, but only at Pyramid AWS due to the lack of sufficient information at other locations and thereafter applied to each cell; however, cells may not be covered by snow at the same time as Pyramid's one, so that albedo is not representative. Finally, differential cloud cover over the quite wide study area might affect the representativeness of radiation and albedo observations at Pyramid for the whole catchment. In conclusion, the simpler temperature index model is preferred to predict snow and ice melt at this spatial resolution.

Noticeably, it is acknowledged that these models require the choice of a correct temperature threshold, which is the major uncertainty source in the computation of snow melt (see e.g. Senese et al. (2014)). In fact, melt does not necessarily occur at daily air temperatures higher than 273.15 K, as already discussed in Paragraph 3.1.1; therefore, the threshold temperature for activating melting has to be set in order to best adapt predictions to the observed occurring melt. For both the temperature index and hybrid model, a threshold temperature of $-5°\ C$ permits the most reliable reconstruction of snow melt; similar results are obtained by Senese et al. (2014).

Finally, as the snow melt module here is calibrated at a single location in the study area, it is interesting to evaluate its performance in simulating the snow cover extent over time. Thus, in Paragraph 6.1 the simulated spatial snow cover extent is compared with satellite observations.

5.2.2 Hydrological parameters

This section presents the model results in terms of predicted discharge over the calibration and validation periods. The observed and simulated hydrographs are compared, and the mean monthly discharges are analysed as further information; efficiency indexes are calculated to support the analysis with objective criteria. The outcomes from two different inputs datasets are also discussed. First, input gridsets are constructed by validating satellite data with ground stations observations as detailed in Paragraphs 4.1.3.2 and 4.2.3. Secondly, the model is run using input climatic variables observed at the ground stations and spatially distributed by means of lapse rates, as explained in Paragraphs 4.1.3.1 and 4.2.3.1.

5.2.2.1 Model calibration

Calibration is performed by visual inspection of the hydrographs (Figure 5.5), control on monthly discharge and maximization of efficiency indexes (Figures 5.6 and 5.7). Table 5.2 reports the calibrated values of the model parameters.

Table 5.2: Calibrated values for the hydrological parameters.

Parameter	Value	Range
Groundwater flow exponent [-]	1.5	0.5 - 1.5
Saturated conductivity [mm/d]	1.7	0.1 - 4.0
Surface reservoirs lag time [h]	180	-
Ground reservoirs lag time [h]	2000	-
Number of surface reservoirs [-]	3	-
Number of ground reservoirs [-]	3	-

This set of parameters is calibrated over the assimilated satellite- and ground stations dataset. Noticeably, very high values for the lag times are found to best fit the observed hydrograph. This is likely due to the fact that no base flow is included in the model, thus lag times result to be higher in an attempt to reproduce that constant component.

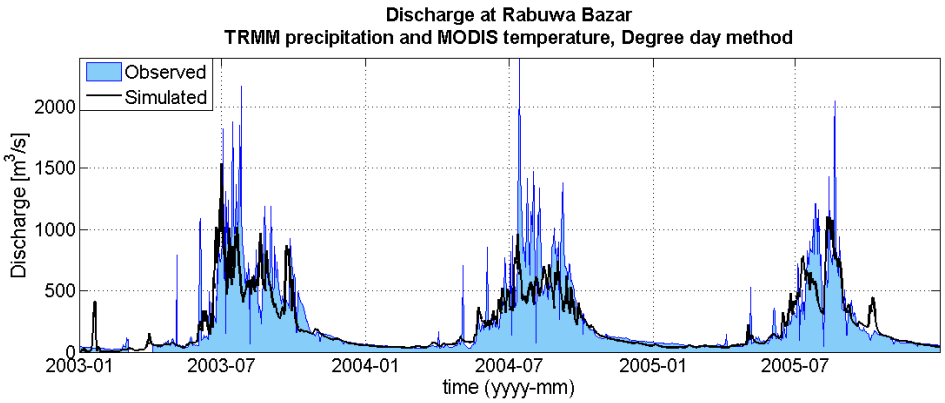

(a) Satellite data as input

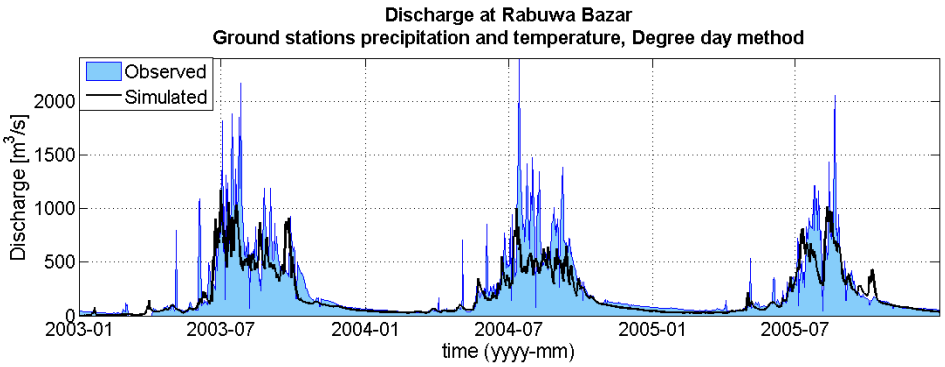

(b) Ground data as input

Figure 5.5: Calibration of the hydrological model run with the two different input datasets. The degree day method is used for the melt module.

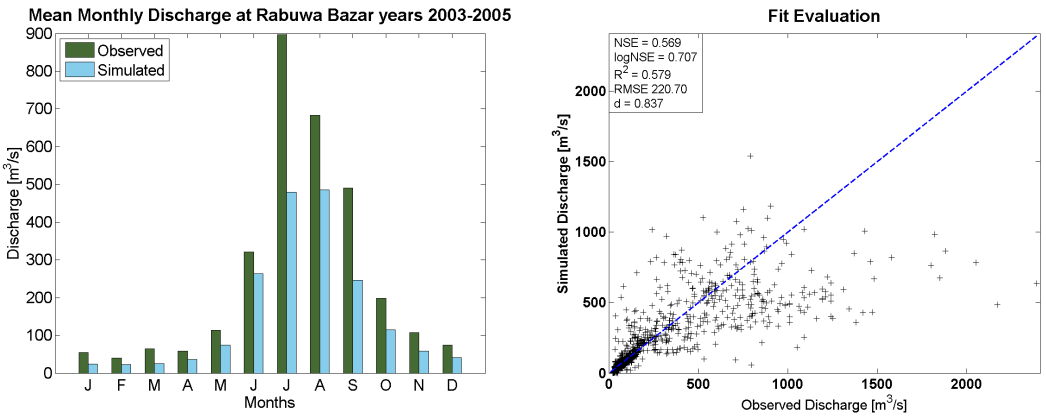

Figure 5.6: Monthly mean discharge and model efficiency for the calibration period. Satellite data as input.

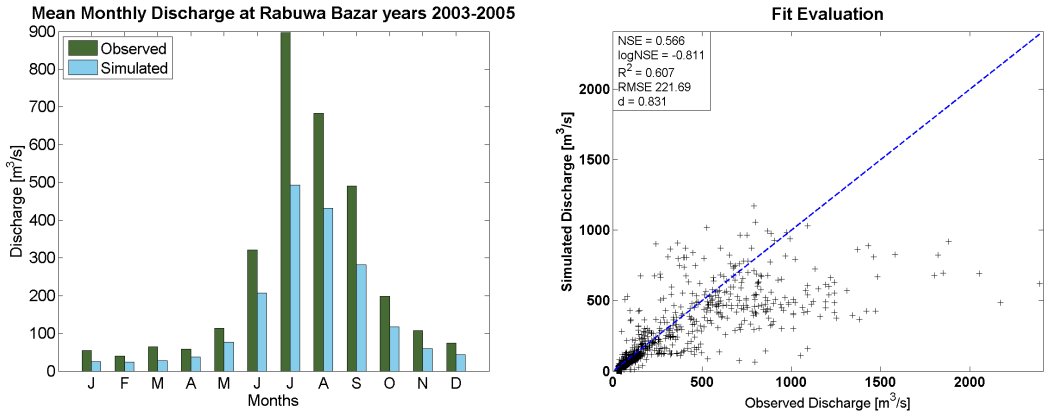

Figure 5.7: Monthly mean discharge and model efficiency for the calibration period. Ground data as input.

5.2.2.2 Model validation

The model is run with the same set of parameters over the validation period. Figure 5.8 presents the hydrographs, while Figures 5.9 and 5.10 show the monthly discharge in the validation period along with the efficiency indexes. Coherently with calibration analysis, discharge is compared between observed and simulated series, as well as between simulations based on satellite and ground stations input data.

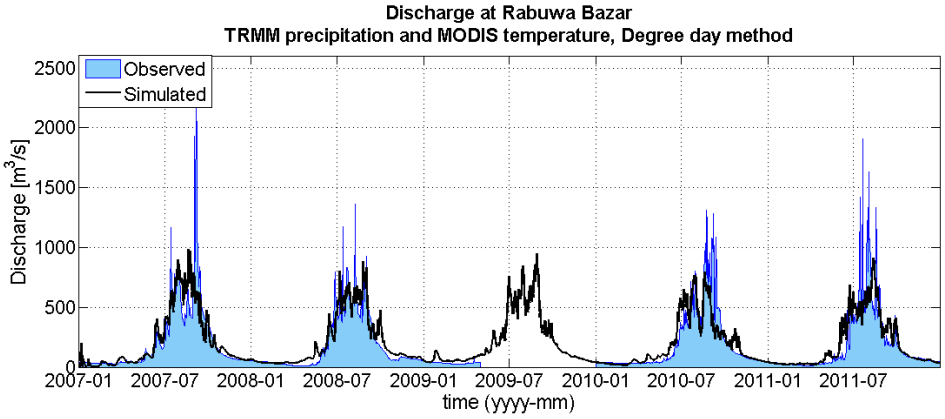

(a) Satellite data as input

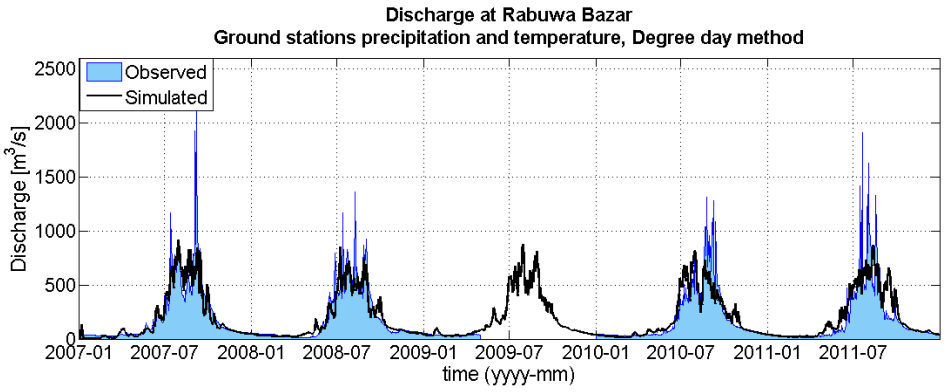

(b) Ground station data as input

Figure 5.8: Validation of the hydrological model run with the two different input datasets. The degree day method is used for the melt module.

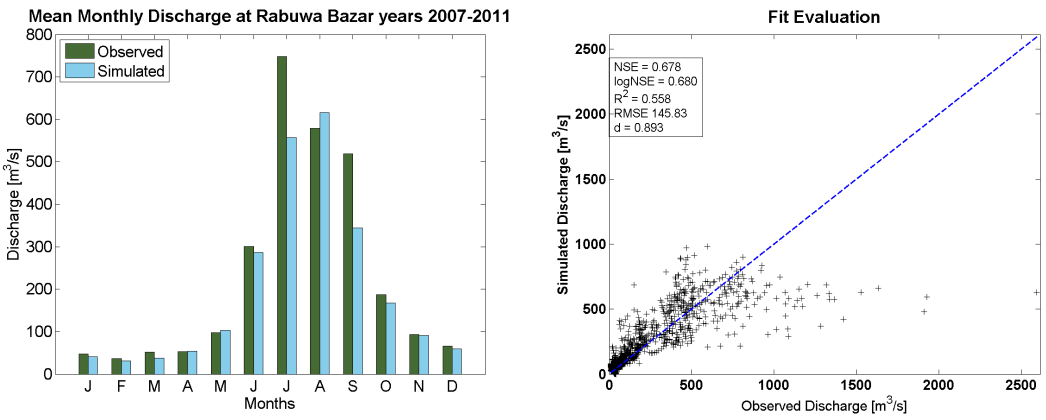

Figure 5.9: Monthly mean discharge and model efficiency for the validation period. Satellite data as input.

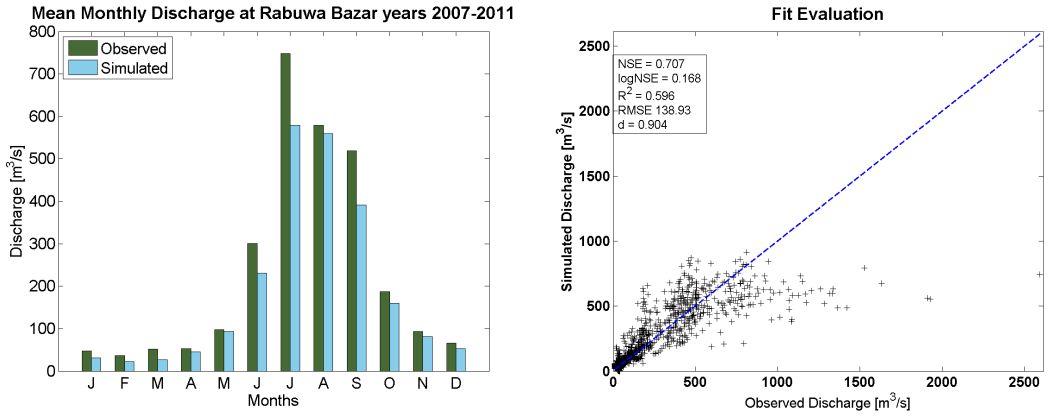

Figure 5.10: Monthly mean discharge and model efficiency for the validation period. Ground data as input.

5.2.2.3 Hydrograph analysis

Figures 5.5 and 5.8 illustrate the ability of the model to simulate discharge time series at Rabuwa Bazar. Model's performance appears to be comparable for calibration and validation, suggesting that parameters are not overly fitted on the calibration period. Further, Figures 5.5 and 5.8 show that the choice of the input does not determine substantial differences in the simulated discharge. Indeed, all the simulations display similar merits and issues in reproducing the observed hydrograph, as discussed in the following.

First of all, the model appears to be unable to simulate the peaks discharge with both satellite and ground data, especially those larger than 1000 m^3/s. However, it should be considered that high discharge values are affected by larger uncertainties than low ones because the stage-rating-curve may be based on an inadequate number of measurements. Nepal (2012) reports that the rating curve for the Dudh Kosi river at Rabuwa Bazar is calculated based on a few measurements during low flow periods (in the range of 30-600 m^3/s), and any higher value is normally estimated by the extrapolation. Therefore, there is high confidence in the lower values of discharge and uncertainty is greater for higher values.

Conversely, low flows are fairly well reproduced; in particular, simulating with satellite data as input seems to return better agreement with the observations. Post monsoon discharge is occasionally over estimated, as the model tends to predict larger discharge peaks than observed in the descendant part of the hydrograph.

Premonsoonal floods are generally detected in time, with good agreement in more than half of the years (2004, 2005, 2007, 2008, 2010), even though the peak discharge is at

times underestimated (2004, 2005). The bulk discharge during the monsoon period and seasonal changes are fairly well reproduced (especially in 2003, 2008, 2010). Further, the model appears to capture the quick variations in premonsoonal and monsoonal discharge, even though it fails in reproducing the peak values.

This issue has to be taken into account in case the model is used for real time flood forecast; indeed, rapid flow surges and decreases are simulated with few false and missing predictions, but the magnitude of the peak flood is generally not satisfactorily simulated. The performance of this model against the previously implemented altitude belts approach (Paramithiotti 2013) is discussed in Paragraph 6.3.

Finally, mean monthly discharges are analysed as support to the hydrograph analysis, to better understand the impact of model underpredictions of flood events. In the calibration period (Figures 5.6 and 5.7) it is observed a general underestimation of the river flow throughout the year, since the peaks in discharge are not captured (Figure 5.5). On the other hand, during the validation period, mean monthly discharge indicates good agreement between simulations and observations. This is due to the fact that during validation years, no rapid surge of discharge occurs during the pre- and post-monsoonal seasons, and far less are observed during the monsoon. As anticipated, the satellite data driven model (Figure 5.9) displays better performance during winter months if compared with simulations from ground data (Figure 5.10). The monsoonal season appears to be the most critical to be simulated, as discharge is underestimated in July and September and overestimated in August. This issue might result from insufficient representation of monsoonal rainfall and seasonal melting patterns. In the former case, a higher resolution satellite products for spatial distribution of rainfall should help in correctly simulate monthly discharge, while the latter cause might be addressed, at this rough spatial scale, by studying infra-annual variability of degree day factors. Paragraph 6.4 will deepen the impact of these elements by analysing the different contributions to the total discharge. In addition, great uncertainties on soil water content may be responsible of the inaccurate peak discharge estimations. Future work might study the influence of this variable on the simulated discharge, and ideally field data will be collected to support the analysis.

5.2.2.4 Goodness of fit evaluation

Model performance is also assessed by means of numerical indexes measuring the efficiency and the error of the simulation. Table 5.3 summarizes these indicators for the calibration and validation periods, both run with satellite and ground data as input, alternatively.

Table 5.3: Model efficiency and error for the calibration and validation periods; comparison between the input datasets is also provided.

	Calibration period		**Validation period**	
Index	**Satellite data**	**Ground data**	**Satellite data**	**Ground data**
NSE	0.57	0.57	0.68	0.71
logNSE	0.71	-0.81	0.68	0.17
R^2	0.58	0.61	0.56	0.60
RMSE	220.7	221.7	145.8	138.9
d	0.84	0.83	0.89	0.90

To begin with, the Nash-Sutcliffe Efficiency coefficient is quite low for all simulations, confirming that high flows are not completely resolved by the model; it results being higher for validations probably because the peaks are less pronounced in that period.

The fact that low flows are better simulated by satellite based inputs is evident in the values of the logarithmic Nash-Sutcliffe Efficiency, which turns out to be negative, thus unacceptable, for simulations run on ground stations data. On the contrary, it performs quite well for satellite-driven simulations, being close to unity.

R^2 coefficient does not vary significantly within the simulations, indicating that the results are equally dispersed around the observations. The root mean square error appears to be quite high, as expected given the large difference between peak values and corresponding predictions; however, the index of agreement d, close to unity, suggests that model errors are limited if compared to the potential error.

5.2.2.5 Input dataset choice

In addition to assessing the overall model performance, the influence of input data is also examined in this study. As shown in previous paragraphs, no outstanding difference is evident between the two input datasets. Still, satellite data better describe the low flows, likely because of a more realistic distribution of temperatures is possible with MODIS scenes, not depending on altitude alone; indeed, as it will be shown in Paragraoh 6.4, low flows are mainly constituted of melt water. Moreover, monsoonal flows are more accurately predicted if satellite input data are used (e.g. Figure 5.8), as spatial variability of rainfall is better captured. However, no relevant improvement in model performances is observed (Table 5.3), probably because the spatial resolution of satellite scenes is still coarse compared to the rate of spatial variability of rainfall in such an orographically complex area. Moreover, soil water content might be a key factor in simulating discharge peaks, even more than rainfall spatial distribution. Additionally, it is possible that the choice of model parameters has a stronger influence on the performance than that of

the input dataset, so that good calibrated parameter sets outweigh the better input distribution. Further analysis should investigate whether this is the case.

To sum up, model performances are generally satisfactory, apart from the inability in predicting flood peaks values; however, flood occurrence is at times detected. Further, from hydrograph analysis it comes out that predictions are more accurate if the model is driven by long term averages of remotely sensed climatic variables, adjusted to ground observations, rather than solely by ground observations distributed depending on elevation. However, the coarse spatial resolution of satellite data and the uncertainties in modelling water storage in the soil are still limiting.

5.3 Smaller-catchment calibration

The hydro−glaciological model presented in Section 3.2 is run on the catchment closed at Periche (151.83 km^2) at 300 m horizontal resolution. The driving input dataset is made of precipitation, temperature ad solar radiation observed at ground stations and spatially distributed by means of lapse rates (precipitation, temperature) and topography retrieved from the Digital Elevation Model (radiation). The model simulates flow generation and cryospherical processes such as discharge along the river, snow cover and melt, ice ablation for clean ice and under debris cover, glacier dynamics and flow routing through soil, ice and snow.

The hydrological parameters are calibrated from the discharge time series observed at Periche; thus, simulation periods are limited to those in which discharge records are available, three years so far. Calibration is performed over the year 2011, whereas 2012 and 2013 are used to validate the model. As previously discussed (see Paragraph

Paragraph 5.3.1 illustrates the snow melt parameters calibration and validation, while the ice melt model is treated in Paragraph 5.3.2. Afterwards, the hydrological parameters are optimized and model performance is assessed in terms of ability to reproduce the hydrograph and monthly averages and efficiency indexes (Paragraph 5.3.3). Finally, the parameters for the glacier dynamics model are optimized (Paragraph 5.3.4).

5.3.1 Snow melt parameters calibration

The two parameters of the hybrid model for snow melt are calibrated with the observed snow depth series at Pyramid AWS, being the sole snow gauge in the basin. Figure 5.11 shows the snow depth and cumulative time series used for calibration, while the

validation period is shown in Figure 5.12. Table 5.4 summarizes the calibrated values for the parameters.

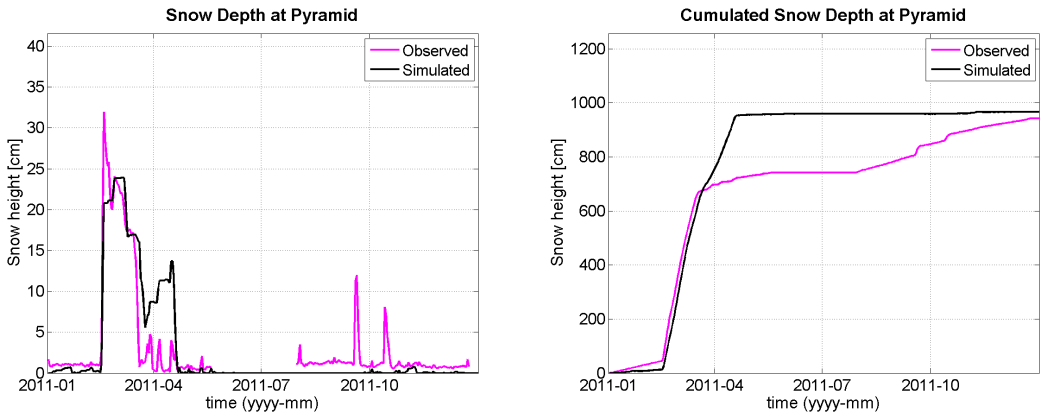

Figure 5.11: Calibration of the hybrid model parameters for snow: observed and simulated time series of snow depth(left) and cumulative snow height (right) at Pyramid AWS.

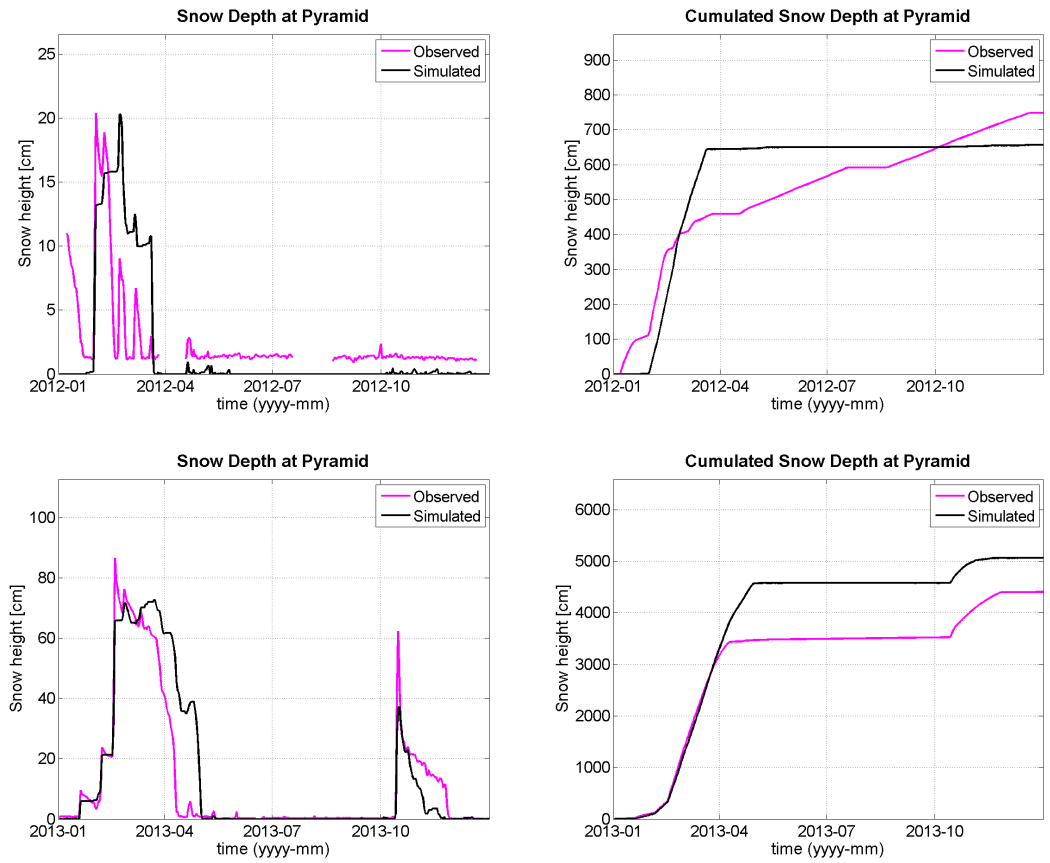

Figure 5.12: Validation of the hybrid model parameters for snow: observed and simulated time series of snow depth(left) and cumulative snow height (right) at Pyramid AWS. The charts at top show year 2012, those at bottom year 2013.

Table 5.4: Optimal snow melt parameters from calibration. DDS is the snow degree day factor, RF_{snow} the solar radiation factor.

Parameter	Value	Range	Method
DDS [mm/d°C]	4	2 - 10	Calibrated
RF_{snow} [mm m^2/dW]	2.0×10^{-7}	0.0002-0.02	Calibrated
Threshold melt [°C]	-5	-	Calibrated

The hybrid model appears to properly fit the observed snow depth series; only in the monsoonal season, it fails in simulating the snow cover at Pyramid (2011 and 2012) or underestimate the snow water equivalent (2013). It has to be noticed that the snow depth records for 2011 and 2012 are retrieved from a different sensor than previous years and 2013; even though no data quality information is provided, it is possible that systematic errors affect the measurements, since the recorded snow depth never falls to zero.

As can be seen in Table 5.4, the radiation factor best suiting the observation is very small, indicating that temperature plays a major role in governing snow melt at Pyramid. A second snow gauge would allow for checking whether this holds at different locations and altitudes in the study area. Another parameters regulating snow melt is the fresh snow density, which has been observed to be 210 kg/m^3 at Pyramid (Paragraph 4.3.1); however, it would be optimal to derive fresh snow density from multiple observations, ideally at different altitudes in the catchment.

5.3.2 Ice melt parameters calibration

The hybrid model parameters for ice melt are partly estimated from ice ablation measurements by means of stakes on the glacier, and partly calibrated from the hydrograph volumes. Indeed, it is possible to estimate the degree day (or temperature) factor from clean ice thickness variations at the stakes (Paragraph 4.4) as temperature records are available near survey locations during the stakes observation period (May−October 2014). On the contrary, radiation observations display an instrumental drift and are thus not deemed reliable. Therefore, the radiation factor is calibrated adjusting the ice melt volumes to the observed volumes flowing at Periche. Figure 5.13 show the volume comparison for the calibration and validation periods. Year 2013 is not included in the analysis as significant parts of observed data are missing. Also the last two months of 2012 discharge are missing, thus have been deleted from the simulation series as well. Table 5.5 summarizes the optimal parameters for snow melt.

By comparing the observed and simulated volumes, it emerges that the hybrid model efficiently represents the melt processes in the study area. Further, the degree day factor

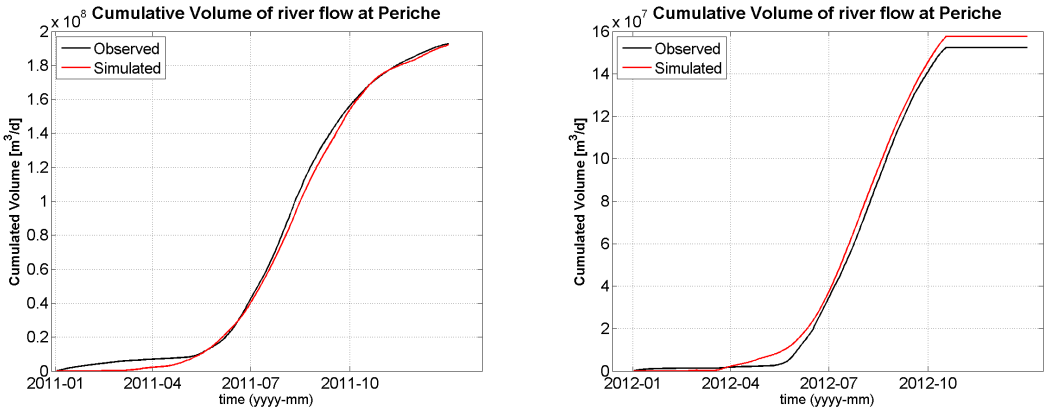

Figure 5.13: Comparison of observed and simulated volumes at Periche during the calibration (left) and validation (right) periods for optimizing the radiation parameters for ice melt. Last two months of 2012 are missing.

Table 5.5: Optimal ice melt parameters from calibration. DDI is the ice degree day factor, RF_{ice} the solar radiation factor.

Parameter	Value	Range	Method
DDI [mm/d°C]	6.5	2 - 10	Estimated
RF_{ice} [mm m^2/dW]	1.0×10^{-4}	0.0002-0.02	Calibrated
Threshold melt [°C]	-5	-	Calibrated

computed from ablation at stakes permits a consistent representation of ice melt. As for snow melt, the temperature threshold above which ice melt occurs is set to $-5°$, since it allows the best simulation of melting; this choice has already been discussed in Paragraph 5.2.1.

5.3.3 Hydrological parameters

As discussed in Paragraph 3.2.4, in a highly glacierized catchment it is relevant to model the water flow thorugh snow and ice, in addition to the surface and ground water flows. The runoff generated at each cell is routed to the outlet through one of those systems, each consisting of a fast and a slow linear cascade of reservoirs. Number of reservoirs and lag times are calibrated for each means (6 parameters). Further, two coefficients for fast and slow flows partitioning are necessary for the snow and ice system (2 parameters), whereas for soil, runoff and infiltration are separated according to eq. (3.15) (2 parameters). Calibrating ten parameters on a single discharge time series returns several combinations of parameters fitting the observations equally well. Thus, the simulated discharge is decomposed in its contributions from soil, snow and ice, and

the parameters of each means are calibrated on the time interval in which each means dominates the runoff.

In the following, the results from calibration and validation are presented (Paragraphs 5.3.3.1 and 5.3.3.2) and discussed, in terms of hydrographs comparison (Paragraph 5.3.3.3) and efficiency indexes (Paragraph 5.3.3.5).

5.3.3.1 Model calibration

Calibration is performed by visual inspection of the hydrographs (Figure 5.14), control on monthly discharge and maximization of efficiency indexes (Figure 5.15). Table 5.6 reports the calibrated values of model parameters. Noticeably, both ice and snow yield low shares of fast flow (0.1 for both); lag times are quite high probably for compensating the lack of a base flow component, as discussed in Paragraph 5.2.2.

Table 5.6: Calibrated values for the hydrological parameters.

	Parameter	Value	Range
Soil	Groundwater flow exponent [-]	1.2	0.5 - 1.5
	Saturated conductivity [mm/d]	4	0.1 - 4
	Surface reservoirs lag time [h]	75	-
	Ground reservoirs lag time [h]	420	-
Snow	Fast flow share [-]	0.1	0 - 1
	Fast reservoirs lag time [h]	250	-
	Slow reservoirs lag time [h]	1450	-
Ice	Fast flow share [-]	0.1	0 - 1
	Fast reservoirs lag time [h]	50	-
	Slow reservoirs lag time [h]	850	-

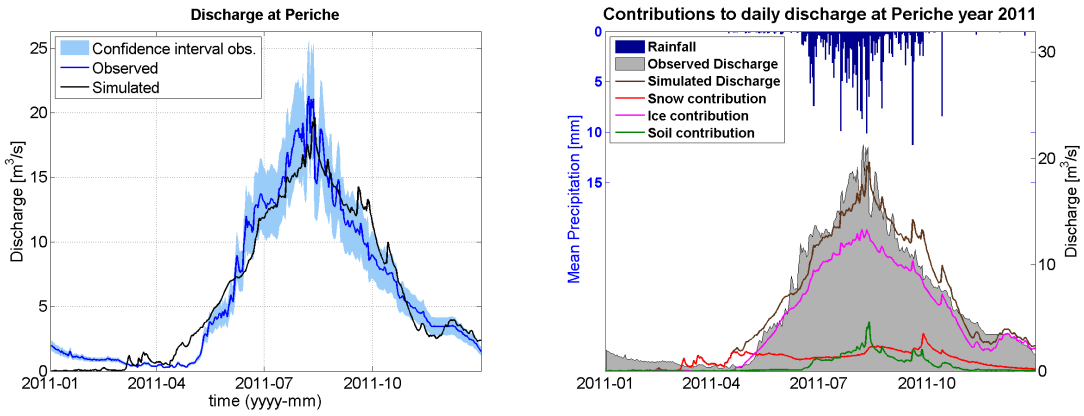

Figure 5.14: Calibration of the hydrological model. The best fitting hydrograph is shown (left) along with the contributions time series used to identify the time spans where to optimize the different parameters.

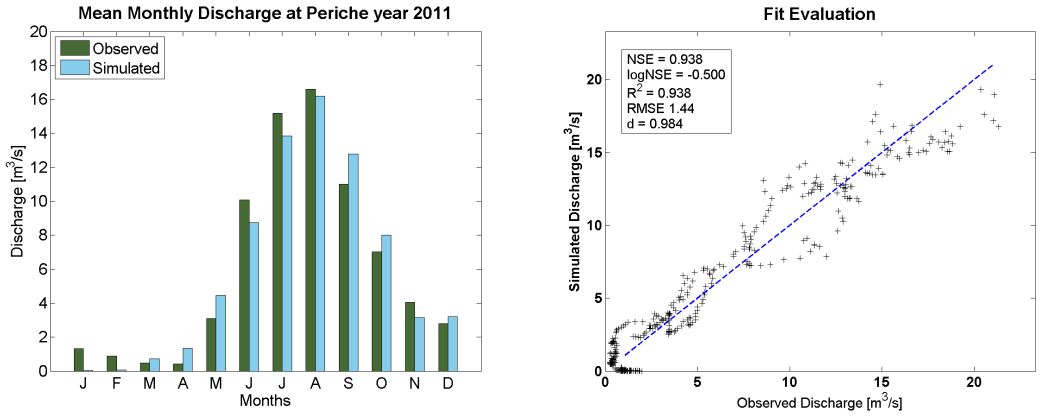

Figure 5.15: Monthly mean discharge and model efficiency for the calibration period.

5.3.3.2 Model validation

The model is run with the same set of parameters over the second part of observed discharge for validating the optimality of the parameters. Figure 5.16 presents the hydrographs, while Figure 5.17 shows the monthly discharge in the validation period along with the efficiency indexes. Validation is mainly performed over year 2012, as large parts of observed discharge in 2013 are missing. However, given the data scarcity, it is interesting to see how the model performs in one additional year (Figures 5.18 and 5.19).

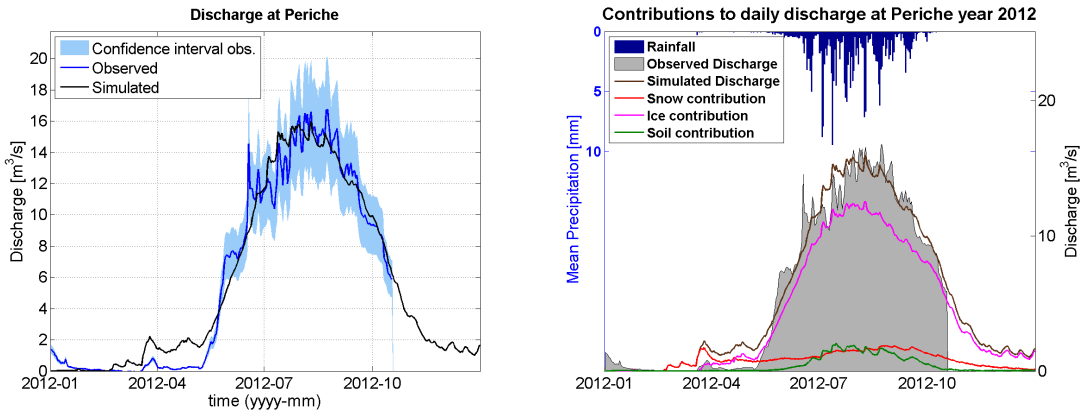

Figure 5.16: Validation of the hydrological model (year 2012). The best fitting hydrograph is shown (left) along with the contributions time series used to identify the time spans where to optimize the different parameters.

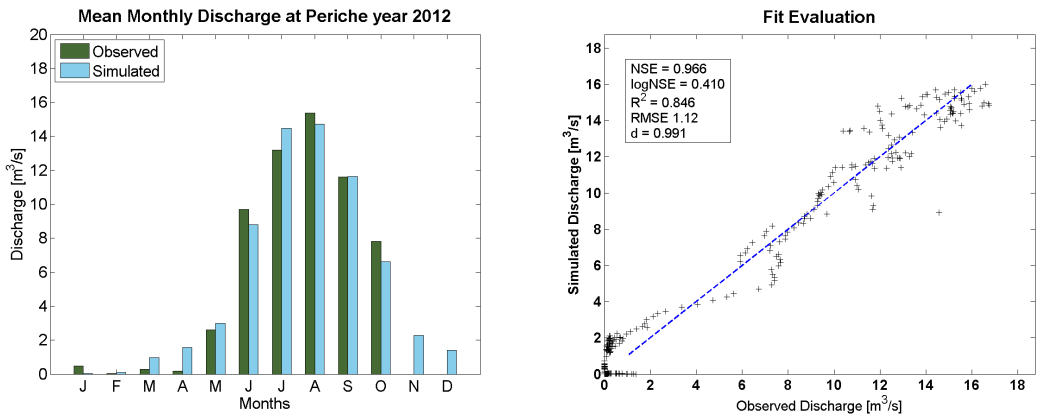

Figure 5.17: Monthly mean discharge and model efficiency for the validation period.

5.3.3.3 Hydrograph analysis

A fairly good agreement is obtained between simulated and observed daily discharge. Generally, the seasonal behaviour is reproduced, as well as the seasonal magnitude of the river flow. The most difficult processes to be reproduced seem to be the early snow melt during the pre monsoonal season and the response to rainfall events in the post monsoonal season. Comparison of modelled and observed mean monthly discharge confirms this statement, as the high flows periods are better reproduced in the simulation.

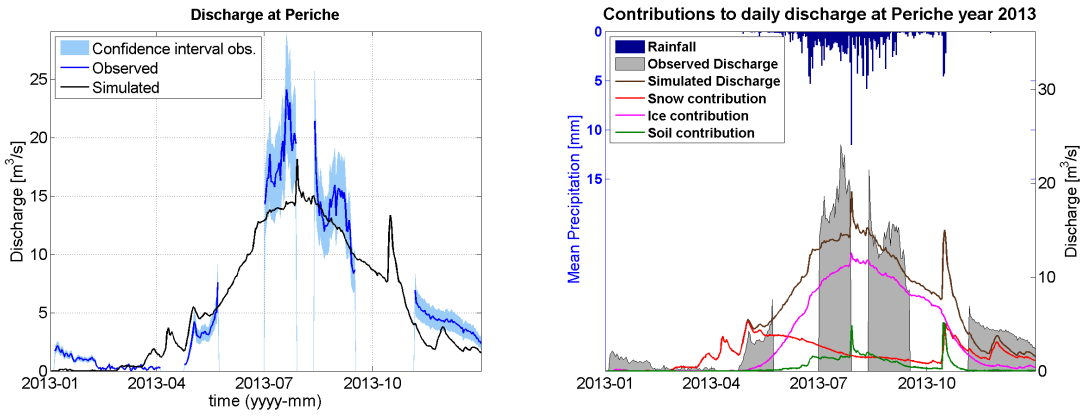

Figure 5.18: Further validation of the hydrological model (year 2013). The best fitting hydrograph is shown (left) along with the contributions time series used to identify the time spans where to optimize the different parameters.

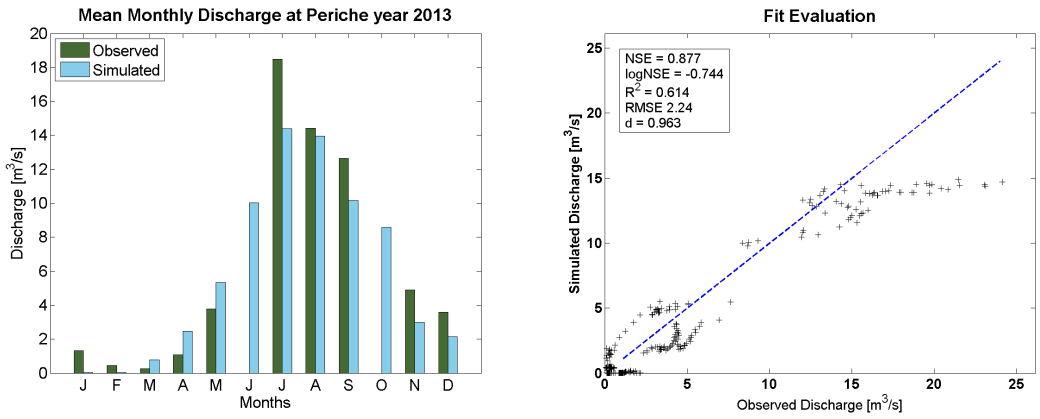

Figure 5.19: Monthly mean discharge and model efficiency for the validation period.

Snow−related route flow parameters are mainly calibrated during the pre monsoonal rising limb, as it appears to be the main contribution to river flow. For the rest of the year, snow melt and rainfall conveyed through the snow reservoirs provide an almost constant term, as a sort of base flow; indeed, calibrated lag times for snow reservoirs are very high. After the snow ones, the ice route flow parameters are calibrated, based on the descending limb of hydrograph; indeed, during late autumn and winter precipitation is almost absent and also the snow cover is limited. Another period where ice dominates the river flow is the late pre monsoonal season. Calibration of these periods yields better results than that of snow route flow parameters, probably due to the large uncertainties affecting snowfall simulations that will be discussed in the following. Finally, soil route flow parameters are optimized. Their influence is dominant in determining the peaks during the monsoonal season (see e.g. Figure 5.14); however, the discharge magnitude

is dependent on the ice melt parameters (Paragrpah 5.3.2).

In 2011 and 2013 the high flows appear to be underestimated, and by dedicated analysis it resulted being related to low radiation intake; however, model parameters were not modified not to worsen the simulation of 2012, when the discharge is overestimated in the late pre monsoonal season. The sudden increase in discharge in July, 2013 is due to the contemporary occurrence of heavy rainfall and an increasing trend in radiation observed at Kala Patthar. The post monsoonal peak show the system response to heavy rainfalls, but as observed discharge steadily decrease, it is likely that convective rainfall occurred on a limited part of the basin. This analysis points out the need for a more extended gauging network, in order to record spatial variability of radiation and precipitations, which are likely to vary over a 150 km^2 wide catchment. The post monsoonal discharge peak in 2013, on the other hand, corresponds to an exceptionally high snowfall event at Pyramid. It is not known whether the event hit the whole catchment, as no other snow depth gauge is present and discharge observations are missing.

A global sensitivity analysis may be useful to study the complex interactions between the parameters; however, a more complete flow routing model could also be developed in order to account for the flow exchanges between soil, ice and snow reservoirs, enhancing the accuracy of the physical representation of the catchment.

5.3.3.4 Uncertainties and Limitations

It must be remarked that the observed discharge at Periche is affected by uncertainties deriving from interpolating the rating curve on only four discharge measurements, and from the small magnitude of recorded levels. Indeed, during low flows, river stage amounts to few centimetres, so that measured values are comparable with the magnitude of measurement errors; thus, discharge time series are provided with $\pm 20\%$ confidence intervals. Nonetheless, the discharge series at Periche is an extremely valuable dataset, as it exceptionally allows for focussing the hydrological modelling on a large glacierized, high altitude catchment.

Model performance is partly limited by missing rainfall observations in multiple AWSs at the same time and by uncertainties in snow depth measurements. The first issue is evident in the first half of 2012, when several months of rainfall data are missing from Periche and at times from Pyramid as well. Thus, it was necessary to perform a simple form of gap filling (see Paragraph 4.2.1.1 for details), which yielded rainfall time series having little amounts of rainfall in consecutive days; as a consequence, the simulated hydrograph appears to be smooth. The reason why rainfall gap filling performed worse than usual is that during these months, no rainfall is recorded at Kala Patthar, which

would have been necessary to discriminate between rainy and dry days. The second issue is the likely due to the existence of an instrumental drift in the snow depth sensor at Pyramid in 2011 and 2012 (see Paragraph 5.3.1), even though no information on data validation is available. Errors in snow depth measurements affect the precipitation totals as positive daily snow depth variations are used to correct the rainfall amounts at high altitudes, as explained in Paragraph 4.3.3.

Finally, by simulating on a single year, model performance cannot be tested in January, as the effect of the initial conditions is still present, notwithstanding the choice of beginning the simulation in a low flow, limited snow covered period to minimize this issue. Indeed, very high lag times for snow related flow routing sensibly delay the runoff, and discharge in the beginning of the simulation period cannot benefit from previous months' contributions. Anyway, acquiring more data as time passes, it will be possible to carry out longer simulations and this problem will disappear.

5.3.3.5 Goodness of fit evaluation

Table 5.7 shows the values of the model error and efficiency indexes as an objective indication of the goodness of fit discussed by visual inspection of the hydrograph. Given the amount of missing data, year 2013 is not deemed representative in testing model performance and thus it is excluded from the analysis.

Table 5.7: Summary of efficiency indexes and model error for the calibration and validation periods.

Index	Calibration (2011)	Validation (2012)
NSE	0.938	0.966
logNSE	-0.500	0.410
R^2	0.938	0.846
RMSE	1.44	1.12
d	0.984	0.991

First of all, the model performs similarly during the calibration and validation periods, indicating that parameters are not overly fitted over the calibration dataset. Efficiency indexes confirm that high flows are better simulated than low ones. Indeed, values close to the unity are obtained for the NSE and d coefficients, whereas the logarithmic Nash−Sutcliffe Efficiency display much lower values; in particular, during the calibration period it results to be negative. There are several reasons behind this behaviour. First, low flows are often not detected in the beginning of the simulation as a consequence of the aforementioned effects of initial conditions. Secondly, low flows are overestimated in the pre monsoonal, snow−melt−dominated season and this is likely related to the

uncertainties in precipitation amounts as previously discussed. Finally, low flows observations themselves are affected by high uncertainties related to the measurements. These considerations confirm the previous discussion from hydrographs visual analysis.

Remarkably, the hydro−glaciological model run on the catchment closed at Periche yields better results in terms of discharge simulation than the model run on the wider catchment closed at Rabuwa Bazar, showing the potential of a detailed and yet conceptual hydro−glaciological modelling of high altitude basins.

5.3.4 Glacier dynamics parameters calibration

Glacier dynamics is reproduced by means of a conceptual model based on Weertman's equation computing ice velocities from basal shear stress, as illustrated in Paragraph 3.2.3. There are two parameters to be calibrated, being the roughness of the bedrock ν and the material roughness R coefficients; actually, from eq. (3.23) it is evident that the product $\nu^2 \times R$ can be calibrated. Observed velocities from stakes positioning at different epochs (see Paragraph 6.7) are available at five locations in the upper part of the Khumbu glacier, and are used to calibrate the glacier dynamics parameters by minimizing the root mean square error. Figure 5.20 shows the simulated ice velocities at stakes locations against the observations.

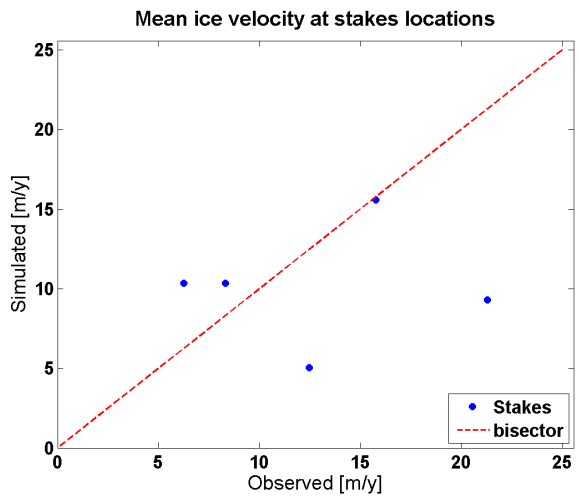

Figure 5.20: Mean simulated ice velocities at stakes locations against observed values. Ice velocities are intended as averages over the vertical profile of the ice section.

Noticeably, observed surface velocities have been reduced to averages over the vertical profile in order to be compared with the outcomes of the simulation. The results corresponding to the minimum−square−error parameters show very good agreement at one stake and either over− or underestimation at the other stakes. It should be considered,

however, that punctual measurements are being compared with averages over 300 m $\times$ 300 m cells in a region characterized by great spatial variability over small distances; further discussion is provided in Paragraph 6.7.

Chapter 6

Discussion

This Chapter deepens some simulation features that are deemed interesting for understanding the hydrological and cryosphere−related processes in the catchment, and for assessing model performance. The intention is to show model achievements in describing the hydrology of a high altitude glacierised catchment, along with its limitations and uncertainty sources.

First, the ability of the coarser−resolution hydrological model in simulating the snow cover extent and the rainfall spatial distribution is tested by comparing model predictions with long term average satellite observations from MODIS and TRMM respectively (Paragraphs 6.1 and 6.2). Then, simulated discharge is compared with that of the previously adopted altitude belts based model, in order to show the improvements in the discharge simulation at Rabuwa Bazar (Paragraph 6.3). Paragraph 6.4 discusses the contributions to river flow from rainfall, snow and ice melt both at Rabuwa Bazar and Periche, analysing the seasonal variations and suggesting possible future impacts. Paragraph 6.5 the discharge series simulated at Periche by the two models at different spatial resolution. Afterwards, Paragraph 6.6 analyses the model performance in simulating debris thicknesses and ice melt, discussing the uncertainties affecting the model; furthermore, the spatial distribution of ice melt during the year is shown as relevant outcome. Finally, the ice velocity map resulting from the glacier dynamics model is discussed and compared with previous works (Paragraph 6.7).

6.1 Spatial snow cover extent

The snow melt module is calibrated over the local snow depth time series observed at Pyramid AWS. Here, it is also tested for its ability to reproduce the extension of snow

cover over time. For this purpose, the simulated snow water equivalent is compared with the MODIS snow cover product. Given the monthly resolution of satellite data, the comparison is carried out between the mean monthly snow depth at each cell and the mean monthly snow cover retrieved from MODIS Aqua and Terra satellites, expressed in percentage of time each cell is occupied by snow. Indeed, it is assumed that higher monthly mean snow depths should correspond to more frequently snow covered areas. Figures 6.1 and 6.2 illustrate this comparison over the calibration period $2003 - 205$, using the degree day method to compute snow melt.

As it can be observed in Figures 6.1 and 6.2, the snow cover extent is accurately simulated, at least in terms of monthly means. Only, the model does not reproduce snow cover for May, July, August and September in the lower part of the catchment. However, since snow cover at low altitudes is unlikely present in those months and no quality information is available for MODIS scenes, it cannot be assumed that satellite data always correctly represent the phenomenon. Remarkably, the snow cover extent in January and December is as little as in June, during the melting season; this probably has to be ascribed to the scarcity of precipitation during winter months. Bajracharya & Uddin (2010) report that seasonal changes in snow cover are quite significant, but so far no study has been carried out over a longer period of time to establish whether this is also an impact of global climate change.

Finally, permanent snow is simulated above 5700 m a.s.l., whereas MODIS does not detect snow on the northern ridges in the basin. This could be due to the steep topography, as Nagler et al. (2008) observed MODIS fractional snow maps being affected by topographic noise on steep slopes if compared with the higher resolution snow maps of the Advanced Spaceborne Thermal Emission and Reflection Radiometer (ASTER). Figure 6.3 shows the permanent snow cover derived from ASTER, lastly updated to 2006[1].

Evidently, the simulated and the ASTER datasets show good agreement in the northern part of the catchment, whereas the model fails at capturing permanent snow cover in the central crests. Indeed, in those areas, only seasonal snow cover (January−May and September−November) is replicated.

[1] Available at http://geoportal.icimod.org/indusbasin/Downloads/ [Accessed 10th November 2014].

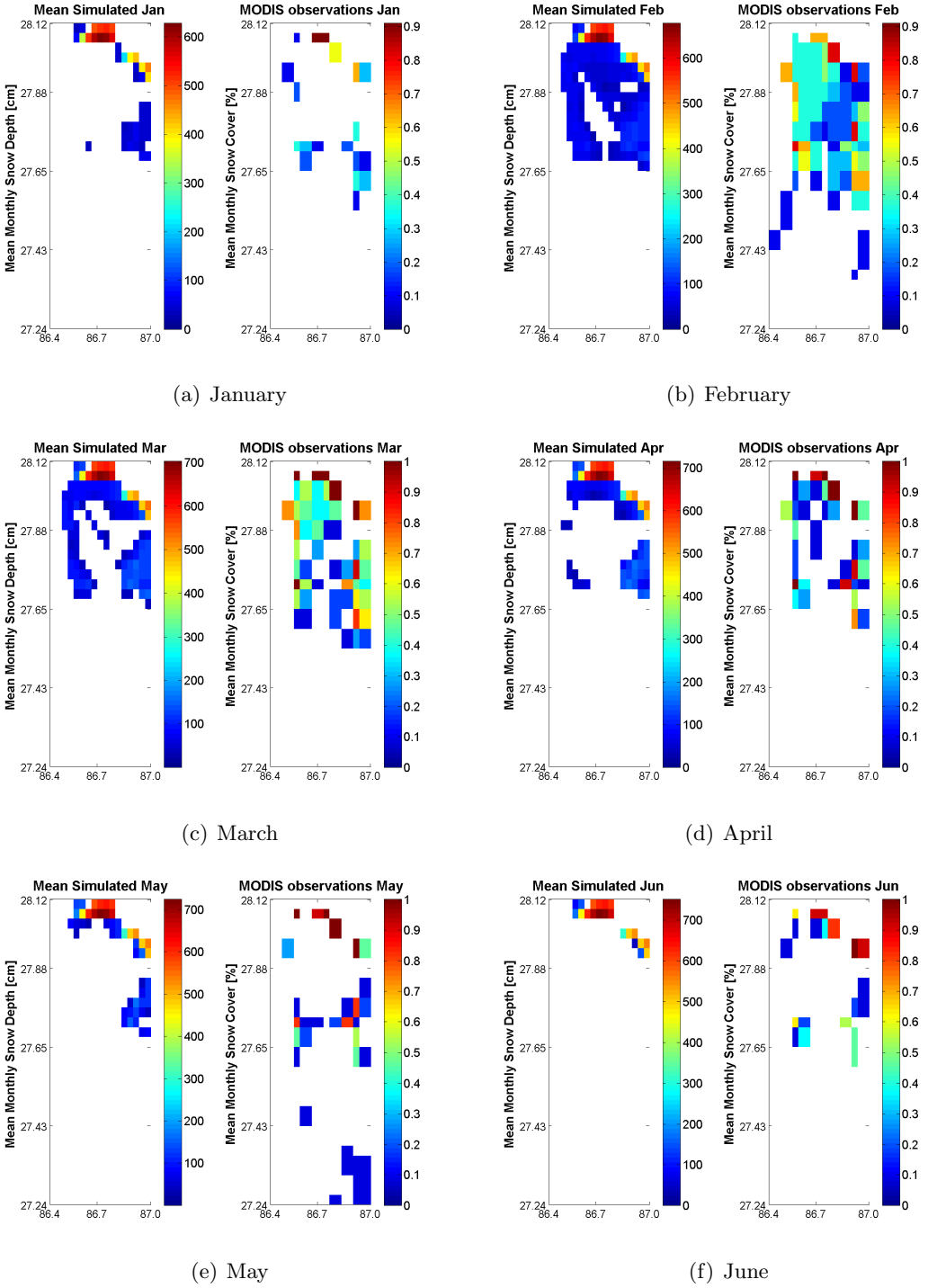

(a) January (b) February

(c) March (d) April

(e) May (f) June

Figure 6.1: Comparison of monthly mean simulated snow depth and MODIS monthly mean snow cover, expressed in percentage of time each cell is occupied by snow, from January to June.

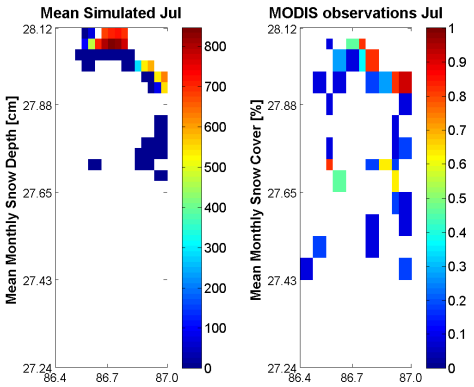

(a) July

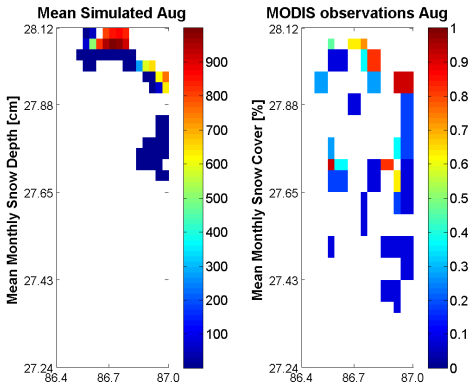

(b) August

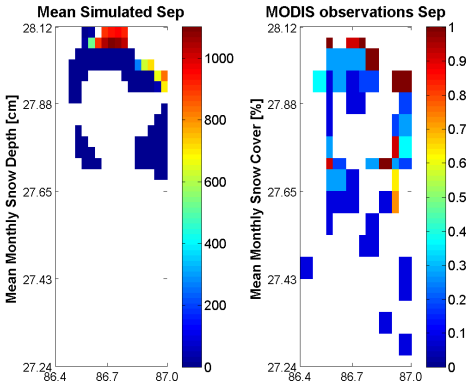

(c) September

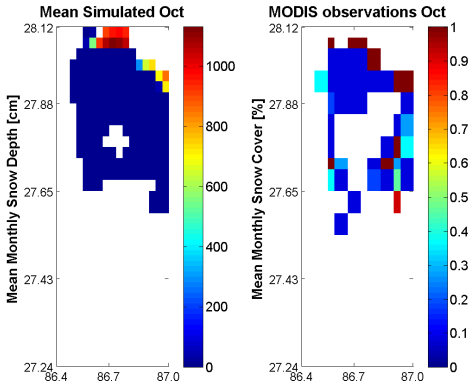

(d) October

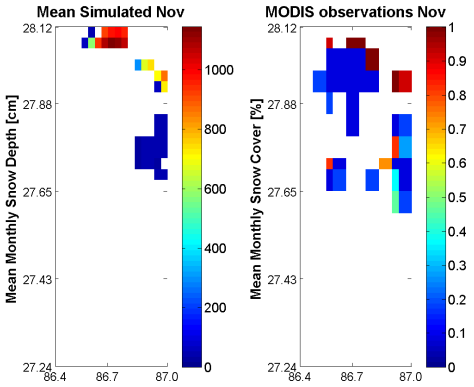

(e) November

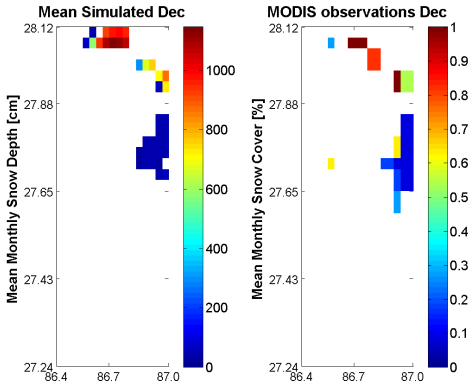

(f) December

Figure 6.2: Comparison of monthly mean simulated snow depth and MODIS monthly mean snow cover, expressed in percentage of time each cell is occupied by snow, from July to December.

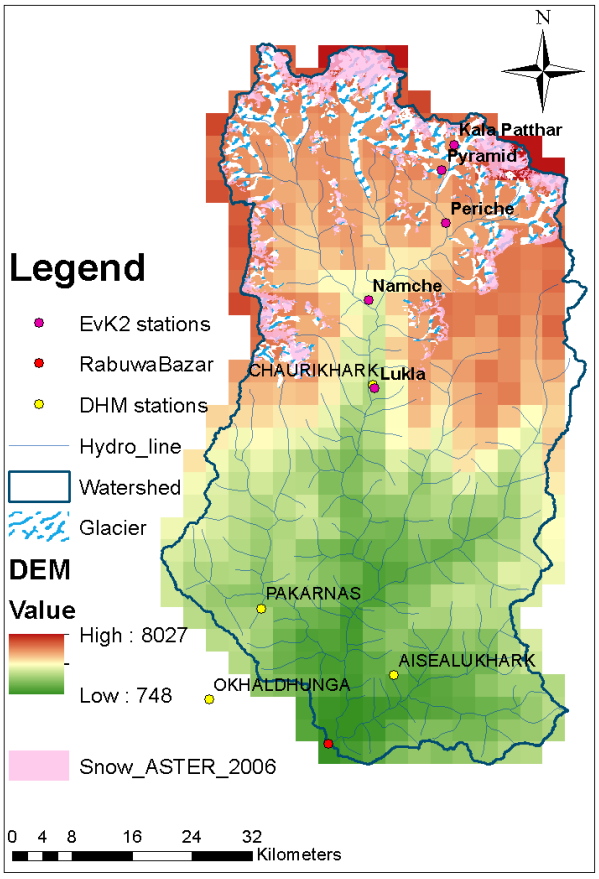

Figure 6.3: Permanent snow cover extent from ASTER imagery for year 2006. Model cells are also represented for comparison with the simulations.

6.2 Rainfall Spatial Distribution

This section shows how the precipitation is spatially distributed on the study area if TRMM scenes are merged with stations data, which provide the "ground truth" for rainfall totals. As detailed in Paragraphs 2.2 and 4.2, rainfall prediction in the Himalayas is extremely challenging because of the interactions between the complex topography and the circulations patterns, the foremost of which is the monsoonal phenomenon. For these reasons, it is believed that altitude-based lapse rates cannot fully resolve the spatial variations of precipitation, thereby satellite scenes are integrated with ground observations. As a result, rainfall fields are expected to fit locally with direct (but scarce) rain gauge measurements and spatially with the shapes of satellite fields in a daily combination of TRMM and rain gauge data.

Here, predicted monthly rainfall totals are visually compared with TRMM monthly averages in order to assess the spatial variations of rainfall. Quantitative comparison is not relevant at stations locations as TRMM data are adjusted in order to match the ground values; further, cross-validation techniques are not applicable in a scarcely−gauged catchment, as their accuracy depends on the number and the location of the gauges within the study area, which should be representative of the distribution of rainfall in space. Velasco-Forero et al. (2009) and Wagner et al. (2012) advance that a more robust validation is mostly of a qualitative nature, e.g., comparison and analysis of interpolated rainfall patterns. Indeed, the decision on the suitability of the predicted rainfall fields should take into account the representativeness of the given measurement network as well as of the spatial rainfall distribution. Figure 6.4 illustrates the comparison between simulated and TRMM observed rain fields, on a monthly basis (Paragraph 4.3.3). Only the monsoonal period is shown because, as explained in Paragraph 4.2.3, it is difficult for TRMM's sensors to detect low amounts of rainfall and thus lapse rates are used over the whole study area for the driest months (October to May). In any case, these months only minorily contribute to the annual hydrological budget, as the bulk of rainfall occurs during the monsoon.

Figure 6.4 clearly shows the effect of the Greater Himalayas orographical barrier on rainfall totals. Indeed, after the topography steeply rises in the middle of the basin (starting at about 4000 m a.s.l.), very little rainfall is observed with respect to the amounts recorded at lower altitudes. At high elevations, the highest rainfall amounts are observed along the main valley, with a peak at its end, in the Khumbu accumulation zone area.

Only liquid precipitation is plotted, as TRMM displays issues in detecting snowfall (see Paragraph 4.3.3). Indeed, TRMM patterns in the upper part of the basin cannot be

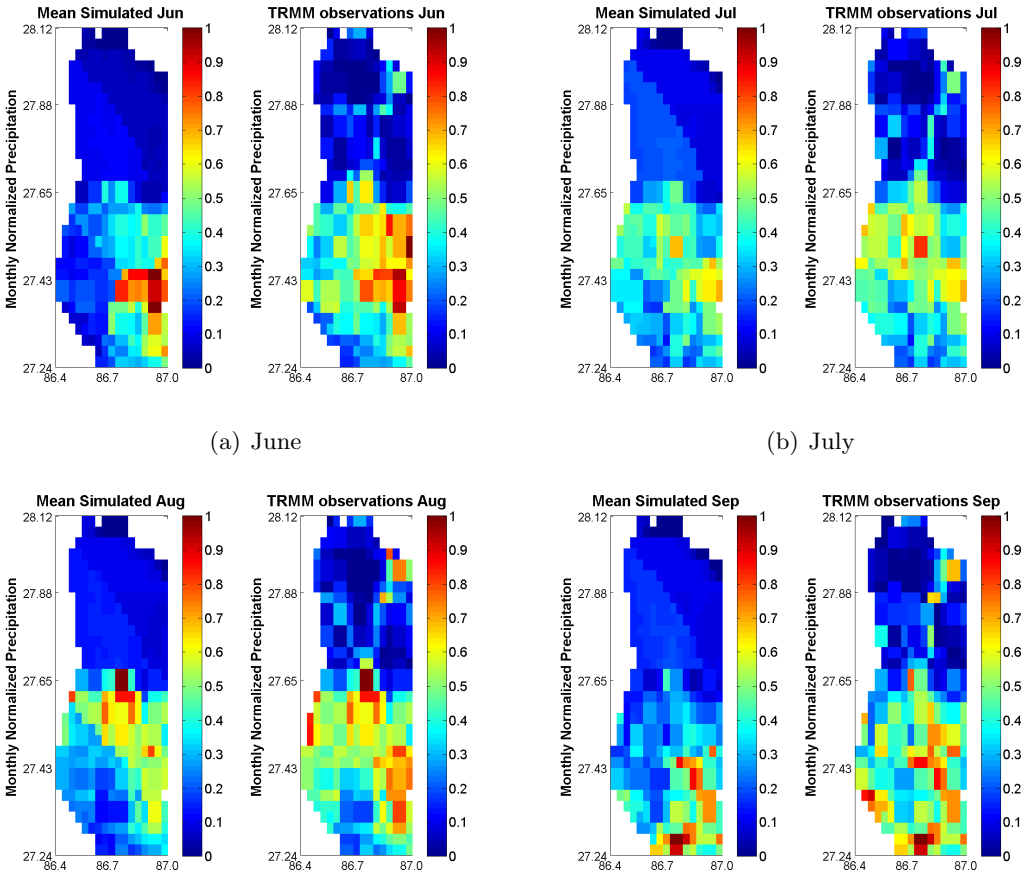

(a) June

(b) July

(c) August

(d) September

Figure 6.4: Comparison of monthly mean simulated rainfall field and long term TRMM monthly averages in the period 2003−2005. To be compared, data are normalized with the monthly maximum rainfall total. Represented period is the monsoonal season, from June to September.

completely trusted, as they do not agree with ground observed trends (see Paragraph 4.2.2); this analysis focuses on the lower altitude part of the catchment. As explained in Paragraph 4.3.3, the TRMM spatial distribution is applied only to the monsoon season (June to September) at low altitudes.

It appears that rainfall fields predicted by merging TRMM and ground data reproduce very well the relative spatial distribution observed from TRMM, even though TRMM scenes are scaled on different ground stations, according to the reference Thiessen polygon. Therefore, monsoonal spatial patterns are well represented, although at the TRMM's pixel scale, which poses a limit to the accuracy. At high altitudes, where only lapse rates are used to predict rainfall, the shapes of Thiessen polygons dominate the spatial variation in the rainfall fields. From Figure 6.4, it stands out how elevation alone cannot resolve the spatial variability of precipitation. This is particularly evident

at lower altitudes, where the air is still rich in moisture and thus more sensitive to orographical obstacles, even though small.

A major constraint in this study is the lack of rain gauges at very high altitudes. At the moment, precipitation gradients are extrapolated from the highest available gauge − Kala Patthar, located at 5600 m a.s.l.; the same holds for snow gauges. However, several stations, covering the full elevation range, are necessary in order to represent the climatic situation correctly and to validate remotely sensed products (Andermann et al. 2011). Stations at very high elevations constitute a technological even before than economical issue, as they face harsh operational conditions; EvK2 has installed two AWSs on Changri Nup glacier (5700 m a.s.l.) and on the route to Everest summit (South Col, 7986 m a.s.l.) but precipitation gauges are either out of order or absent. This issue is affecting the simulations over the smaller catchment closed at Periche, located above 5000 m a.s.l.; there, high uncertainty on precipitation amounts is expected.

In conclusion, within their range of applicability, merging-based prediction methods using a long term averages of TRMM data as covariate are very promising to reconstruct rainfall fields in a scarcely gauged area. Major limitations are the coarse spatial resolution of TRMM scenes, its little reliability at high altitudes and its inability in detecting solid precipitation, thereby the use of TRMM is restricted in space and time.

6.3 Comparison with previous work

Here it is carried out a direct comparison between simulated discharge time series from this study and the previous model (Paramithiotti 2013) implemented on the the same catchment closed at Rabuwa Bazar. The best simulations are chosen for both the theses, being those driven by satellite input data.

There are two main differences between the models. First of all, in the previous thesis a 100 m altitude belts spatial discretization was used, whereas here the basin is subdivided by means of 3000 m side cells. Secondly, different use is made of satellite data. In Paramithiotti (2013), the model is fed with 8−days moving averages of TRMM scenes, here monthly means are merged with and used to spatially distribute ground data. Besides, in the previous thesis MODIS temperatures were only used for computing lapse rates, along with AWS data; indeed, on short time spans MODIS products suffer from cloud cover disturbance, thus their utility is limited. Here, again, employment of long term averages and ground data allows for distributing climatic variables on a daily basis, so that a good representation of those quantity is made possible even for future nearly−real time usages of the model.

Moreover, minor refinements are introduced in this study. To begin with, rainfall is corrected for solid precipitation instead of assuming a linear decay with elevation from Pyramid station on. Then, gap filling is performed for both temperature and precipitation gauged time series, so that a continuous input is provided to the model. Finally, snow and ice melt models are calibrated with direct observations of snow depths time series and ice ablation rates; thus, fewer parameters are left to be calibrated on the hydrograph, reducing the degrees of freedom of the simulation.

Figures 6.5 and 6.6 compare the outcomes of the two models in terms of discharge time series.

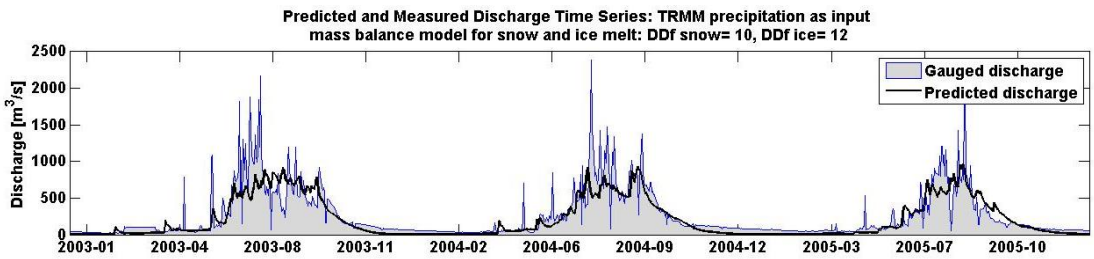

(a) Altitude belts model. From Paramithiotti (2013).

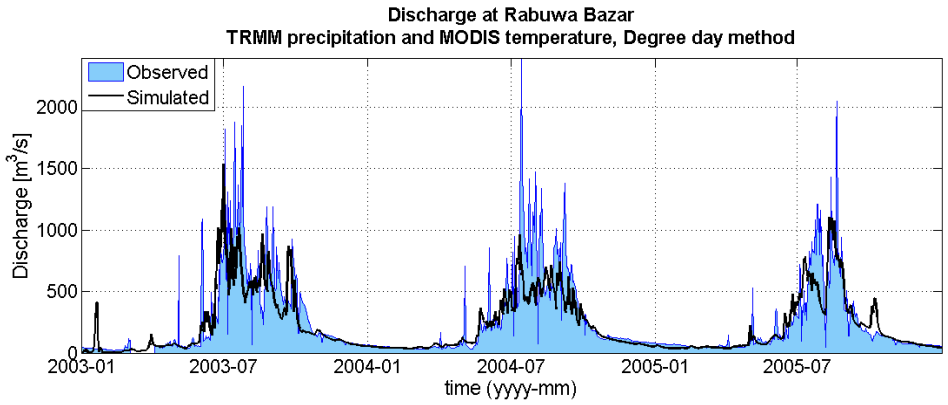

(b) Cells based model.

Figure 6.5: Simulations in 2003 – 2005 from the hydrological altitude belts model (above) and the cells based model implemented in this thesis (below).

A number of improvements can be seen by visual comparison of the hydrographs, even though some issues are still present. The cells model better simulates low flow periods, captures the occurrence of floods in the premonsoonal season and is able to capture infra-seasonal discharge oscillations during the monsoon (see e.g. years 2003, 2008, 2010 for comparison). Peak values are still not predicted, even though progress is made in simulating the flow surge. Improvements in the low flows domain are likely coming from the more accurate spatial distribution of temperatures from MODIS, as low flows are governed by melting (see Paragraph 6.4); on the other hand, those during the monsoon

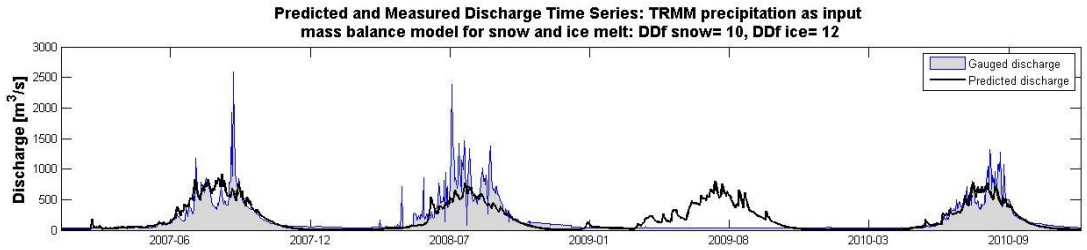

(a) Altitude belts model. From Paramithiotti (2013).

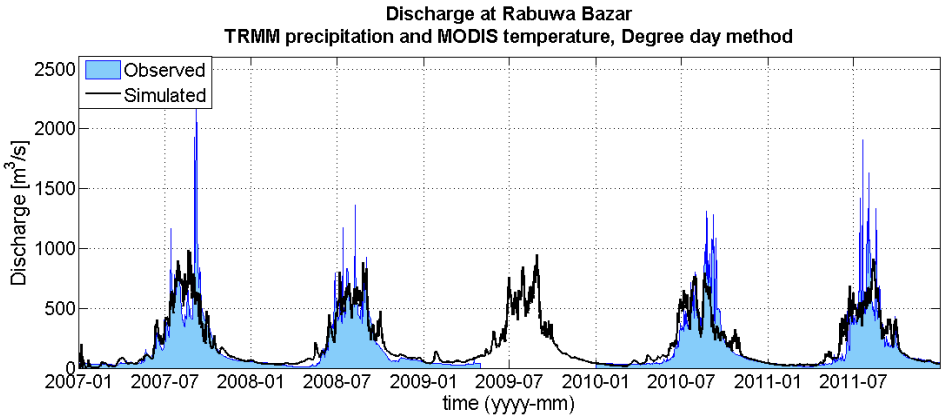

(b) Cells based model.

Figure 6.6: Simulations in 2007 – 2011 from the hydrological altitude belts model (above) and the cells based model implemented in this thesis (below).

period may derive from the assimilation of TRMM and ground data, which describes rainfall spatial variations other than that related to altitude.

Remarkably, no significant worsening in model performance is produced by using monthly instead of weekly satellite rainfall totals, showing that the former can be applied to gain more flexibility to the model. Also, the use of large cells does not affect the outcomes, suggesting that, for this level of analysis, spatial resolution is not a key factor in the model. Instead, relevant improvements will likely be obtained by increasing the gauge network density, especially for solid and liquid precipitation, and by studying the soil water contents, as previously discussed..

6.4 Contributions to the river flow

This section analyses how the different processes contribute to the river discharge at different distances from the head of the river. Knowledge on flow contributions is of paramount importance for understanding the hydrological budget, predicting the future impacts of climate scenarios and assessing natural hazards. Bookhagen & Burbank

(2010) studied the spatiotemporal distribution of rainfall and snowmelt and their impacts on the hydrological budget of Himalayan catchments, finding that wide differences exists both along the range and at the local scale. Therefore, as it is difficult to derive flow contributions from spatial and meteorological analysis, a detailed, integrated hydro−glaciological modelling is fundamental in simulating river flow. Figures 6.7 and 6.8 show the averaged monthly and annual contributions of rainfall (after the removal of evapotranspiration), snow and ice melt at different sections along Dudh Kosi river.

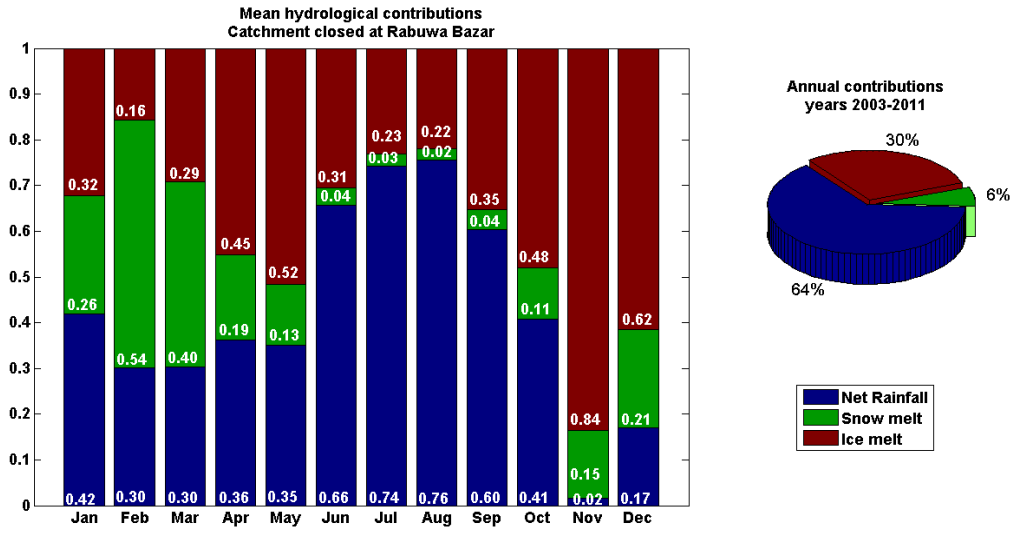

Figure 6.7: Mean monthly contributions [%] to generation of river flow at Rabuwa Bazar (left) and mean annual shares of discharge sources (right) in the period 2003 − 2011.

At Rabuwa Bazar, about 90 km downstream the head of the catchment, discharge is manly formed from rainfall (about 64% of the annual budget); ice melt plays a relevant but not dominant role (about 30% of annual discharge) and snow melt merely contributes to 6% of the annual budget. Seasonal variations in contribution shares exists. Rainfall contributions peak in summer during the monsoon (up to 76%), decrease in the pre− and post−monsoonal seasons and play a minor role in winter, even though significant rainfall shares may be observed (e.g. about 40% in January and February). The comparison of Figures 6.7 and 6.8 suggests that winter rainfall is likely to occur at low and intermediate elevations (below about 4000 m a.s.l.) Ice melt is observed throughout the year, only limited in late winter when the snow cover extent reaches its maximum (see Paragraphs 5.2.1 and 6.1).In the pre− and post−monsoonal seasons, ice melt contributes to nearly half of the river flow; the greatest melt amounts are observed during summer, thus ice melt overlaps with monsoonal rainfalls in determining floods. Finally, snow melt is relevant to discharge formation mainly in the late winter−early premonsoonal season (up to 50% of monthly contributions in February). Bookhagen & Burbank (2010) estimates

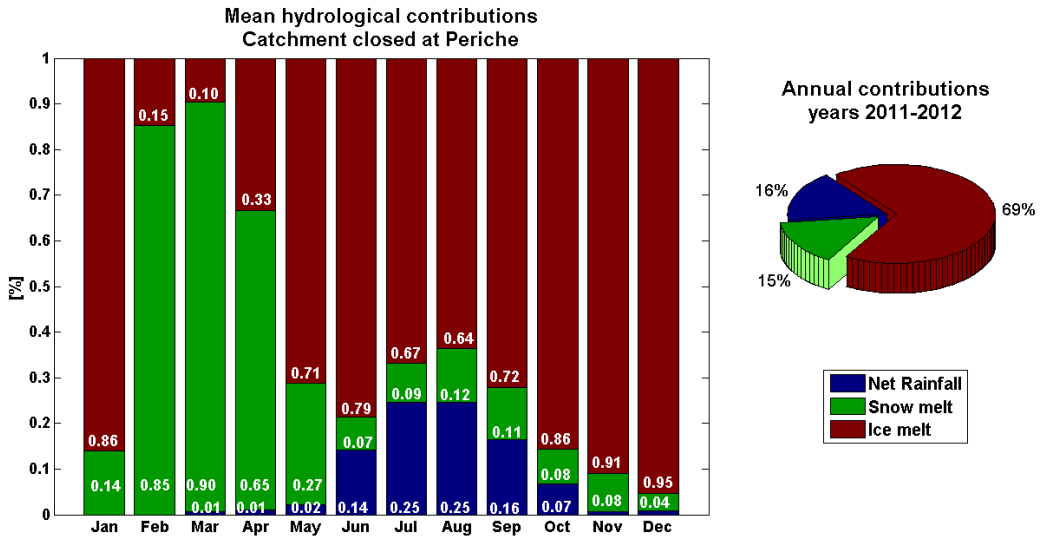

Figure 6.8: Mean monthly contributions [%] to generation of river flow at Periche (left) and mean annual shares of discharge sources (right) in the period 2011 – 2012.

the contributions to the discharge of Tsangpo River, Eastern Nepal, being about 80% from rainfall and less than 20% from snow melt; these figures are similar to the results of this thesis.

Periche river section is located 3.7 km downstream Khumbu glacier's tongue. The discharge at this location appears to be dominated by ice melt during the whole year, apart from those months in which the snow cover prevents ice from melting, i.e. late winter and early premonsoonal season (February−March). Rainfall plays only a minor role, accounting at maximum for 25% of the mean monthly discharge during the monsoon season; even then, ice and snow melt are more relevant than rainfall. This confirms the observed rainfall trends with elevation discussed in Paragraph 4.2, i.e. the fact that the steep orographical barrier drains the air moisture content so that little or no precipitation is left at higher altitudes.

This analysis is the starting point for predictions of the behaviour of the hydrological system, namely future water availability and natural hazards. Several studies (e.g. Bajracharya et al. (2007), Benn et al. (2012), Bolch et al. (2012), Immerzeel et al. (2013)) indicate that in the region glaciers are retreating and this tendency may increase in the near future as a result of climate change. Accordingly, the river flow may undergo increases or decreases in discharge due to changes in precipitations and temperatures, which impact differently the hydrological budget depending on the dominant contributions to flow formation throughout the year.

6.5 Comparison of the simulated discharge at Periche

The two modelling approaches at different scales are compared by paralleling the simulated discharge time series at Periche (Figure 6.9). Noticeably, due to the elevated computational effort, the hydro−glaciological model at finer scale (purple line) is run year by year, causing discharge to abruptly fall in December; this issue is purely computational and does not represent the physics of the system.

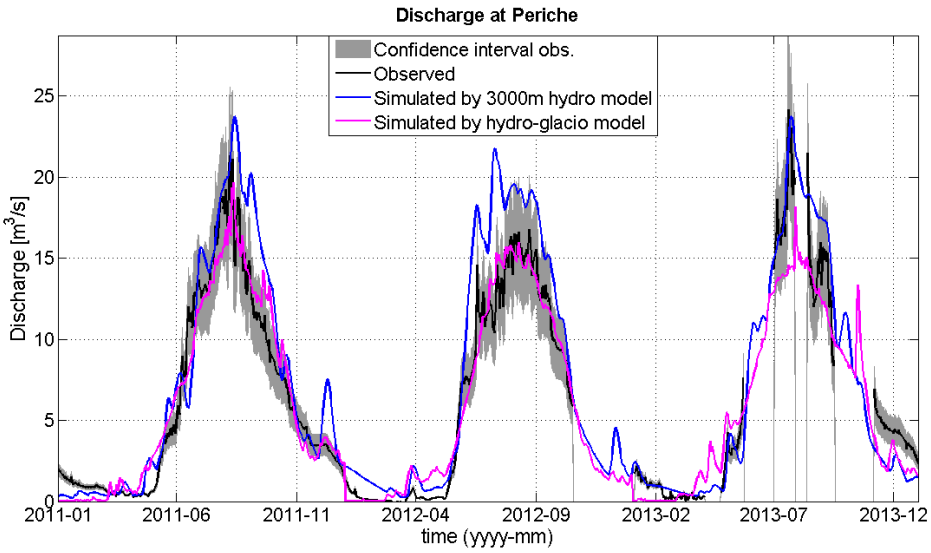

Figure 6.9: Comparison of the two modelling approaches in simulating river discharge at Periche.

The mesoscale hydrological model returns a smoother discharge series, since it has a coarser horizontal resolution (3000 m against 300 m) and simulates with less detail the glaciological process. Generally, the finer scale model generates more accurate discharge predictions, where the mesoscale model tends to overestimate the observed discharge; yet, its predictions are within the 20% confidence boundaries due to measurement errors. The mesoscale model appears to better reproduce the higher flow period during summer 2013, and partly during 2011; however, 2012 is better simulated by the finer scale model. A sounder analysis could be carried out in the future as the recorded time series at Periche increases in length. Issues in predicting discharge at Periche, such as overestimation of snow melt in March−April and of rainfall response in October are present in both the models.

This analysis highlights that, depending on the necessities, both the models could be used to predict discharge at Periche. The mesoscale model generally displays lower but still acceptable performances; it tends to predict false peak in discharge but its accuracy for summer high flow might be good; longer recorded data are needed to assess it. The

finer scale model is certainly more accurate in simulating discharge; it still suffers from high uncertainties in precipitation totals and ice melt predictions (discussed in Paragraph 6.6.1) that will likely decrease as more field data are collected. Another advantage of using the finer scale model is the possibility to study in detail the glacier mass budget.

6.6 Ice melt model for the Khumbu glacier: discussion

Bolch et al. (2012) identify the major uncertainties in modelling the state and fate of high altitude glacierised catchments, such as those in the H-K-H region, as being related to the contribution of glaciers to runoff, the projection of glacier changes, the influence of debris cover on glacier melt, the role of ice and snow avalanches in the glacier mass budget, and the magnitude of past glacier changes; they attribute these uncertainties mainly to the lack of data. Benefiting of field surveys and weather stations data, this study is able to provide valuable information on the behaviour of Khumbu glacier, as it covers the main issues generating uncertainties in understanding of glacierised catchments. In particular, this thesis analyses the contribution of glaciers to runoff, the influence of debris cover on glacier melt and the glacier dynamics.

This section discusses some key points for modelling and understanding the melt processes taking place on Khumbu glacier. First, the performance of the debris model in predicting the spatial distribution of debris thickness and the ice melt under debris cover are analysed (Paragraph 6.6.1). Secondly, the spatio−temporal distribution of ice melt is shown over the year in the study area over the year (Paragraph 6.6.2).

6.6.1 Simulation of debris thickness and ice melt under debris cover

Debris thickness has been evaluated at each cell by estimating an empirical relation between punctual observations on Khumbu glacier and surface temperatures retrieved from Landsat (Paragraph 4.5.2). Here, the debris thickness estimations are tested by comparing the observed values with the simulated ones (Figure 6.10).

Evidently, whereas at some stakes thickness predictions are acceptable, in some other cases the model considerably overestimate debris thicknesses; this holds at the stakes locations, i.e. in the upper part of Khumbu glacier. Noticeably, field measurements are punctual, while simulated values are representative of the whole cell area, thus some error is expected, especially given the high spatial variability of the glacier surface within short distances (Watanabe et al. 1986).

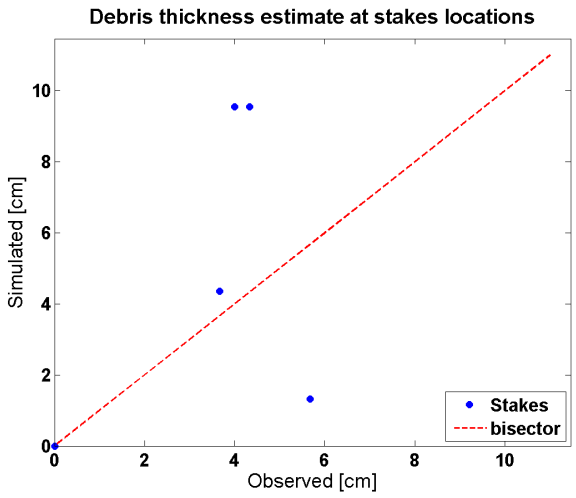

Figure 6.10: Simulated debris thickness at stakes locations against observed values.

Afterwards, model performance in predicting ice melt under debris cover at various thicknesses is checked. Figures 6.11 and 6.12 show the double−mass plot of observed and simulated ice ablation at stakes locations and the mean ice ablation rates simulated at each cell against the debris thickness predicted for the cell, with a possible interpolative functions.

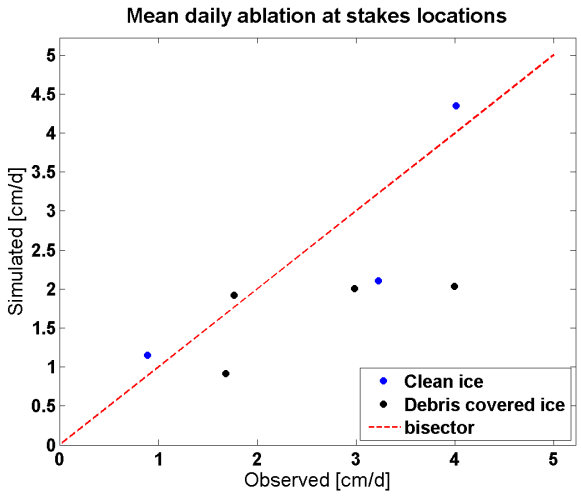

Figure 6.11: Comparison between simulated and observed mean ice ablation rates under debris cover and in debris−free conditions at stakes locations.

Ice melt rates under debris cover are mostly underestimated at stakes locations and up to 10 cm thickness with respect to the interpolative function; however, observed ablations are generally reproduced, especially for clean ice. Under higher debris thicknesses, ice melt is in accordance to the values generally accepted in literature, summarised in Mattson (1993). While underestimating interpolated values, the model seems to reproduce the shape of the interpolative function. The interpolative function for simulated

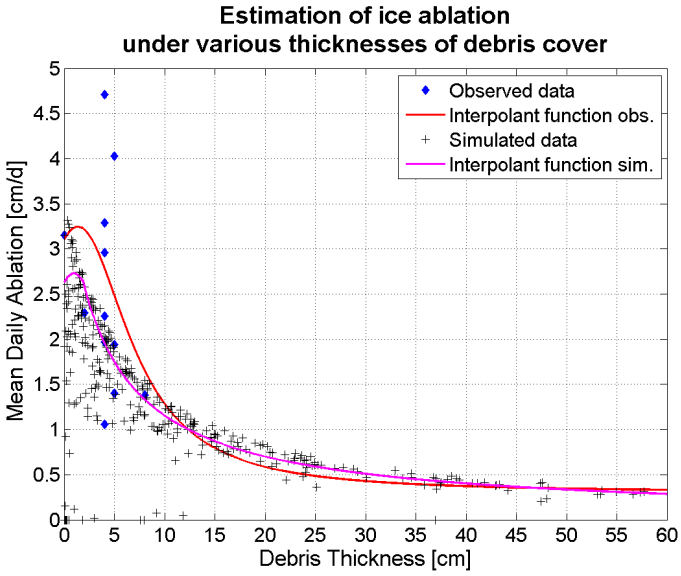

Figure 6.12: Comparison between simulated mean ice ablation under debris cover, observed values and interpolative functions of observed and simulated ice ablation.

ice ablation as a function of debris thickness is shown, displaying similar behaviour as that for observed data, and as those available in literature for other glaciers (Mattson 1993). This suggests that the model is correctly representing the physics of ice melt under debris cover. The major difference with the observations' interpolative function lies in the prediction of ice ablation under thin debris cover, while the asymptotic behaviour under high thicknesses is similar. Regarding clean ice melt, the degree day factor has been estimated from observations, but the radiation factor has been increased in order to match the observed volumes flowing at Periche. The latter has been preferred over matching observed melt rates at few locations.

Multiple sources of uncertainty are introduced when computing ice melt under debris cover. First of all, errors are introduced while estimating debris thicknesses by interpolation (Figure 6.10). Secondly, daily surface temperature for each pixel is computed from debris thickness and daily radiation values, by means of an interpolative function as well (see Paragraph 3.2.2 for details). Finally, the debris effective thermal resistance is calculated from the debris thickness at each cell. While the first two steps introduce errors because of the interpolation, the latter constitutes the major source of uncertainty, as it was impossible to calibrate the empirical relation between thermal resistance and thickness due to the lack of data. Indeed, debris thermal resistance should be calculated at some locations on the glacier by measuring the temperature at the top and at the bottom of the debris layer, and from these observations an equation should be fitted to predict thermal resistances at any location in the study area. However, no such

measurement is available in the Khumbu area, thus it has been used a relation fitted for Baltoro glacier, Pakistan, by Mihalcea et al. (2008). Ice melt rate estimates will certainly improve as temperature measurements will be taken both at the surface and at the bottom of the debris layer.

On the other hand, this method offers advantages as well, in addition to the ability of simulating runoff formation on the glacier. Indeed, Nakawo et al. (1999) claims that one of the advantages of estimating ablation under a debris layer from surface temperature data is that the averaged temperature can lead to realistic averaged ablation rates over a heterogeneous area such as a mixture of icecliffs, lakes and debris covered surfaces, where ablation rates differs significantly from place to place.

6.6.2 Spatio−temporal distribution of ice melt

The model simulates daily ice ablation at each cell throughout the whole simulation period; therefore, the spatial and temporal evolutions of ice melt can be analysed. To begin with, Figure 6.13 presents the cumulative annual ice ablation over the study area; the analysis is carried out for year 2011 as similar results are obtained for the other simulation periods.

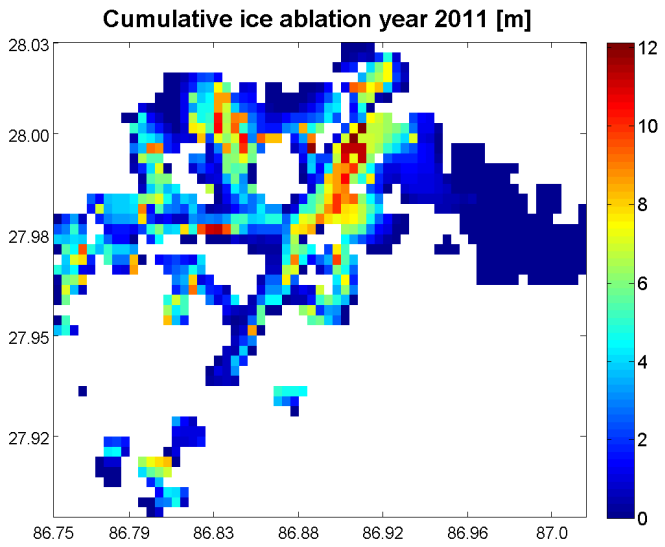

Figure 6.13: Simulated cumulative ice ablation during 2011.

The model simulates cumulative ice ablation amounting to about 10 to 12 m per year. Ice melt is more relevant in the upper part of Khumbu and Changri Nup glaciers, where little or no debris cover is present; some ablation is also simulated on Khumbu's tongue, decreasing till disappearing close to the terminus, where thicker debris layers

are located. By comparison with satellite images (e.g. Figure 2.7), it results that ice melt on Khumbu's tongue is concentrated around supraglacial ponds and streams, as already Watanabe et al. (1986) had observed. Ice thickness variations are not shown, as they are strictly related to the dynamics model discussed in Paragraph 6.7.

Figure 6.14 decomposes the total annual melt in its seasonal contributions. As expected,

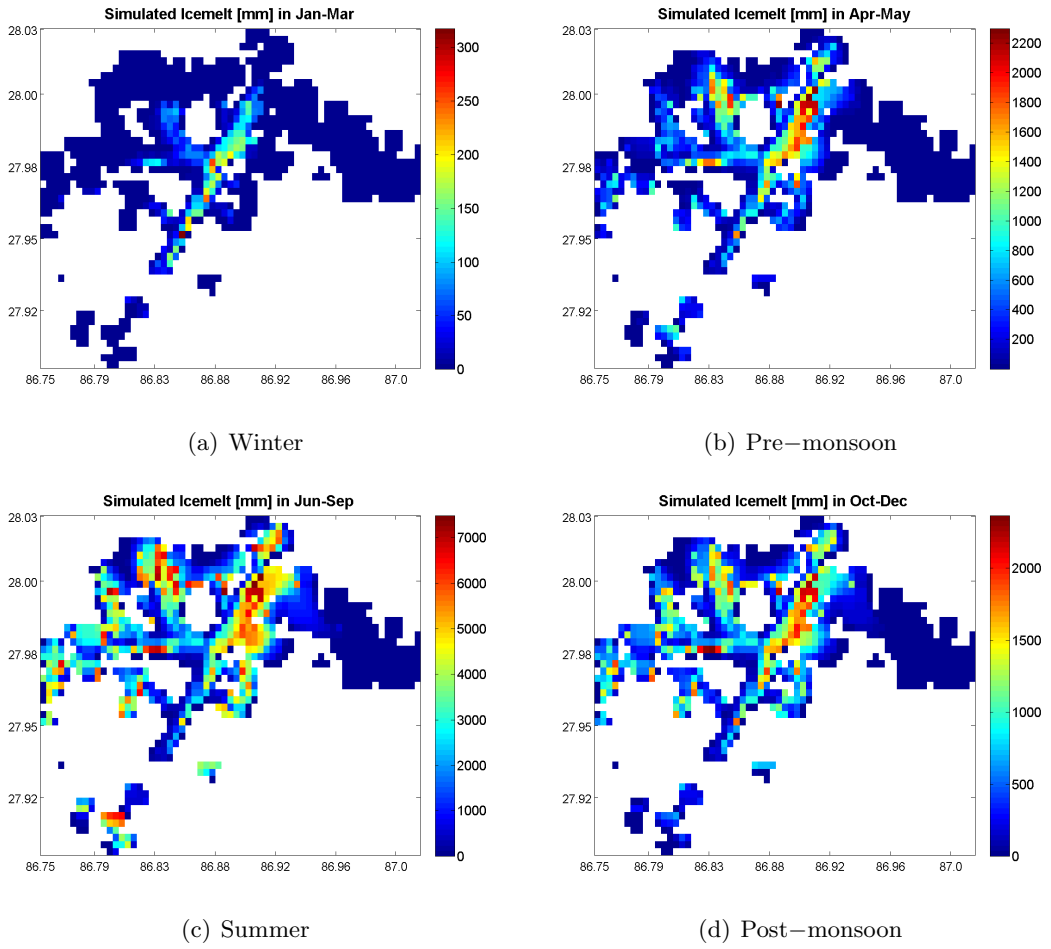

(a) Winter

(b) Pre−monsoon

(c) Summer

(d) Post−monsoon

Figure 6.14: Simulated cumulative ice ablation during each season, in 2011.

the bulk of ice ablation occurs in summer, followed by spring and autumn, whereas much lower rates are simulated in winter. From January to March, ice melt is limited to the lower part of the glacier, i.e. Khumbu's tongue, while during the rest of the year, it occurs on most of glacierised area. However, no ablation is simulated on Khumbu Icefall and accumulation zone. This is likely due to the higher elevation of the Icefall if compared with the glacier tongue, and to its west−facing orientation, so that it is likely to receive less incoming solar radiation. Thus, the model sets Khumbu's equilibrium line altitude (ELA) at the Icefall, coherently with other studies (e.g. Benn et al. (2012), Nakawo et al. (1999)). The active terminus is simulated being about 2 km above the

apparent one, confirming the observation of Nakawo et al. (1999) positioning the active terminus 3 km upstream the apparent one.

Figure 6.15 shows the cumulative ice ablation in each simulated year. Unfortunately, ablation data are only available for year 2014, not covered by the simulation, so that a direct comparison of cumulative melt amounts is currently not possible. However, since climatic inter-annual variability is generally limited, the results from the different years are shown together.

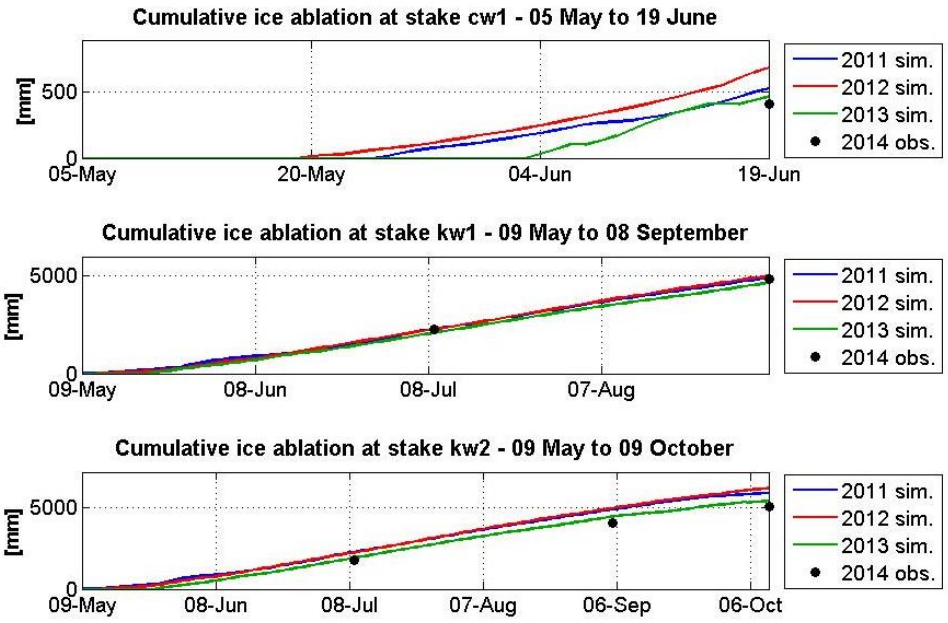

Figure 6.15: Simulated cumulative ice ablation at those stakes located on clean ice. The lines preprent the simulated values (2001−2013), the dots the observations (2014).

Cumulative ice ablation patterns are similar for all the simulated years, and noticeably well represent the ablation patterns observed from the surveyed stakes in 2014. Ice melt in the highest part of Khumbu and Changri Nup glaciers onsets in May, after the snow cover has been depleted, and continues at a more or less constant rate till September, when the ice melt rate decreases. Ideally, the performance of the ice melt module will be tested once the meteorological data from 2014 are available to run the model; however at the moment the comparison between ablation in different years seems to suggest that the clean ice melt process is well simulated.

6.7 Glacier dynamics model

During the field survey in 2014, a number of stakes have been installed on Khumbu and Changri Nup glaciers, both on clean and debris covered ice. Stakes locations have been measured by means of the GPS post processing positioning technique at two different epochs, i.e. in May and October 2014. Glacier velocities are thus computed as ratio of distance between the initial and final position of each stakes and the elapsed time between the measurements. Table 6.1 illustrates the resulting surface velocities; the accuracy obtained from post processing of GPS data is below the metre. Surface velocities are then reduced to mean velocities along the vertical profile by means of the coefficient 0.8 as suggested by Cuffey & Paterson (2010). Indeed, the glacial motion is not expected to entirely occur by slip, but may also have a deformation component; it has been observed that depth averaged velocities are similar to the surface ones through the coefficient 0.8.

Table 6.1: Calculated glacier surface velocities from GPS positioning at stakes locations performed in May and October, 2014.

Stake ID	Elevation [m a.s.l.]	Velocity [m/y]
Kw2	5237	19.72
Kb1	5258	26.64
Kb2	5226	15.57
Kb4	5055	7.82
Kb5	5059	10.41

The comparison between observed values from 6.1 and simulated ones is carried out in Paragraph 5.3.4 while calibrating the glacier dynamics model.

Remarkably, surveyed velocities are in general agreement with those predicted or measured in previous studies. Naito et al. (2000) calculated ice velocities on Khumbu glacier by implementing the continuity equation coupling mass balance and glacier flow based on topographical surveys. They find a maximum flow speed of 50 m/y monotonically decreasing downstream the glacier. Similar results are obtained by Kodama & Mae (1976), who measured stakes displacements over time by means of topographical triangulation, yielding ice velocities of 40 m/y. Nakawo et al. (1999) also report smaller velocities, estimated by comparing satellite images at different times; they find the flow speed being 20 m/y 1 km from the Everest Base Camp and decreasing velocities downstream till null values 10 km from the EBC. More recently, Quincey et al. (2009) use both interferometry and feature tracking on Landsat images to estimate spatially distributed ice velocities in the Everest region. Velocities for Khumbu glacier tongue are computed between 5300 and 4900 m a.s.l., amounting to 10 to 25 m/y between 5200 and 5000 m a.s.l. and then decreasing to 0 to 10 m/y; noticeably, data exhibit large scatter, denoting strong variations in space. Their results are in agreement with measured velocity

values in Table 6.1. Finally, Peters et al. (2010) measure surface velocities of glaciers in the Khumbu region both manually and automated−based on multi-temporal Ikonos and ASTER data, finding maximum surface velocities of 60 m/y at the Khumbu Icefall, subsequently decreasing till less than 5 m/y at Lobuche, 2 km up from the terminus. According to their map of velocities, at the surveyed stakes locations the flow speed is approximately 15 to 25 m/y, in agreement with the values in Table 6.1.

The spatial distribution of mean annual ice velocities resulting from the model is investigated (Figure 6.16). The highest velocities are reasonably observed at the Khumbu

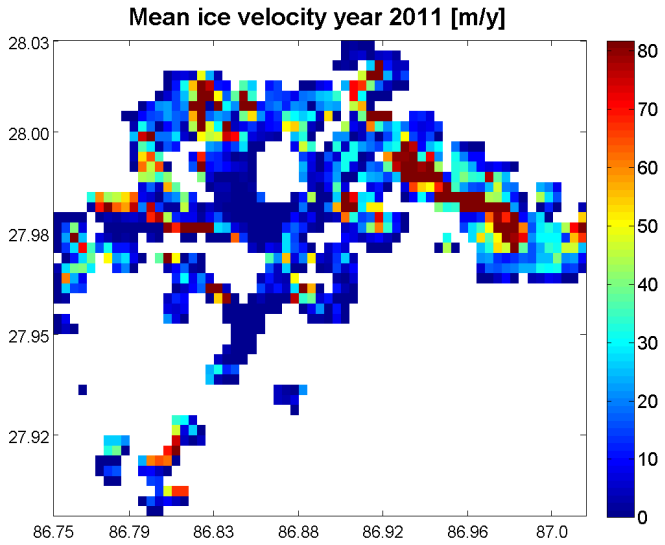

Figure 6.16: Simulated ice velocity, averaged over the vertical profile and in time during year 2011.

Icefall and at the head of Changri Nup glacier, i.e. where surface slope is greater. Right after the Icefall, an abrupt change in velocities occur due to the change in slope and flow direction, as the glacier turns around the west flank of the mountain. Downstream on the ice tongue velocities decrease till disappearing north to Lobuche, approximately $3-4$ km from the terminus; this is expected since slope and ice thickness sensibly diminish. At the terminus, the model simulate ice flow because of the steep slope in those cells, but the glacier is likely not moving in reality.

Spatial distribution of velocities shows good agreement with those estimated by Quincey et al. (2009) and Peters et al. (2010). Maximum surface velocities calculated in this thesis reach 80 m/y, against maximum values of about 50 m/y in the other studies; however, previous works did not model the Khumbu Icefall, probably because it is difficult to be tracked with automatic image analyses as no constant, detectable shape are present on its surface. In the region where previous works identifies maximum velocities, the flow

model returns values of about 40 m/y, thereby agreeing with satellite estimates at finer spatial resolution. Noticeably, both this study and previous ones identify a stagnant zone on Khumbu glacier for the lowermost 4 km of its tongue. Also Benn et al. (2012) report that downwasting [in Khumbu region] has been accompanied by a reduction in glacier surface gradients and velocities, and large parts of the lower ablation zones of the major glaciers are now stagnant.

Therefore, even though the dynamics model introduces several simplifications and assumptions, its performance is comparable to that of ice velocity estimation from satellite images tracking. For the future, it is recommended to introduce at least an interaction term between the cells, to ensure a more physically based outcome. Further, when running the model over long time spans as for instance in climatic scenarios, it would be interesting to compare the outcomes from this model with those of other conceptual models available in literature, such as that developed by Oerlemans (Oerlemans 2001). Indeed, the currently adopted model requires an upper bound for basal shear stress as neglecting several equilibrium components would results in overestimating shear stress and consequently ice velocities. It would be interesting to test the results from a more physically based model.

Chapter 7

Conclusions

This study has implemented a semi distributed hydro−glaciological model for the Dudh Kosi basin, that takes meteorological data as inputs and predicts discharge at different sections of the river along with glacier ablation and dynamics. This model constitutes a tool for hydrological analysis, natural hazards assessment and water management in the Koshi river system. The major innovation consists in the fact that, in our understanding, no similarly thorough model has been developed so far for large, partly glacierized catchments, whereas these areas are particularly prone to floods, glacial outbursts, landslides, droughts and water resources depletion. Various studies have been formerly carried out on some of the components of the hydrological and glaciological balance in high altitude, low latitude poorly gauged catchments, and their findings and weaknesses forms the background for this thesis.

In this study, several modules from contemporary research studies are adapted and inserted in a comprehensive modelling approach, in addition to original techniques developed to spatially distribute meteorological inputs. The model is tuned at different spatial resolutions and scales in order to better understand the flow formation process along the river with increasing distance from the glaciated headwaters.

This chapter describes the major achievements of the study (Paragraph 7.1) and suggests possible future work for refining the model along with its possible future applications (Paragraph 7.2); the mesoscale hydrological model and the finer scale hydro−glaciological one are discussed separately .

7.1 Achievements

The hydrological modelling of Dudh Kosi catchment is carried out at the mesoscale for the catchment closed at Rabuwa Bazar, and at a finer scale focussing on the sub−catchment closed at Periche, about 4 km from Khumbu glacier's terminus. This section first presents the improvements this study provides for the hydrological modelling of a high altitude partly glacierised catchment in a scarcely gauged basin in the Himalayas. Subsequently, it illustrates the accomplishments of the detailed glacio−hydrological modelling carried out for Khumbu glacier.

7.1.1 Mesoscale hydrological model

A semi−distributed conceptual hydrological model is implemented for Dudh Kosi river; the domain is discretised in cells with an horizontal resolution of 3 km × 3 km. THe model receives weather variables in input and simulates discharge time series, along with ice and snow melt processes and snow cover extension. Cryospheric processes are reproduced by means of a temperature index model; at this resolution, it is not possible to discriminate between clean and debris−covered ice melt. The following presents the major model accomplishments:

1. Data treatment techniques are adopted in order to compensate for the gaps affecting observations from automatic weather stations located at high altitudes. Indeed, several data are missing, frequently from multiple stations at the same time, potentially preventing model simulations. Therefore, gap filling techniques for rainfall, temperature and radiation are developed to reconstruct daily series of these variables. The low station density and contemporary missing data from multiple stations hinder the adoption of geostatistical methods in favour of simpler single station−based techniques. The results for temperature and radiation are satisfactory, whereas rainfall reconstructed time series can be subject to further improvements.

2. Original methods have been developed to spatially distribute the input meteorological variables over the study area. The semi−distributed modelling approach is indeed limited by the low gauge network density in the catchment, partly due to harsh terrain and climatic conditions. This issue is addressed by integrating ground observations from weather stations with satellite data; TRMM long term monthly averages are retrieved for rainfall and MODIS monthly averages are used for temperature. Remote sensing rainfall and temperatures are validated by comparing mean monthly ground observations with satellite data at the stations locations.

It emerges that the absolute values of MODIS temperatures and TRMM rainfall totals cannot be trusted but need to be re-adjusted to the ground observations. A modified bias−adjustment method is implemented; while being one of the simplest available for satellite and ground data merging, it has been shown that on complex topography and in scarcely gauged regions simpler methods are more robust (Dinku et al. 2014). As a result, daily temperature and rainfall spatial patterns are simulated at the satellite pixel scale, accounting for spatial distribution of these quantities. Analysis of the outcomes shows in particular that topography−related gradients are introduced. The annual distribution of TRMM rainfall results to be incompatible with ground observations at high altitudes (above 4000 m a.s.l.), thus in that region altitude lapse rates are used to distribute rainfall.

3. A temperature index model for ice and snow melt is calibrated with snow depth time series and ice ablation rates. The model set up is able to accurately reproduce snow depth time series at Pyramid AWS. Further, the simulated snow cover extent displays good agreement with the MODIS snow cover product, in terms of mean monthly average snow cover extension. On average, the minimum snow cover extent is simulated and observed in the driest winter months and in June−July during the melt season. Permanent snow is simulated above 5700 m a.s.l. in the northern part of the catchment; if compared to ASTER permanent snow cover extension, the model fails at capturing permanent snow cover in the southern crests, where only seasonal snow cover is replicated. The degree day factor for snow is calibrated, while that for ice is computed from observations of ice ablation on Khumbu glacier during the melt season, from May to October, 2014.

4. The semi−distributed hydrological model is able to simulate discharge time series at Rabuwa Bazar with acceptable performance (yielding 0.68 for NSE and 0.71 for logarithmic NSE) and generally good agreement with the observed hydrograph. Temporal variations are reproduced, and low flows are simulated well; however, detecting peak discharge magnitudes during the monsoonal season is still challenging. Mean monthly discharges are simulated fairly well, only displaying some under− or over−estimation in the monsoonal season. Thus, the monsoonal season appears to be the most critical period to be simulated; however, it should be considered that high discharge values are affected by larger uncertainties than low ones as the stage−rating−curve is based on an inadequate number of measurements for high flow conditions.

5. The impact of different datasets as input to the model is assessed by alternatively running the model with rainfall and temperature grids built either upon satellite−merged data or altitude lapse rates of ground stations data. The former

returns at least similar and even higher model performance than the latter, especially during low flows and the monsoonal season. The employment of long term averages of satellite data does not prevent the model from being used in forecast and nowcast mode for flow prediction, as only ground observed weather data are required as daily inputs.

6. The semi−distributed, cell based model implemented in this thesis is compared with the previously adopted altitude belts model (Paramithiotti 2013). The two models differ also in the spatial distribution of weather variables, as the latter was fed with 8−days TRMM rainfall averages and altitude lapse rates for temperature; further, no data gap filling and solid precipitation correction at high altitudes were implemented, and finally melt parameters were not calibrated upon ground snow depth and ice ablation data. A number of improvements can be seen by visual comparison of the hydrographs (Figures 6.5 and 6.6); the present model simulates far more accurately the temporal variations in discharge, as well as floods occurrence, with respect to the altitude belts one.

7. The hydrological model constitutes an useful tool for understanding the hydrological budget in the catchment, particularly valuable for water management and hazards assessment. In addition to simulating river flow along the Dudh Kosi River, it provides information on the cryospheric contributions to flow in the different seasons. On annual average, ice melt contribute to 30% of the river flow at Rabuwa Bazar, snow melt accounts for about 6% and the rest derives from rainfall. Ice melt dominates the rivel flow in May, November and December, whereas snow melt is the major contribution in February and March.

7.1.2 Finer scale hydro−glaciological model

A semi−distributed hydro−glaciological model is implemented for the subcatchment of the Dudh Kosi River closed at Periche, with an horizontal resolution of 300 m. Snow and clean ice melt are simulated by means of an hybrid model, while ice melt under debris cover is predicted by means of an energy balance approach. A glacial hydrology routine routes flow through ice, snow and soil separately. A glacier dynamics conceptual model is applied to simulate ice flow. In detail, the following achievements are obtained:

1. An unprecedented comprehensive modelling approach is implemented over the Khumbu area; the main features of the cryosphere are simulated. Debris cover extension and distributed thickness is mapped from satellite and field data, ice melt rates under debris cover and for clean ice are computed form field data and

subsequently spatially distributed, debris surface temperature at each cell is daily simulated. The results are in agreement with measurements and estimations reported in literature.

2. Furthermore, at this horizontal resolution it is possible to spatially distribute solar radiation accounting for topographical effects such as shading and aspect; daily cloud cover conditions of the sky are used to correct the incoming solar radiation. As a result, melt processes are more physically−based simulated, so that cumulated observed and modelled discharge volumes are very well represented. It is also possible to investigate the spatio−temporal distribution of ice melt; it results that from January to March, ice melt is limited to the lower part of the glacier, i.e. Khumbu's tongue, while during the rest of the year, it occurs on most of glacierised area; the Equilibrium Line Altitude is simulated at the Khumbu Icefall, whereas the active terminus at about 2 km upstream the apparent one. The cumulative annual ablation amounts at maximum to about 12 m in the areas where the debris cover is thinner; annual ablation on Khumbu's tongue ranges from 0 to 5 m.

3. The model is able to simulate river discharge in a high altitude, scarcely gauged glacierised catchment. Simulated discharge time series agrees well with the observed one, which is nevertheless affected by high uncertainty in the rating curve estimate. NSE coefficient is found to be 0.94 and 0.97 for the calibration and validation periods respectively, while low values of logarithmic NSE (-0.5 and 0.41) indicates that low flows are poorly represented; this is partly to be ascribed to the impacts of initial conditions, as observations are available over little periods. However, the model performs well in simulating the higher flow periods, capturing the magnitude and temporal variations of observed discharge. The most critical period to be simulated is the snow melt season, form March to April, when discharge is overestimated by the model.

4. Simulated discharge at Periche is compared between the two models. The analysis highlights that, depending on the necessities, both the models could be used to predict discharge at Periche. Indeed, while being less accurate and occasionally predicting peaks in discharge that are not observed, in two out of the three years the mesoscale model appears to better capture the summer high flows. However, longer records of discharge are necessary for a sounder assessment. The finer scale model should be preferred when specifically studying the river flow at Periche and the glacier mass budget and dynamics.

5. By discriminating the flow routing through different means (soil, ice, snow), the model is able to illustrate how the different contributions impact the river flow both in terms of monthly averages and time series; by discriminating the lag times

between the means, it is possible to account for water storage in ice and firn. The river flow at Periche is dominated by ice melt throughout the year, apart from February and March when snow melt is the most relevant contribution to discharge; rainfall contribute at maximum to 25% of monthly river discharge.

6. Glacier dynamics is also included in the model, simulating ice flow by means of a conceptual model assuming basal slide as driving force. The ice thickness is estimated from the DEM and a reasonable value of basal shear stress, and the ice flow velocity is computed at each cell after calibrating the model with field observations. On the short period, the model returns a spatial distribution for ice velocity that is consistent with satellite estimates provided in independent studies, thereby showing potential for analysing the future evolution of the glacier.

7.2 Follow up

This section presents suggestions for improving the modelling approach by deepening particular features, along with possible applications for studies in the Dudh Kosi region and on Khumbu glacier.

1. Model performance will certainly benefit from accurate reconstruction of missing data in rainfall time series, more relevant at high altitudes (above 3000 m). This is particularly challenging in a scarcely gauged region, with short recorded time series (up to 10 years). However, stochastic rainfall field generators might be used to simulate rainfall occurrence as a stochastic process. Indeed, the major limitation of the gap filling technique adopted in this thesis is the inability to discriminate between rainy and dry days, which in turn affects discharge predictions.

2. The major issue in simulating daily discharge time series is the model inability to detect peak discharge during the monsoonal season. This issue might result from insufficient spatial representation of rainfall; it could be addressed by improving the spatial distribution of rainfall derived from remote sensing data and by increasing the gauge network density. The recently launched GPM mission products could be tested as input to the model to improve the discharge simulation during the monsoon. However, this might reduce the flexibility of the model by requiring frequently updates of satellite input data. Precipitation observations reveal that there is great variability over short horizontal distances (Immerzeel et al. 2014), and several scale-dependent mechanisms may explain the observations. Thus, a denser network would allow for better detection of rainfall peaks during the monsoon; further, it may permit to adopt geostatistically rigorous approaches for meteorological

data gap filling, which presented some issues for precipitation. As installing new gauges might not be feasible in the immediate future, the performance of GPM products against ground data should be assessed. Another important feature of GPM is the ability to detect snowfall, which will provide more accurate estimates of precipitation especially at higher altitudes, since at the moment precipitation gradients need to be extrapolated above 5600 m a.s.l., where about one third of the study area is located.

3. However, poor representation of monsoonal peaks in discharge might be also due to inaccurate simulation of soil water content. Indeed, Nepal et al. (2014) are generally able to reproduce peak discharge at Rabuwa Bazar by introducing a detailed simulation of water storage and movement in the ground. However, soil data are only available at rough spatial resolution, and soil water content has not been sampled so far. Future work might study the influence of this variable on the simulated discharge, and ideally field data will be collected to support the analysis. Noticeably, Nepal et al. (2014) use a fully distributed model for flow routing through the soil reservoirs, while here a simpler semi−distributed approach is adopted in order to limit the computational costs.

4. A number of actions could be undertaken in order to reduce uncertainties in ice melt predictions at the finer scale model. First, it is recommended to sample debris thicknesses on the tongue of Khumbu glacier, so that it would not be necessary to arbitrarily constrain the relation between surface temperature and debris thicknesses. Secondly, temperature needs to be measured at the base of the debris layer in order to estimate its thermal resistivity. Finally, ice ablation rates could be measured at different elevations on the glacier for better understanding the influence of the different factors governing ice melt. Future field surveys should address these needs, as the already available data have allowed significant improvements in the modelling approach, showing the potential of further work.

5. A snow maturation model accounting for snow accumulation, metamorphosis and melting could be developed to improve the mass balance approach. Besides, a module simulating permafrost and mass transport by active rock glaciers, along with their responses to changes in climatic conditions, could be developed to deepen the representation of the cryospheric processes. Moreover, the glacier dynamics model could be improved by introducing forces in the equilibrium accounting for interactions between ice masses, later drag of moraines, creep deformation. Finally, the glacial hydrology routine could be further developed in order to model the interactions between the different systems of reservoirs.

6. From the set up model, climate change projections can be performed in order to predict the variations in the hydrological regime under different scenarios. This would allow for detecting criticalities and sustainable water management practices in the region, in order to ensure water availability and food security. In particular, the finer scale model could be used to simulate the fate of Khumbu glacier in the next decades.

7. Another possible application of the model is the analysis of hydrogeological hazards in the study area, characterised by a steep and fragile topography. The model indeed receives meteorological variables as input and returns discharge time series along the Dudh Kosi River; thus, it could be used for assessments of water resources statistics and extremes and flood mapping. It is however recommended to further study rainfall and soil water content simulation in the mesoscale modelling approach, as peak discharge magnitudes are still poorly depicted. On the contrary, the final scale model is able to capture discharge variations.

These improvements are intended to provide a better understanding and depictions of the hydrological and glaciological processes occurring in the Himalayan catchments. Modelling flow discharge along Himalayan rivers and cryospheric processes is fundamental as extreme disastrous events are becoming more and more frequent in the region, while climate change threatens to deplete water resources stored in the glaciers, thus impacting the hundreds of millions of people living the H-K-H region.

Bibliography

Andermann, C., Bonnet, S. & Gloaguen, R. (2011), 'Evaluation of precipitation data sets along the Himalayan front', *Geochemistry, Geophysics, Geosystems* **12**(7).

Anders, A. M., Roe, G. H., Hallet, B., Montgomery, D. R., Finnegan, N. J. & Putkonen, J. (2006), 'Spatial patterns of precipitation and topography in the Himalaya', *Geological Society of America Special Papers* **398**, 39–53.

Bajracharya, B. & Uddin, K. (2010), Study of Land Cover Dynamics in Sagarmatha National Park and Buffer Zone, *in* 'Proceedings of the 10th International Symposium on High Mountain Remote Sensing Cartography', pp. 125–132.

Bajracharya, S. R., Mool, P. K. & Shrestha, B. R. (2007), 'Impact of Climate Change on Himalayan Glaciers and Glacial Lakes - Case Studies on GLOF and Associated Hazards in Nepal and Bhutan', *International Centre for Integrated Mountain Development (ICIMOD)* .

Barnett, T. P., Adam, J. C. & Lettenmaier, D. P. (2005), 'Potential impacts of a warming climate on water availability in snow-dominated regions', *Nature* **438**(7066), 303–309.

Barros, A., Joshi, M., Putkonen, J. & Burbank, D. (2000), 'A study of the 1999 monsoon rainfall in a mountainous region in central Nepal using TRMM products and rain gauge observations', *Geophysical Research Letters* **27**(22), 3683–3686.

Benn, D., Bolch, T., Hands, K., Gulley, J., Luckman, A., Nicholson, L., Quincey, D., Thompson, S., Toumi, R. & Wiseman, S. (2012), 'Response of debris-covered glaciers in the Mount Everest region to recent warming, and implications for outburst flood hazards', *Earth-Science Reviews* **114**(1), 156–174.

Bolch, T., Kulkarni, A., Kääb, A., Huggel, C., Paul, F., Cogley, J., Frey, H., Kargel, J., Fujita, K., Scheel, M. et al. (2012), 'The state and fate of Himalayan glaciers', *Science* **336**(6079), 310–314.

Bookhagen, B. (2012), 'High resolution spatiotemporal distribution of rainfall seasonality and extreme events based on a 12-year TRMM time series'.

Bookhagen, B. & Burbank, D. (2006), 'Topography, relief, and TRMM-derived rainfall variations along the Himalaya', *Geophysical Research Letters* **33**(8).

Bookhagen, B. & Burbank, D. W. (2010), 'Toward a complete Himalayan hydrological budget: Spatiotemporal distribution of snowmelt and rainfall and their impact on river discharge', *Journal of Geophysical Research: Earth Surface (2003–2012)* **115**(F3).

Brubaker, K., Rango, A. & Kustas, W. (1996), 'Incorporating radiation inputs into the snowmelt runoff model', *Hydrological processes* **10**(10), 1329–1343.

Casey, K. A. (2011), 'Supraglacial dust and debris characterization via in situ and optical remote sensing methods'.

Casey, K., Kääb, A. & Benn, D. (2012), 'Geochemical characterization of supraglacial debris via in situ and optical remote sensing methods: a case study in Khumbu Himalaya, Nepal', *The Cryosphere* **6**(1), 85–100.

Cenderelli, D. A. & Wohl, E. E. (2001), 'Peak discharge estimates of glacial-lake outburst floods and "normal" climatic floods in the Mount Everest region, Nepal', *Geomorphology* **40**(1), 57–90.

Chen, J. M., Chen, X., Ju, W. & Geng, X. (2005), 'Distributed hydrological model for mapping evapotranspiration using remote sensing inputs', *Journal of Hydrology* **305**(1), 15–39.

Coll, C., Galve, J. M., Sanchez, J. M. & Caselles, V. (2010), 'Validation of Landsat-7/ETM+ thermal-band calibration and atmospheric correction with ground-based measurements', *Geoscience and Remote Sensing, IEEE Transactions on* **48**(1), 547–555.

Cuffey, K. M. & Paterson, W. S. B. (2010), *The physics of glaciers*, Academic Press.

Dinku, T., Hailemariam, K., Maidment, R., Tarnavsky, E. & Connor, S. (2014), 'Combined use of satellite estimates and rain gauge observations to generate high-quality historical rainfall time series over Ethiopia', *International Journal of Climatology* **34**(7), 2489–2504.

Fujii, Y. & Higuchi, K. (1977), 'Statistical Analyses of the Forms of the Glaciers in the Khumbu Himal: Glaciological Expedition of Nepal, Contribution No. 31', *Journal of the Japanese Association of Snow and Ice* **39**, 7–14.

Fukui, K., Fujii, Y., Ageta, Y. & Asahi, K. (2007), 'Changes in the lower limit of mountain permafrost between 1973 and 2004 in the Khumbu Himal, the Nepal Himalayas', *Global and Planetary Change* **55**(4), 251–256.

Gades, A., Conway, H., Nereson, N., Naito, N. & Kadota, T. (2000), 'Radio echo-sounding through supraglacial debris on Lirung and Khumbu Glaciers, Nepal Himalayas', *IAHS PUBLICATION* pp. 13–24.

Groppelli, B., Soncini, A., Bocchiola, D. & Rosso, R. (2011), 'Evaluation of future hydrological cycle under climate change scenarios in a mesoscale Alpine watershed of Italy', *Natural Hazards and Earth System Science* **11**(6), 1769–1785.

Hannah, D. M., Kansakar, S. R., Gerrard, A. & Rees, G. (2005), 'Flow regimes of Himalayan rivers of Nepal: nature and spatial patterns', *Journal of Hydrology* **308**(1), 18–32.

Higuchi, K., Ageta, Y., Yasunari, T. & Inoue, J. (1982), 'Characteristics of precipitation during the monsoon season in high-mountain areas of the Nepal Himalaya', *Hydrological Aspects of Alpine and High-Mountain Areas* **138**, 21–30.

Hock, R. (2003), 'Temperature index melt modelling in mountain areas', *Journal of Hydrology* **282**(1), 104–115.

Immerzeel, W., Droogers, P., De Jong, S. & Bierkens, M. (2009), 'Large-scale monitoring of snow cover and runoff simulation in Himalayan river basins using remote sensing', *Remote Sensing of Environment* **113**(1), 40–49.

Immerzeel, W., Pellicciotti, F. & Bierkens, M. (2013), 'Rising river flows throughout the twenty-first century in two himalayan glacierized watersheds', *Nature Geoscience* **6**(9), 742–745.

Immerzeel, W., Petersen, L., Ragettli, S. & Pellicciotti, F. (2014), 'The importance of observed gradients of air temperature and precipitation for modeling runoff from a glacierized watershed in the Nepalese Himalayas', *Water Resources Research* **50**(3), 2212–2226.

Immerzeel, W. W., Van Beek, L., Konz, M., Shrestha, A. & Bierkens, M. (2012), 'Hydrological response to climate change in a glacierized catchment in the Himalayas', *Climatic change* **110**(3-4), 721–736.

Jajarmizadeh, M.and Harun, S. & Salarpour, M. (2012), 'A Review on Theoretical Consideration and Types of Models in Hydrology', *Journal of Environmental Science and Technology* **5**(5), 249–261.

Kattel, D., Yao, T., Yang, K., Tian, L., Yang, G. & Joswiak, D. (2013), 'Temperature lapse rate in complex mountain terrain on the southern slope of the central Himalayas', *Theoretical and applied climatology* **113**(3-4), 671–682.

Kodama, H. & Mae, S. (1976), 'The Flow of Glaciers in the Khumbu Region: Glaciological Expedition to Nepal, Contribution No. 10', *Journal of the Japanese Association of Snow and Ice* **38**, 31–36.

Konz, M. ETH, Z. (2009), 'Manual on Snow and Glacier Melt Runoff Modelling in the Himalayas'.

Krause, P., Boyle, D. & Bäse, F. (2005), 'Comparison of different efficiency criteria for hydrological model assessment', *Advances in Geosciences* **5**(5), 89–97.

Martinec, J. (1989), 'Hour-to-hour snowmelt rates and lysimeter outflow during an entire ablation period', *Snow Cover and Glacier Variations* pp. 19–28.

Mattson, L. (1993), 'Ablation on debris covered glaciers: an example from the Rakhiot Glacier, Panjab, Himalaya', *IAHS publication* **218**, 289–296.

Mihalcea, C., Mayer, C., Diolaiuti, G., D'agata, C., Smiraglia, C., Lambrecht, A., Vuillermoz, E. & Tartari, G. (2008), 'Spatial distribution of debris thickness and melting from remote-sensing and meteorological data, at debris-covered Baltoro glacier, Karakoram, Pakistan', *Annals of glaciology* **48**(1), 49–57.

Mishra, B. K., Takara, K. & Tachikawa, Y. (2008), 'Regionalization of Nepalese river basins for flood frequency analysis', *J. Hydraul. Eng* **52**, 91–96.

Moribayashi, S. (1978), 'Transverse Profiles of Khumbu Glacier Obtained by Gravity Observation: Glaciological Expedition of Nepal, Contribution No. 46', *Journal of the Japanese Association of Snow and Ice* **40**, 21–25.

Nagler, T., Rott, H., Malcher, P. & Müller, F. (2008), 'Assimilation of meteorological and remote sensing data for snowmelt runoff forecasting', *Remote sensing of environment* **112**(4), 1408–1420.

Naito, N., Nakawo, M., Kadota, T. & Raymond, C. F. (2000), Numerical simulation of recent shrinkage of Khuinbu Glacier, Nepal Himalayas, *in* 'Debris-covered Glaciers: Proceedings of an International Workshop Held at the University of Washington in Seattle, Washington, USA, 13-15 September 2000', number 264, IAHS, p. 245.

Nakawo, M., Iwata, S., Watanabe, O. & Yoshida, M. (1986), 'Processes which distribute supraglacial debris on the Khumbu Glacier, Nepal Himalaya', *rn* **500**, 129–131.

Nakawo, M. & Rana, B. (1999), 'Estimate of ablation rate of glacier ice under a supraglacial debris layer', *Geografiska Annaler: Series A, Physical Geography* **81**(4), 695–701.

Nakawo, M., Yabuki, H. & Sakai, A. (1999), 'Characteristics of Khumbu Glacier, Nepal Himalaya: recent change in the debris-covered area', *Annals of Glaciology* **28**(1), 118–122.

Nepal, S. (2012), 'Evaluating upstream downstream linkages of Hydrological Dynamics in the Himalayan Region'.

Nepal, S., Krause, P., Flügel, W., Fink, M. & Fischer, C. (2014), 'Understanding the hydrological system dynamics of a glaciated alpine catchment in the Himalayan region using the J2000 hydrological model', *Hydrological Processes* **28**(3), 1329–1344.

Nicholson, L. & Benn, D. I. (2013), 'Properties of natural supraglacial debris in relation to modelling sub-debris ice ablation', *Earth Surface Processes and Landforms* **38**(5), 490–501.

Oerlemans, J. (2001), *Glaciers and climate change*, Balkema.

Paramithiotti, V. (2013), Climate change assessment and hydrological modelling in the Dudhkosi River basin, Eastern Nepal, Master's thesis, Politecnico di Milano.

Pellicciotti, F., Brock, B., Strasser, U., Burlando, P., Funk, M. & Corripio, J. (2005), 'An enhanced temperature-index glacier melt model including the shortwave radiation balance: development and testing for Haut Glacier d'Arolla, Switzerland', *Journal of Glaciology* **51**(175), 573–587.

Peters, J., Bolch, T., Buchroithner, M. & Baessler, M. (2010), 'Glacier Surface Velocities in the Mount Everest Area using ASTER and Ikonos imagery'.

Putkonen, J. K. (2004), 'Continuous snow and rain data at 500 to 4400 m altitude near Annapurna, Nepal, 1999-2001', *Arctic, Antarctic, and Alpine Research* **36**(2), 244–248.

Quincey, D., Luckman, A. & Benn, D. (2009), 'Quantification of Everest region glacier velocities between 1992 and 2002, using satellite radar interferometry and feature tracking', *Journal of Glaciology* **55**(192), 596–606.

Rounce, D. & McKinney, D. (2014), 'Debris thickness of glaciers in the Everest area (Nepal Himalaya) derived from satellite imagery using a nonlinear energy balance model', *The Cryosphere* **8**(4), 1317–1329.

Senese, A., Maugeri, M., Vuillermoz, E., Smiraglia, C. & Diolaiuti, G. (2014), 'Using daily air temperature thresholds to evaluate snow melting occurrence and amount on Alpine glaciers by T-index models: the case study of the Forni Glacier (Italy)', *The Cryosphere* **8**(5), 1921–1933.

Shrestha, A., Chapagain, P. & Thapa, R. (2011), 'Flash Flood Risk Management', *International Centre for Integrated Mountain Development (ICIMOD)* .

Takehuci, Y. (2000), 'Practical prediction of ice melting beneath various thickness of debris cover on Kliumbu Glacier, Nepal, using a positive degree-day factor', *Debris-covered Glaciers: Proceedings of an International Workshop Held at the University of Washington in Seattle, Washington, USA, 13-15 September 2000* (264), 71.

USDA United States Department of Agriculture, Natural Resources Conservation Service, C. E. D. (1986), Urban Hydrology for small Watersheds, Technical report, USDA Soil Conservation Service.

Velasco-Forero, C. A., Sempere-Torres, D., Cassiraga, E. F. & Jaime Gómez-Hernández, J. (2009), 'A non-parametric automatic blending methodology to estimate rainfall fields from rain gauge and radar data', *Advances in Water Resources* **32**(7), 986–1002.

Wagner, P. D., Fiener, P., Wilken, F., Kumar, S. & Schneider, K. (2012), 'Comparison and evaluation of spatial interpolation schemes for daily rainfall in data scarce regions', *Journal of Hydrology* **464**, 388–400.

Wan, Z., Zhang, Y., Zhang, Q. & Li, Z.-L. (2004), 'Quality assessment and validation of the MODIS global land surface temperature', *International Journal of Remote Sensing* **25**(1), 261–274.

Watanabe, O., Iwata, S. & Fushimi, H. (1986), 'Topographic characteristics in the ablation area of the Khumbu Glacier, Nepal Himalaya', *Annals of Glaciology* **8**, 177–180.

Weertman, J. (1957), 'On the sliding of glaciers', *J. Glaciol* **3**(21), 33–38.

Weiß, M. & Menzel, L. (2008), 'A global comparison of four potential evapotranspiration equations and their relevance to stream flow modelling in semi-arid environments', *Advances in Geosciences* **18**(18), 15–23.

Wigmosta, M. S., Vail, L. W. & Lettenmaier, D. P. (1994), 'A distributed hydrology-vegetation model for complex terrain', *Water resources research* **30**(6), 1665–1679.

Zhang, Y., Fujita, K., Liu, S., Liu, Q. & Nuimura, T. (2011), 'Distribution of debris thickness and its effect on ice melt at Hailuogou glacier, southeastern Tibetan Plateau, using in situ surveys and ASTER imagery', *Journal of Glaciology* **57**(206), 1147–1157.